VOLUME 32 DECEMBER 1954 NUMBER 12

Canadian Journal of Physics

Editor: G. M. VOLKOFF

Associate Editors:

L. G. ELLIOTT, *Atomic Energy of Canada, Ltd., Chalk River*
J. S. FOSTER, *McGill University*
G. HERZBERG, *National Research Council of Canada*
L. LEPRINCE-RINGUET, *Ecole Polytechnique, Paris*
D. W. R. McKINLEY, *National Research Council of Canada*
B. W. SARGENT, *Queen's University*
Sir FRANCIS SIMON, *Clarendon Laboratory, University of Oxford*
W. H. WATSON, *University of Toronto*

Published by THE NATIONAL RESEARCH COUNCIL
OTTAWA CANADA

CANADIAN JOURNAL OF PHYSICS

(*Formerly Section A, Canadian Journal of Research*)

Under the authority of the Chairman of the Committee of the Privy Council on Scientific and Industrial Research, the National Research Council issues annually THE CANADIAN JOURNAL OF PHYSICS and six other journals devoted to the publication of the results of original scientific research. Matters of general policy concerning these journals are the responsibility of a joint Editorial Board consisting of: members representing the National Research Council of Canada; the Editors of the Journals; and members representing the Royal Society of Canada and four other scientific societies.

EDITORIAL BOARD

Representatives of the National Research Council

A. N. Campbell, *University of Manitoba*
G. E. Hall, *University of Western Ontario*
E. G. D. Murray, *McGill University*
D. L. Thomson, *McGill University*
W. H. Watson (Chairman), *University of Toronto*

Editors of the Journals

D. L. Bailey, *University of Toronto*
J. B. Collip, *University of Western Ontario*
E. H. Craigie, *University of Toronto*
G. A. Ledingham, *National Research Council*
Léo Marion, *National Research Council*
R. G. E. Murray, *University of Western Ontario*
G. M. Volkoff, *University of British Columbia*

Representatives of Societies

D. L. Bailey, *University of Toronto*
Royal Society of Canada
J. B. Collip, *University of Western Ontario*
Canadian Physiological Society
E. H. Craigie, *University of Toronto*
Royal Society of Canada
R. G. E. Murray, *University of Western Ontario*
Canadian Society of Microbiologists
H. G. Thode, *McMaster University*
Chemical Institute of Canada
T. Thorvaldson, *University of Saskatchewan*
Royal Society of Canada
G. M. Volkoff, *University of British Columbia*
Royal Society of Canada; Canadian Association of Physicists

Ex officio

Léo Marion (Editor-in-Chief), *National Research Council*

Manuscripts for publication should be submitted to Dr. Léo Marion, Editor-in-Chief, Canadian Journal of Physics, National Research Council, Ottawa 2, Canada.
(For instructions on preparation of copy, see **Notes to Contributors** (inside back cover).)

Proof, correspondence concerning proof, and *orders for reprints* should be sent to the Manager, Editorial Office (Research Journals), Division of Administration, National Research Council, Ottawa 2, Canada.

Subscriptions, renewals, and orders for single or back numbers should be sent to Division of Administration, National Research Council, Ottawa 2, Canada. Remittances should be made payable to the Receiver General of Canada, credit National Research Council.

The journals published, frequency of publication, and prices are:

Canadian Journal of Biochemistry and Physiology	Bimonthly	$3.00 a year
Canadian Journal of Botany	Bimonthly	$4.00 a year
Canadian Journal of Chemistry	Monthly	$5.00 a year
Canadian Journal of Microbiology*	Bimonthly	$3.00 a year
Canadian Journal of Physics	Monthly	$4.00 a year
Canadian Journal of Technology	Bimonthly	$3.00 a year
Canadian Journal of Zoology	Bimonthly	$3.00 a year

The price of single numbers of all journals is 75 cents.

*Volume 1 will combine three numbers published in 1954 with six published in 1955 and will be available at the regular annual subscription rate of $3.00.

NOTICE

The title page included with this issue should be used in bound copies of the Canadian Journal of Physics in place of the page that appears in the January 1954 issue.

Canadian Journal of Physics

Issued by THE NATIONAL RESEARCH COUNCIL OF CANADA

VOLUME 32 DECEMBER 1954 NUMBER 12

THE PROPAGATION OF AN ELECTROMAGNETIC WAVE ALONG AN INFINITE CORRUGATED SURFACE[1]

BY R. A. HURD

ABSTRACT

Propagation of an electromagnetic wave along an infinite corrugated surface whose slot walls are vanishingly thin is investigated using a method based on the calculus of residues. The method yields expressions for the amplitudes and phase velocities which are highly accurate near cutoff when the number of slots per wavelength is greater than about five.

1. INTRODUCTION

In recent years, the application of corrugated surfaces to linear accelerators and antennas has aroused interest in the theoretical problem of finding the phase velocity and "mode" amplitudes of the surface wave which propagates on an infinitely wide surface. No rigorous solution to this problem is known, but approximate solutions have been obtained (1, 2, 4, 5). Of these papers, only that of Brillouin (1) has given expressions for the amplitudes, the others being concerned with the phase velocity only.

The problem, as considered by Brillouin, was simplified by making the following assumptions:

(*a*) The slot walls are vanishingly thin.

(*b*) Only the propagating (TEM) mode in the slots is reflected from the base of the slots. As far as the higher order attenuated waves are concerned, the slots are of infinite depth.*

To this idealized problem, Brillouin has given an approximate solution.

In the work which follows, we shall be able to give an exact solution to this simplified problem, thus obtaining a useful solution to the problem of the corrugated surface with vanishingly thin slot walls, valid for frequencies *near cutoff*, when the number of slots per wavelength is about five or greater.

2. PRELIMINARY THEORY

Consider the configuration shown in Fig. 1. A perfectly conducting plate coincides with the plane $y = -h$. On the plate is built up a series of parallel, infinitely thin walls of height h, spaced a distance d apart. The walls are

[1]*Manuscript received July 9, 1954.*

Contribution from the Radio and Electrical Engineering Division, National Research Council, Ottawa, Canada. Issued as N.R.C. No. 3436.

**Assumption* (*b*) *is equivalent to assuming that the slot width is small compared with both the slot depth and the free space wavelength.*

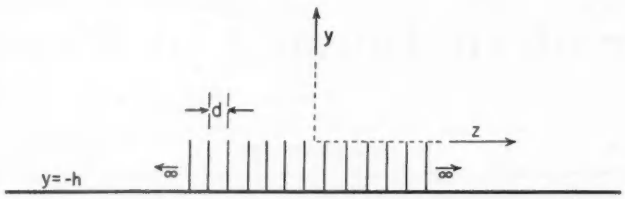

FIG. 1. An infinite corrugated surface.

assumed to extend to infinity in the $\pm x$ directions, and to be infinite in number in the $\pm z$ directions.

In the region above the slots it is assumed that there exists a wave proceeding in the $+z$ direction. This wave will be assumed to have three field components only, E_y, E_z, H_x. The problem is thus a scalar one, with

$$E_y = -(i/\omega\epsilon)\partial H_x/\partial z, \tag{1a}$$

$$E_z = (i/\omega\epsilon)\partial H_x/\partial y, \tag{1b}$$

$$\partial^2 H_x/\partial y^2 + \partial^2 H_x/\partial z^2 + k^2 H_x = 0. \tag{2}$$

Here $k = 2\pi/\lambda$ is the free space propagation constant. The time dependence of $e^{i\omega t}$ has been omitted.*

On account of the periodic nature of the structure, the field above the slots will not be a simple wave but will be a summation of an infinite number of waves of differing amplitudes and phase constants:

$$H_x = \sum_{n=-\infty}^{\infty} A_n e^{-\alpha_n y - i\beta_n z}, \tag{3}$$

$$\alpha_n = (\beta_n^2 - k^2)^{\frac{1}{2}}. \tag{4}$$

The phase constants, β_n, may be shown (1) to satisfy a relation of the form

$$\beta_n = \beta_0 + 2\pi n/d \quad (n = 0, \pm 1, \pm 2, \ldots). \tag{5}$$

Since we are looking for surface waves, we shall assume that $\beta_0 > k$ and that the positive root is always taken in Equation [4].

In the νth slot region the field is represented by a superposition of all the x-independent modes which satisfy the boundary conditions at the base and sides of the slot:

$$H_x^{(\nu)} = \sum_{m=0}^{\infty} B_m^{(\nu)} \cos \gamma_m (y+h) \cos(m\pi z_\nu/d), \tag{6}$$

$$\gamma_m = [k^2 - (m\pi/d)^2]^{\frac{1}{2}}. \tag{7}$$

Here z_ν is measured from the left-hand wall of the νth slot, and is related to z through

$$z_\nu = z - (\nu - \tfrac{1}{2})d.$$

*The m.k.s. unit system is employed.

The coefficients, $B_m^{(\nu)}$, have to be chosen to give the correct phase change from slot to slot, hence

$$B_m^{(\nu)} = B_m e^{-i\nu\beta_0 d}.$$

The unknowns of the problem are the coefficient ratios A_n/B_0, B_m/B_0, and the phase constant β_0. These are determined by ensuring continuity of the tangential magnetic and electric fields (H_x and $\partial H_x/\partial y$) across the mouth of the νth slot. Therefore

$$[8a] \qquad \sum_{m=0}^{\infty} B_m \cos(m\pi z_\nu/d) \cos\gamma_m h = \sum_{n=-\infty}^{\infty} A_n e^{-i\beta_n(z_\nu - d/2)},$$

$$[8b] \qquad \sum_{m=0}^{\infty} \gamma_m B_m \cos(m\pi z_\nu/d) \sin\gamma_m h = \sum_{n=-\infty}^{\infty} \alpha_n A_n e^{-i\beta_n(z_\nu - d/2)},$$

for $0 \leqslant z_\nu \leqslant d$. Solving Equations [8] for the coefficients B_m yields the equations, true for all m,

$$[9a] \qquad \frac{d}{2}\,\frac{\epsilon_m B_m \cos\gamma_m h}{(-)^m e^{-i\beta_0 d} - 1} = \sum_{-\infty}^{\infty} \frac{i\beta_n A_n e^{i\beta_n d/2}}{\alpha_n^2 + \gamma_m^2},$$

$$[9b] \qquad \frac{d}{2}\,\frac{\epsilon_m \gamma_m B_m \sin\gamma_m h}{(-)^m e^{-i\beta_0 d} - 1} = \sum_{-\infty}^{\infty} \frac{i\alpha_n \beta_n A_n e^{i\beta_n d/2}}{\alpha_n^2 + \gamma_m^2},$$

where

$$\epsilon_m = \begin{cases} 2, & m = 0 \\ 1, & m > 0 \end{cases}.$$

Multiplication of Equation [9a] by $i\gamma_m$ and addition and subtraction of [9a] and [9b] gives

$$[10] \qquad \frac{d}{2}\,\frac{\epsilon_m \gamma_m B_m e^{-i\gamma_m h}}{(-)^m e^{-i\beta_0 d} - 1} = \sum_{-\infty}^{\infty} \frac{\beta_n A_n e^{i\beta_n d/2}}{\alpha_n - i\gamma_m} \quad (m = 0, 1, 2, \ldots),$$

$$[11] \qquad -\frac{d}{2}\,\frac{\epsilon_m \gamma_m B_m e^{i\gamma_m h}}{(-)^m e^{-i\beta_0 d} - 1} = \sum_{-\infty}^{\infty} \frac{\beta_n A_n e^{i\beta_n d/2}}{\alpha_n + i\gamma_m} \quad (m = 0, 1, 2, \ldots).$$

If now assumption (b) of the preceding section is invoked, it is seen that the factors $e^{-i\gamma_m h}$ ($m > 0$) are small. We may therefore agree to neglect the left-hand side of Equation [10] when $m > 0$. Thus

$$[12a] \qquad \frac{kdB_0 e^{-ikh}}{e^{-i\beta_0 d} - 1} = \sum_{-\infty}^{\infty} \frac{\beta_n A_n e^{i\beta_n d/2}}{\alpha_n - ik},$$

$$[12b] \qquad 0 = \sum_{-\infty}^{\infty} \frac{\beta_n A_n e^{i\beta_n d/2}}{\alpha_n - i\gamma_m} \quad (m = 1, 2, \ldots).$$

Equations [12] are to be solved for the unknowns A_n. Equations [11] will be used later to determine the coefficients B_m.

3. SOLUTION OF THE EQUATIONS

Equations [12] have the same form as a set of equations solved by Whitehead (8), and the analysis used here follows his method. Consider a meromorphic function $f(w)$ which

(i) has simple poles at $w = \alpha_n$ ($n = 0, \pm 1, \pm 2, \ldots$);

(ii) has simple zeros at $w = i\gamma_m$ $(m = 1, 2, 3, \ldots)$;

(iii) tends to zero as $|w| \to \infty$, except near the poles α_n.

Choose a circle C_s which encloses the point $w = ik$ and the poles at $w = \alpha_n$, $|n| \leqslant s$. Then by Cauchy's theorem of residues

$$[13] \qquad \lim_{s\to\infty} \frac{1}{2\pi i} \int_{C_s} \frac{f(w)}{w - i\gamma_m}\, dw = \sum_{-\infty}^{\infty} \frac{r(\alpha_n)}{\alpha_n - i\gamma_m} + \delta_{0m} f(ik) = 0,$$

where $r(\alpha_n)$ is the residue of $f(w)$ at $w = \alpha_n$, and

$$\delta_{0m} = \begin{cases} 1 \text{ for } m = 0 \\ 0 \text{ for } m > 0 \end{cases}.$$

Setting

$$[14] \qquad f(ik) = -\frac{kdB_0 e^{-ikh}}{e^{-i\beta_0 d} - 1},$$

the solution to Equations [12] is given by

$$[15] \qquad A_n = r(\alpha_n)\beta_n^{-1} e^{-i\beta_n d/2}.$$

A function of $f(w)$ that satisfies all the conditions of the problem (i.e., conditions (i), (ii), (iii), and Equation [14]) is

$$[16] \qquad f(w) = -\frac{kdB_0 e^{-ikh}}{e^{-i\beta_0 d} - 1} \frac{ik - \alpha_0}{w - \alpha_0} \frac{\Pi_1(w)\Pi_2(ik)}{\Pi_1(ik)\Pi_2(w)} \exp\left[(d/\pi)(ik - w)\log 2\right],$$

where $\Pi_1(w)$ and $\Pi_2(w)$ are defined by

$$\Pi_1(w) = \prod_{p=1}^{\infty} (w - i\gamma_p)(-d/p\pi) e^{dw/p\pi},$$

$$\Pi_2(w) = \prod_{p=1}^{\infty} (w - \alpha_p)(w - \alpha_{-p})(d/2p\pi)^2 e^{dw/p\pi}.$$

In Equation [16] the exponential factor is necessary to ensure the proper behavior of $f(w)$ as $|w| \to \infty$. For details of the choice of this function, the reader is referred to Whitehead's paper (8).

4. CALCULATION OF THE MODE AMPLITUDES

To compute the coefficients A_m, we should ordinarily make use of relations [15] and [16]. However, computation of the residues of $f(w)$ as given by Equation [16] is awkward for the higher values of n; so it will be found convenient to derive an alternative expression. To do this, note that

$$[17] \qquad \Pi_1(w)\Pi_1(-w) = \frac{\sin[d(w^2 + k^2)^{\frac{1}{2}}]}{d(w^2 + k^2)^{\frac{1}{2}}}$$

and

$$[18] \qquad \Pi_2(w)\Pi_2(-w) = \frac{\sin[(d/2)\{\beta_0 - (w^2 + k^2)^{\frac{1}{2}}\}]\sin[(d/2)\{\beta_0 + (w^2 + k^2)^{\frac{1}{2}}\}]}{(d/2)^2(\alpha_0^2 - w^2)}.$$

Hence

$$[19] \qquad f(w) = \frac{1}{4} \frac{kd^2 B_0 e^{-ikh}}{e^{-i\beta_0 d} - 1} \frac{(ik - \alpha_0)(w + \alpha_0)}{(w^2 + k^2)^{\frac{1}{2}}} \frac{\Pi_2(ik)}{\Pi_1(ik)} \frac{\Pi_2(-w)}{\Pi_1(-w)}$$

$$\times \frac{\sin[d(w^2 + k^2)^{\frac{1}{2}}]}{\sin[(d/2)\{\beta_0 + (w^2 + k^2)^{\frac{1}{2}}\}]\sin[(d/2)\{\beta_0 - (w^2 + k^2)^{\frac{1}{2}}\}]} \exp\left[\frac{d}{\pi}(ik - w)\log 2\right].$$

Using Equations [15] and [19], we obtain, after some computation,

$$[20] \qquad \left|\frac{A_n}{B_0}\right| = \frac{1}{2}\,\frac{k(\alpha_n+\alpha_0)}{\alpha_n|\beta_n|}\,\frac{\Pi_2(-\alpha_n)}{\Pi_1(-\alpha_n)}\exp\left(-\frac{\alpha_n d\log 2}{\pi}\right),$$

where use has been made of the relations

$$|\Pi_1(ik)| = 1,$$

$$|\Pi_2(ik)| = \frac{\sin(\beta_0 d/2)}{\beta_0 d/2},$$

which are easily derivable from Equations [17] and [18].

There does not seem to be any easy way of computing the coefficients $\Pi_1(-\alpha_n)$ and $\Pi_2(-\alpha_n)$ exactly. However, a good approximation is obtained by extracting the initial term from the infinite product and using the approximations

$$\alpha_p \simeq |\beta_p|, \qquad i\gamma_p \simeq p\pi/d,$$

in the remaining terms of the infinite products. The products can then be expressed in terms of gamma functions. Thus

$$[21] \qquad \left|\frac{A_n}{B_0}\right| \simeq \frac{kd}{8\pi}\,\frac{(\alpha_n+\alpha_0)}{\alpha_n|\beta_n|}\,\frac{(\alpha_n+\alpha_1)(\alpha_n+\alpha_{-1})}{\alpha_n+i\gamma_1}$$

$$\times\,\frac{\Gamma(2+\alpha_n d/\pi)}{\Gamma[2+(d/2\pi)(\alpha_n+\beta_0)]\Gamma[2+(d/2\pi)(\alpha_n-\beta_0)]}\exp\left[-\frac{\alpha_n d\log 2}{\pi}\right].$$

The coefficients $|A_0/B_0|$, $|A_1/A_0|$, and $|A_{-1}/A_0|$ are shown plotted against h/λ, for $\lambda/d = 20$, in Fig. 2.

For large n,

$$[22] \qquad |A_n/B_0| \simeq (kd/4)(\pi|n|)^{-3/2}.$$

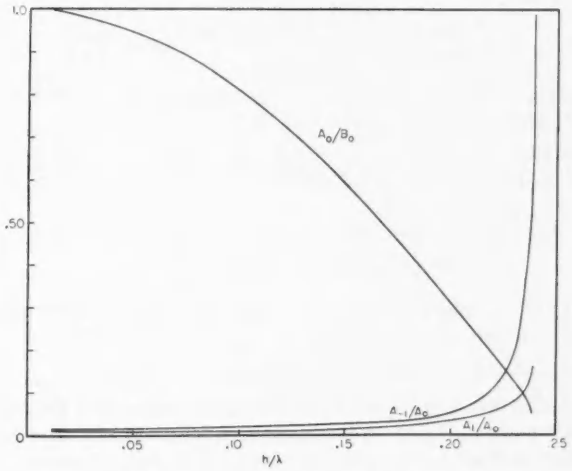

FIG. 2. Variation of A_0/B_0, A_{-1}/A_0, A_1/A_0 with h/λ.

To compute the coefficients B_m, consider the expression

$$[23] \qquad \lim_{z\to\infty} \frac{1}{2\pi i}\int_{C_z} \frac{f(w)}{w+i\gamma_m}\,dw = \sum_{n=-\infty}^{\infty} \frac{r(\alpha_n)}{\alpha_n+i\gamma_m} + f(-i\gamma_m) = 0,$$

($m = 0, 1, 2, \ldots$). Comparing Equations [11] and [23], it is found that

$$[24] \qquad f(-i\gamma_m) = \frac{d}{2}\,\frac{\epsilon_m\gamma_m B_m e^{t\gamma_m h}}{(-)^m e^{-i\beta_0 d}-1}.$$

Equations [16] and [24] then completely determine the B_m. For even m,

$$[25a] \qquad \left|\frac{B_m}{B_0}\right| = \frac{4k\sin(\beta_0 d/2)}{d\epsilon_m|\gamma_m||i\gamma_m+\alpha_0|}\,\frac{|\Pi_1(-i\gamma_m)|}{|\Pi_2(-i\gamma_m)|}\left|\exp\left[i\gamma_m\left(\frac{d}{\pi}\log 2-h\right)\right]\right|,$$

and for odd m,

$$[25b] \qquad \left|\frac{B_m}{B_0}\right| = \frac{4k|\cos(\beta_0 d/2)|}{d\epsilon_m|\gamma_m||i\gamma_m+\alpha_0|}\,\frac{|\Pi_1(-i\gamma_m)|}{|\Pi_2(-i\gamma_m)|}\left|\exp\left[i\gamma_m\left(\frac{d}{\pi}\log 2-h\right)\right]\right|.$$

When m is large,

$$[26a] \qquad |B_m/B_0| \simeq kd(\pi m/2)^{-3/2}\sin(\beta_0 d/2)\,e^{-t\gamma_m h}, \quad \text{for even } m;$$

$$[26b] \qquad |B_m/B_0| \simeq kd(\pi m/2)^{-3/2}|\cos(\beta_0 d/2)|e^{-t\gamma_m h}, \quad \text{for odd } m.$$

5. EVALUATION OF THE PHASE CONSTANT

The phase constant, β_0, may be determined by the elimination of B_0 between Equations [14] and [24]. This leads to the relation

$$[27] \qquad \frac{ik-\alpha_0}{ik+\alpha_0}\,\frac{\Pi_1(-ik)\Pi_2(ik)}{\Pi_1(ik)\Pi_2(-ik)}\exp\left[\frac{2ikd}{\pi}\log 2\right] = e^{2ikh}.$$

This equation is satisfied identically in modulus for real β_0. Upon taking arguments of each side,

$$[28] \qquad kh = -\sum_{m=1}^{\infty}\frac{kd}{m\pi} - \sin^{-1}\left(\frac{kd}{m\pi}\right) + \sum_{m=1}^{\infty}\frac{kd}{2m\pi} - \sin^{-1}\left(\frac{k}{\beta_m}\right)$$
$$+\sum_{m=1}^{\infty}\frac{kd}{2m\pi} - \sin^{-1}\left(\frac{k}{|\beta_{-m}|}\right) + \frac{kd\log 2}{\pi} + \cos^{-1}\left(\frac{k}{\beta_0}\right).$$

Approximating the inverse sines by their arguments, and leaving out terms of order $(d/\lambda)^3$ and higher, we obtain

$$[29] \qquad kh = \frac{kd}{2\pi}\left\{2\psi\left(1+\frac{\beta_0 d}{2\pi}\right) + \pi\cot\left(\frac{\beta_0 d}{2}\right) + 2C - \frac{2\pi}{\beta_0 d}\right\} + \cos^{-1}\left(\frac{k}{\beta_0}\right) + \frac{kd\log 2}{\pi},$$

where $\psi(x)$ is the digamma function (3),

$$\psi(x) = \frac{\Gamma'(x)}{\Gamma(x)} = -C-(1/x)+\sum_{n=1}^{\infty}\left(\frac{1}{n}-\frac{1}{x+n}\right),$$

and $C = 0.577$ is Euler's constant. In deriving Equation [29] use has been made of the relation

$$[30] \qquad \psi(x)+\psi(-x) = 2\psi(1+x)+\pi\cot\pi x-(1/x).$$

Equation [29] can now be solved graphically for β_0. This has been done in Fig. 3 which plots λ_g/λ ($\lambda_g = 2\pi/\beta_0$) as a function of slot depth for various values of slot width.

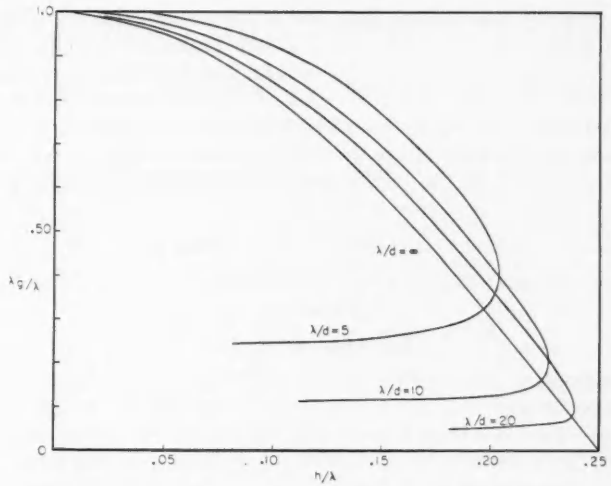

FIG. 3. λ_g/λ as a function of h/λ for various values of λ/d.

6. DISCUSSION

The results of the preceding sections call for some comment. With reference to Equation [29] it is apparent that for any h which corresponds to a solution λ_g/λ as given in Fig. 3 (say h_0), there is an infinite set of values $h_0+p\lambda/2$ ($p = 0, 1, 2, 3, \ldots$) which corresponds to the same value of λ_g/λ. The maximum value of h attained on any particular curve (Fig. 3) is the *cutoff* depth h_c. For values of h greater than h_c and less than $\lambda/2$, it can be shown that it is necessary to take the α_n ***negative***, and hence there is no surface wave in this case. Summarizing, we have propagation when h is such that

$$[31] \qquad (p\lambda/2) < h < (p\lambda/2)+h_c \quad (p = 0, 1, 2, \ldots),$$

and no propagation for h lying outside these limits.

By differentiation of the right-hand side of Equation [28] it can be shown that the cutoff value of d/λ_g is 0.5. Then, from Equation [5], $\beta_m = -\beta_{-m-1}$; and from Equation [20], $A_m = A_{-m-1}$. Thus a standing wave is set up on the surface. That this happens at cutoff has been pointed out by Walkinshaw (7).

By substituting $d/\lambda_g = 0.5$ in Equation [29] and using the relation

$$\psi(3/2) = 2-C-2\log 2,$$

one obtains

$$[32] \qquad h_c = (\lambda/4)-(d/\pi)\log 2 + (\text{terms of order } d^3/\lambda^2).$$

It is seen that, at cutoff, the slots may be considered to be parallel resonant with a discontinuity capacity at the mouth of the slots. The amount of shortening of h_c over $\lambda/4$ given by Equation [32] is in agreement with that which would be expected from electrostatic considerations. (See Smythe (6).)

It is to be noted that the left-hand side of Equation [27] is invariant under the substitution of $1/d-1/\lambda_g$ for $1/\lambda_g$. Hence Equation [27] has two roots λ_g' and λ_g'' connected by $1/\lambda_g'+1/\lambda_g'' = 1/d$. This is evident from the graphs in Fig. 3. Using Equation [5], $\beta_m' = -\beta_{-m-1}''$; and it is apparent that the two solutions correspond to equal waves which proceed in *opposite* directions.

When one compares the above results with those of Brillouin (1), it is seen that the expressions for the coefficients B_m are considerably different. Thus we find

$$|B_m| = O\{m^{-3/2}e^{-t\gamma_m h}\}, \quad \text{for large } m; \tag{33}$$

whereas, according to Brillouin (in our notation),

$$|B_m| = O\left\{\frac{e^{-t\gamma_m h}}{m^2[\frac{1}{2}(m-1)]!}\right\}, \quad \text{for large } m. \tag{34}$$

It is not difficult to see that Equation [34] must be incorrect, since coefficients defined in this way lead to expressions for E_y and E_z which are finite everywhere. This is a violation of the edge condition which states that $E_y, E_z = O\{R^{-\frac{1}{2}}\}$ for $R \to 0$, where R is the distance from the field point to any of the edges $y = 0, z = (\nu+\frac{1}{2})d$. On the other hand it is relatively easy to show that our coefficients A_n, B_m lead to expressions for E_y, E_z which exhibit the correct singularity at the edges.*

It is possible to obtain better approximations to the solution of the general problem by keeping terms of order greater than zero in the left-hand side of Equation [10]. In order to establish the range of d/λ and h/λ for which the above results are valid, the calculation was carried out retaining the B_1 term. For $\lambda/d = 5$ and $0.1\lambda \leqslant h \leqslant h_c$, it was found that the new phase velocity differed by less than 1% from the value found above, while the amplitudes varied by less than 3.5%. When $\lambda/d > 5$, there is, of course, a correspondingly larger range of h in which comparable accuracy is obtained.

7. ACKNOWLEDGMENTS

The writer is indebted to Dr. H. Gruenberg for helpful discussions of the problem; and to Miss N. McDougall who performed some of the computations.

REFERENCES

1. BRILLOUIN, L. J. Appl. Phys. 19: 1023. 1948.
2. CUTLER, C. C. Bell Telephone Lab. Rept. MM–44–160–218. 1944.
3. DAVIS, H. T. Tables of the higher mathematical functions. The Principia Press, Inc., Bloomington, Indiana. 1933.
4. ROTMAN, W. Proc. I.R.E. 39: 952. 1951.
5. Second Quart. Progr. Rept., Ridge and Corrugated Antenna Studies, Stanford Research Inst. Jan., 1951.
6. SMYTHE, W. R. Static and dynamic electricity. McGraw-Hill Book Company, Inc., New York. 1950. p. 104, problem 26.
7. WALKINSHAW, W. Proc. Phys. Soc. (London), B, 61: 246. 1948.
8. WHITEHEAD, E. A. N. Proc. Inst. Elec. Engrs. (London), 98, Pt. III (No. 51): 133. 1951.

**The error in Brillouin's work apparently lies in his Equation [51]. The generating function $f(\theta)$ given there is said to be unique, but actually it may be multiplied by any normalized integral function, and even more general functions having poles, and still satisfy the stated conditions (see Brillouin's Equations [46], [47], [48]). The choice of the correct multiplying function would appear to be dictated by the necessity that the fields satisfy the edge condition.*

THE ROTATIONAL RAMAN SPECTRUM OF ETHYLENE[1]

By J. Romanko,[2] T. Feldman, E. J. Stansbury,[3] and A. McKellar[4]

ABSTRACT

The rotational Raman spectrum of ethylene excited by Hg4358 was photographed with a reciprocal linear dispersion of 10.5 cm.$^{-1}$ per mm. In addition to S and R branches which, in the symmetric top approximation, can be used to determine $B_{[o]} + C_{[o]}$, the spectrum shows a series of lines which must be interpreted in terms of the asymmetric top model. This series is shown to be due to the transitions, $\Delta J = 2$, between the two lowest τ levels of each rotational state, and is used to determine $C_{[o]}$. The rotational constants obtained from the analysis are $A_{[o]} = 4.66 \pm 0.20$, $B_{[o]} = 1.008_8 \pm 0.006$, $C_{[o]} = 0.828_9 \pm 0.003$ cm^{-1}.

INTRODUCTION

The plane symmetric form (point group $\mathbf{V}_h$) for the ethylene molecule is generally accepted, and the structures of the vibrational infrared bands and the rotational Raman band show that the molecule is very nearly a symmetric top. If the principal moments of inertia are designated I_A, I_B, and I_C, with $I_A < I_B < I_C$,* then I_C refers to the principal axis of inertia perpendicular to the plane of the molecule, and I_A and I_B to the axes in the plane, which are parallel and perpendicular, respectively, to the carbon–carbon bond. Since I_B is nearly equal to I_C the symmetric top approximation has been used to determine the values of the rotational constants A, B, and C ($A = h/8\pi^2 cI_A$, etc.) from the spectrum. The value of $\tilde{B} = \frac{1}{2}(B + C)$ can be obtained from the P and R branches of parallel infrared bands and the value of $A - \tilde{B}$ from the Q branches of perpendicular bands. Using the relationship for planar molecules $1/C = 1/A + 1/B$, the constants A, B, and C and the moments of inertia can be calculated. The most accurate determination of these constants from the infrared spectrum appears to be that of Gallaway and Barker (3), who obtained $\tilde{B}_{[o]} = 0.9116$ and $A_{[o]} = 4.867$ cm.$^{-1}$ for the ground vibrational state.

The constants $A_{[o]}$, $B_{[o]}$, and $C_{[o]}$ can be also determined from rotational spectra. However, since the molecule has a center of symmetry, a pure rotational spectrum exists only in Raman effect. The Raman spectrum was photographed by Lewis and Houston (6) using a Hilger E1 quartz spectrograph and Hg2537 as the exciting radiation. With the available dispersion (~43 cm.$^{-1}$ per mm.) only a single series of lines with an average spacing of 3.68 cm.$^{-1}$ was observed. The series was interpreted as the S branch ($\Delta J = 2$) in the symmetric top approximation and the value $\tilde{B}_{[o]} = 0.920$ cm.$^{-1}$ was calculated from the average spacing. This value is in fair agreement with the infrared result.

[1]*Manuscript received August 30, 1954.*
Contribution from the McLennan Laboratory, University of Toronto, Toronto, Ontario, and to be reprinted as Contributions from the Dominion Astrophysical Observatory No. 40.
[2]*Holder of a Garnet W. McKee – Lachlan Gilchrist Scholarship, School of Graduate Studies, University of Toronto, 1952–54.*
[3]*Present address: Bell Telephone Laboratories, Murray Hill, New Jersey, U.S.A.*
[4]*Dominion Astrophysical Observatory, Victoria, B.C. Visiting Professor of Astronomy and Physics, University of Toronto, 1952–53.*
*The nomenclature used follows that of Herzberg (4).

The development of sources of high intensity (11, 9, 12) has made it possible to photograph Raman spectra with much higher dispersion than was formerly possible. In the present investigation the rotational spectrum of ethylene has been re-examined with the aim of improving the accuracy of the molecular constants and of ascertaining whether departures from the symmetric top spectrum might be observed in high dispersion spectrograms.

EXPERIMENTAL

The multiple reflection Raman tube and the high dispersion spectrograph have been described (12). The experiments with ethylene were carried out in an early stage of the development of the equipment when the irradiating source was one mercury lamp of the shape described in Reference (10), with internal cooling in the discharge section. Research grade ethylene gas was used at pressures from 1.5 to 3 atm. Exposure times from 2 to 24 hr. were used to record the spectrum on Kodak 103a-0 spectroscopic plates with a spectral slit width of 0.33 cm^{-1}. The reciprocal linear dispersion of the spectrograph was 10.5 $cm.^{-1}$ per mm. The microphotometer traces reproduced in Fig. 1 show the Stokes portion of the spectrum for exposure strengths of 36 and 22 atm. hr. with Hg4358 as the exciting line.

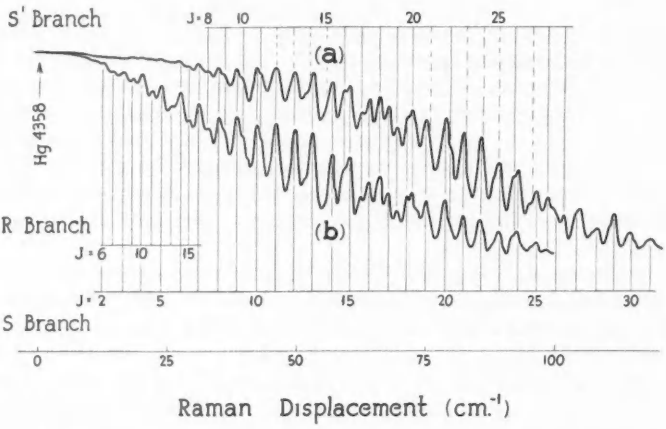

FIG. 1. Microphotometer traces of the Stokes portion of the rotational Raman spectrum of ethylene with exposure strengths of (*a*) 36 and (*b*) 22 atm. hr.

An iron arc comparison spectrum was photographed in juxtaposition with each Raman spectrum. Since there is a scarcity of iron lines in the region of Hg4358 a lightly exposed rotational Raman spectrum of oxygen was also used for comparison. The frequency shifts of the oxygen lines were calculated from the very accurate molecular constants given by Babcock and Herzberg (1). The wavelength of the exciting line was taken as 4358.35 Å as given in the M.I.T. Wavelength Tables. Three spectrograms with different strengths of

exposure, 36, 28, and 5 atm. hr., were measured on a Hilger comparator. The Stokes and anti-Stokes frequency shifts were averaged for each plate; finally, the frequency shifts for the three plates were averaged. The results are given in Table I.

TABLE I

ROTATIONAL RAMAN SHIFTS OF C_2H_4

$\Delta\nu$ (cm.$^{-1}$)	Intensity*	Assignment	$\Delta\nu$ (cm.$^{-1}$)	Intensity*	Assignment
7.27	5	$R(3)$	59.32	6	$S'(16)$
9.00	5	$S(1)$, $R(4)$	60.42	7	$S(15)$
10.60	3	—	62.73	2	$S'(17)$
11.67	3	—	64.39	4	$S(16)$
12.85	7	$S(2)$, $R(6)$	66.27	4	$S'(18)$
14.64	3*s*	$R(7)$	67.95	3	$S(17)$
16.49	8	$S(3)$, $R(8)$	69.88	1	$S'(19)$
18.27	4	$R(9)$	71.78	3	$S(18)$
20.15	9	$S(4)$, $R(10)$	72.79	3*d*	$S'(20)$
21.99	3	$R(11)$	73.79	1	—
23.80	8	$S(5)$, $R(12)$	75.56	3	$S(19)$
25.70	3*s*	$R(13)$	79.32	3	$S(20)$
27.54	8*d*	$S(6)$, $R(14)$	80.37	1*s*	$S'(22)$?
29.35	3*s*	$R(15)$	82.83	3*d*	$S(21)$
31.15	8	$S(7)$, $R(16)$	86.35	3*d*	$S(22)$
33.02	4	$S'(8)$	89.82	2*dd*	$S(23)$
34.99	7	$S(8)$	92.78	2	$S'(26)$
36.07	4	$S'(9)$	93.68	2	$S(24)$
38.51	7	$S(9)$	96.95	1*d*	$S(25)$
39.75	4	$S'(10)$	99.40	1*s*	$S'(28)$
42.43	7	$S(10)$	100.92	1*d*	$S(26)$
43.39	4	$S'(11)$	102.56	1*s*	$S'(29)$
46.10	7*d*	$S(11)$	105.18	1*dd*	$S(27)$
49.72	7	$S(12)$	109.02	1*d*	$S(28)$
51.78	1	$S'(13)$?	112.38	1*d*	$S(29)$
53.29	6	$S(13)$	115.97	0*d*	$S(30)$
56.80	6	$S(14)$	118.78	0*d*	$S(31)$

**The intensities given are visually estimated on a scale 10 to 0. Sharp lines are designated by s, diffuse lines by d, and the more diffuse lines by dd.*

DISCUSSION OF THE RESULTS

The S lines, corresponding to the transitions $\Delta J = 2$, $\Delta K = 0$, in the symmetric top approximation, are easily recognized in the spectrum. These were recorded by Lewis and Houston (6) up to $J = 20$ and, in the present investigation, to $J = 31$. The R lines ($\Delta J = 1$, $\Delta K = 0$) up to $J = 15$ are also easily observed on the high dispersion spectrograms. The relatively low intensity of the R branch is due to the low value, $\sim$0.25, of the ratio I_A/I_B (Placzek and Teller (8)). The assignments for the lines of the S and R branches are unambiguous and are listed in Table I.

In addition to the R and S lines other lines are observed in the part of the spectrum where the R branch is very weak. These extra lines form a series with a spacing somewhat smaller than that of the S lines and will be referred to as the S' lines. The S' series, observable only when it is out of step with the S series, imparts to the spectrum the characteristic appearance shown in Fig. 1.

When the Raman displacements of the S lines are plotted against J, as in Fig. 2, a straight line can be drawn through all the points. Also, when the correct relative numbering of the lines has been determined, the displacements of the S' lines plotted against J yield a straight line. The absolute numbering of the S' series in Fig. 2 is based on the analysis given below.

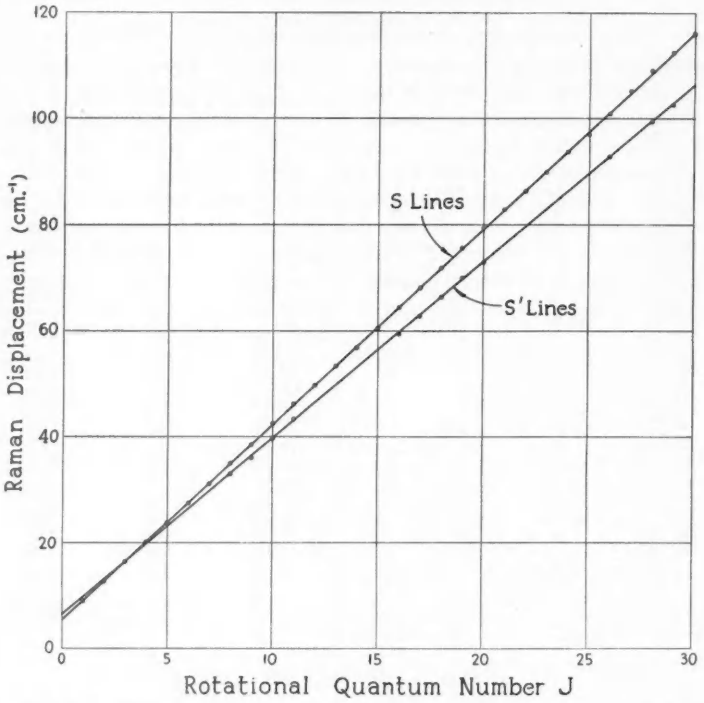

FIG. 2. The S and S' frequency shifts in the rotational Raman spectrum of ethylene as a function of the rotational quantum number J.

The R and S branches of the spectrum can be interpreted in terms of the symmetric top approximation. The S' branch, on the other hand, is an indication of the deviation of the molecule from an exactly symmetric top, and its interpretation must therefore be based on the theory of the asymmetric top.

In the symmetric top there are $J + 1$ sublevels of different energies for each value of the total rotational angular momentum quantum number, J; the assembly of energy levels is given by the expression

$$[1] \qquad F(J, K) = BJ(J + 1) + (A - B)K^2, \quad J = 0, 1, 2, \ldots,$$

where $K = 0, 1, 2, \ldots J$ and each level with $K \neq 0$ is doubly degenerate. In the asymmetric top this degeneracy is removed; for each value of J there are $2J + 1$ sublevels, $F(J_\tau)$, which are ordered by the subscript τ taking the values

$-J, -J+1, \ldots +J-1, +J$ with $\tau = -J$ assigned to the lowest level. When the asymmetric top is very nearly a symmetric top the τ levels can be correlated with the K levels of the equivalent symmetric top. Thus, for the prolate case, $I_B \sim I_C$, the highest pair of τ levels corresponds to $K = J$ and the lowest τ level to $K = 0$.

To determine the origin of the S' lines the frequencies for the $J = 12 \leftarrow J = 10$ Raman transition were calculated using the rotational constants as determined by Gallaway and Barker (3) and the eigenvalues of the asymmetric top as evaluated by King, Hainer, and Cross (5). The populations of the various initial levels were calculated using the statistical weights as given by Wilson (13). Since the matrix elements of the polarizability have not been evaluated for the asymmetric top, the matrix elements for the symmetric top (8) were used to determine the intensities. This procedure restricts the possible transitions to those for which $\Delta K = 0$ in the equivalent asymmetric top; however, since the ethylene molecule does not deviate much from the symmetric top model, the calculated spectrum should not be greatly in error.

In Fig. 3(*a*) the spectrum of the 12←10 transition is plotted for the case of very high spectral resolution. In Fig. 3(*b*) the spectrum is modified for a line width of 0.5 cm.$^{-1}$, which corresponds approximately to the resolution in the experiment. The highest intensity is that due to the nearly superposed lines resulting from transitions at high τ-values; since these energy levels deviate

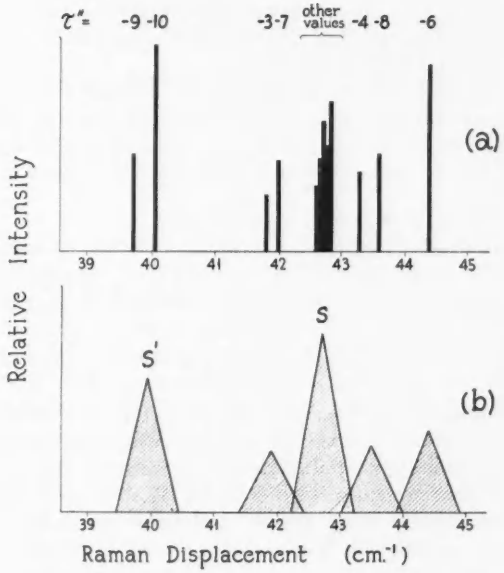

FIG. 3. (*a*) Calculated structure of the $J = 12 \leftarrow J = 10$ transition in the rotational Raman spectrum of ethylene.

(*b*) The calculated structure as modified by a line width of 0.5 cm^{-1}.

very little from those for the equivalent symmetric top this maximum corresponds to the S line. The next highest intensity is that given by the two transitions involving the two lowest sublevels in each J state ($J'_{\tau'}=12_{-12} \leftarrow J''_{\tau''}=10_{-10}$ and $J'_{\tau'}=12_{-11} \leftarrow J''_{\tau''}=10_{-9}$); for these levels the eigenvalues deviate farthest from those of the symmetric top. It is therefore evident that the S' lines can be correlated with the transitions, $\Delta J = 2$, between the two lowest sublevels of each J state. As has been shown by Dieke and Kistiakowsky (2), these two sublevels approach each other at high J values. The minor maxima in Fig. 3(*b*) are not observed, probably because of overlapping with lines from other transitions in J.

For the sublevels with the highest values of τ the formula for the equivalent symmetric top,

[2] $$F_{\text{prolate}}(J, K) = \tfrac{1}{2}(B + C)J(J + 1) + [A - \tfrac{1}{2}(B + C)]K^2,$$

is an adequate representation of the energy. Applying the selection rules, $\Delta J = 2$, $\Delta K = 0$, one obtains for the Raman shifts in the Stokes and anti-Stokes S branches the expression

[3] $$|\Delta\nu| = 2(B + C)J + 3(B + C), \quad J = 0, 1 \ldots .$$

The graph of $|\Delta\nu|$ against J is thus a straight line with slope $4\bar{B} = 2(B + C)$. As is evident in Fig. 2, the experimental data for the S lines can be represented by a straight line over the whole range of J. Since there is no noticeable curvature in the graph it is certain that centrifugal stretching terms, not taken into account in [2], can be neglected. A least squares analysis of the data gives the value $\bar{B}_{[0]} = 0.9187 \pm 0.0017$ cm^{-1}.

In the proposed interpretation of the S' lines an analytical representation of the S' frequency shifts requires an expression for the average value of the energies of the two lowest τ sublevels. For a molecule which approaches the limiting case of an *oblate* symmetric top Mecke (7) obtained the approximate formula

[4] $$\tfrac{1}{2}[F(J_{-J})+F(J_{-J+1})] = CJ^2+\tfrac{1}{2}(A+B)J - \tfrac{1}{8}(A-B)J\left(\frac{2J-1}{J-1}\right)b^*\left(1+\frac{b^{*2}}{4}\right),$$

where $$b^* = \frac{B-A}{2[C-\frac{1}{2}(A+B)]} \quad (=0.910 \text{ for } C_2H_4).$$

Numerical calculations were carried out to ascertain the degree of accuracy to which this formula can be used for ethylene, which approaches the limiting case of a *prolate* symmetric top. In Table II the values of $\frac{1}{2}[F(J_{-J}) + F(J_{-J+1})]$ are given for the even values of J up to $J = 12$. "Correct" values calculated from the eigenvalues of King, Hainer, and Cross are compared with values calculated from formula [4]; in both cases the rotational constants as determined in this investigation (Table IV) were used. The differences, δ, between the "correct" and the approximate values are given in the last column in the table. It is apparent that, although δ increases with J, the differences between

TABLE II

CALCULATED VALUES OF $\frac{1}{2}[F(J_{-J}) + F(J_{-J+1})]$

J	"Correct" value (cm.$^{-1}$)	Approximate value calculated from [4] (cm.$^{-1}$)	Difference, δ (cm.$^{-1}$)
4	19.783	19.914	0.131
6	39.245	40.219	0.974
8	65.672	67.117	1.445
10	98.780	100.633	1.853
12	138.584	140.775	2.191

successive δ's decrease with J; this indicates that formula [4] might be used to calculate the frequency shifts of the S' lines *at high J values.*

With the selection rule $\Delta J = 2$ the frequency shifts of the S' lines using formula [4] are

$$[5] \quad |\Delta\nu| = \tfrac{1}{2}\{F[(J+2)_{-J-2}]+F[(J+2)_{-J-1}]\}-\tfrac{1}{2}\{F(J_{-J})+F(J_{-J+1})\}$$

$$= 4C(J+1)+(A+B)-\frac{1}{8}(A-B)b^*\left(1+\frac{b^{*2}}{4}\right)\left(4-\frac{2}{J^2-1}\right), \; J = 0, 1, 2 \ldots .$$

In Table III "correct" frequency shifts for various transitions are compared with those calculated from the approximate formula [5]. The differences, Δ,

TABLE III

CALCULATED S' FREQUENCIES

Transition $J' \leftarrow J''$	"Correct" value (cm.$^{-1}$)	Approximate value calculated from [5] (cm.$^{-1}$)	Difference, Δ (cm.$^{-1}$)
6←4	19.462	20.305	0.843
8←6	26.427	26.898	0.471
10←8	33.108	33.516	0.408
12←10	39.804	40.142	0.338

decrease with increasing J, but the rate of decrease is less marked at high J values. However, for the 12←10 transition the discrepancy is already of the order of 0.3 cm^{-1}. It is therefore concluded that Mecke's approximation for the oblate asymmetric top can be safely applied to the case of ethylene.

Since the S' lines are observed only for $J > 7$ where they are no longer obscured by the R lines, a simplification in formula [5] can be made. With increasing J the term in $1/(J^2 - 1)$ decreases rapidly so that, at high J values, the S' frequency shifts plotted against J should give a straight line with the slope $4C$. A least squares analysis of the data, plotted in Fig. 2, gives the value $C_{[o]} = 0.8289 \pm 0.0027$ cm^{-1}. It may be noted that the straight line in the plot of $|\Delta\nu|$ vs. J at high J values has an intercept on the $|\Delta\nu|$ axis equal to

$$4C + (A + B) - \tfrac{1}{2}(A - B)b^*(1 + b^{*2}/4)$$

according to formula [5]. This fact was used to obtain the absolute numbering of the S' lines given in Table I and Fig. 1.

The rotational Raman spectrum of ethylene at high dispersion can thus be

used to evaluate all three rotational constants of the ground vibrational state. From the experimental values of $\bar{B}_{[o]} = 1/2(B_{[o]} + C_{[o]})$ and $C_{[o]}$, and the relation $1/A = 1/C - 1/B$, for a planar molecule, the values of $A_{[o]}$ and $B_{[o]}$ can be obtained. The results with their probable errors are summarized and compared with the infrared values of Gallaway and Barker (3) in Table IV.

TABLE IV

ROTATIONAL CONSTANTS FOR THE GROUND VIBRATIONAL STATE OF C_2H_4

	From the Raman spectrum ($cm.^{-1}$)	From the infrared spectrum (3) ($cm.^{-1}$)
$\bar{B}_{[o]}$	0.9187 ± 0.0017	0.9116
$A_{[o]}$	4.66 ± 0.20	4.867
$B_{[o]}$	$1.008_5 \pm 0.006$	0.996
$C_{[o]}$	$0.828_9 \pm 0.002_7$	0.827

The value of $C_{[o]}$ found in the present investigation agrees very well with the infrared value. The agreement of the values of $B_{[o]}$ is not as good, but the Raman value is probably the more accurate. The Raman value of $A_{[o]}$ has a large probable error because it is calculated from the difference of two quantities which are almost equal in the relation $1/A = 1/C - 1/B$. The infrared value of $A_{[o]}$, determined from the spacing of Q branches in perpendicular infrared bands, is undoubtedly more accurate.

With further advances in the techniques of high resolution Raman spectroscopy it is quite possible that more detail of the rotational Raman spectrum of ethylene can be resolved with a resultant improvement in the molecular constants. Also, the analysis of the rotational Raman spectra of slightly asymmetric top molecules, based on the observation of S and S' series, may well find applications in heavier molecules.

ACKNOWLEDGMENTS

The authors acknowledge with sincere thanks the constant advice and encouragement of Professor H. L. Welsh, and also their indebtedness to the Defence Research Board of Canada for generous financial support of the work in Raman spectroscopy of gases at the University of Toronto.

REFERENCES

1. BABCOCK, H. D. and HERZBERG, L. Astrophys. J. 108: 167. 1948.
2. DIEKE, G. H. and KISTIAKOWSKY, G. B. Phys. Rev. 45: 4. 1934.
3. GALLAWAY, W. S. and BARKER, E. F. J. Chem. Phys. 10: 88. 1942.
4. HERZBERG, G. Molecular spectra and molecular structure. Vol. II. Infrared and Raman spectra of polyatomic molecules. D. Van Nostrand Company, Inc., New York. 1945.
5. KING, G. W., HAINER, R. M., and CROSS, P. C. J. Chem. Phys. 11: 27. 1943; 17: 826. 1949.
6. LEWIS, C. M. and HOUSTON, W. V. Phys. Rev. 44: 903. 1933.
7. MECKE, R. Z. Physik, 81: 313. 1933.
8. PLACZEK, G. and TELLER, E. Z. Physik, 81: 209. 1933.
9. STOICHEFF, B. P. Can. J. Phys. 32: 330. 1954.
10. WELSH, H. L., CRAWFORD, M. F., THOMAS, T. R., and LOVE, G. R. Can. J. Phys. 30: 577. 1952.
11. WELSH, H. L., CUMMING, C., and STANSBURY, E. J. J. Opt. Soc. Amer. 41: 712. 1951.
12. WELSH, H. L., STANSBURY, E. J., ROMANKO, J., and FELDMAN, T. J. Opt. Soc. Amer. In press.
13. WILSON, E. B., JR. J. Chem. Phys. 3: 276. 1935.

STATISTICAL STUDIES OF POLAR RADIO BLACKOUTS[1]

By J. W. Cox and Kenneth Davies

ABSTRACT

A statistical study of high frequency radio blackouts in Canada is made from records taken at several ionosphere sounding stations. Both vertical incidence and communication data are examined to determine the geographical, seasonal, and diurnal distributions of the frequency of occurrence of blackout. It is found that blackouts are most abundant in the morning and that the time of maximum occurrence increases with increasing latitude.

I. INTRODUCTION

It is well known that high frequency radio communication is more difficult at high latitudes than at low latitudes because of the frequent occurrence of ionospheric disturbances. Studies by means of conventional vertical incidence pulse soundings have shown that, in general, the same ionospheric regions exist at both high and low latitudes but that at high latitudes rapid variations of considerable size in the ionospheric characteristics are more frequent and pronounced. This is particularly true of the F_2 and D regions which are the regions of greatest importance for high frequency radio propagation.

In the present paper a description will be given of some statistical studies of the frequency of occurrence of the so-called "no-echo" condition at a number of stations in Canada and in the U.S.A. over the period 1949 to 1952. Few attempts appear to have been made to study blackout phenomena and the present study has been made in an effort to make some use of the available data.

II. SOURCES OF DATA

The material used in this study consists of: the hourly records of observations at appropriately chosen ionospheric sounding stations at which records of vertical incidence pulse soundings are made, and the reception, at these ionospheric sounding stations, of signals from WWV, the standard high frequency sender of the National Bureau of Standards, Washington, U.S.A. These records were not made primarily for the purposes of this study, and certain limitations on accuracy, discussed later, had to be accepted.

The locations of the various stations are shown in Fig. 1 and in Table I.

TABLE I

Positions of ionosphere sounding stations

Station	ϕ North	λ West	Φ North	L.M.T.
Resolute Bay	74.7°	94.9°	82.9°	90°
Baker Lake	64.3°	96.0°	73.7°	90°
Churchill	58.8°	94.2°	68.8°	90°
Winnipeg	49.9°	97.4°	59.6°	90°
Washington	39.0°	77.5°	50°	75°

ϕ *Geographical latitude.*
λ *Geographical longitude.*
Φ *Geomagnetic latitude.*

[1]*Manuscript received July 12, 1954.*
Contribution from Defence Research Telecommunications Establishment, Defence Research Board, Ottawa. Research conducted under Defence Research Board Project D48-95-11-02.

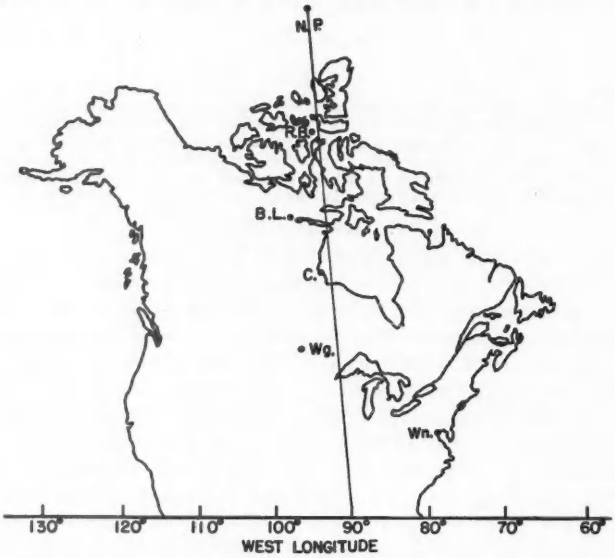

FIG. 1. Locations of ionosphere sounding stations.

(*a*) *Vertical Incidence Results*

Since there are no quantitative measurements of ionospheric absorption available for the stations, attention has been confined only to those occasions when no echoes were received. These occasions are denoted by the symbol *B* on the data sheets, and in the remainder of this paper, the occurrence of blackout at vertical incidence is synonymous with the occurrence of "*B*". A total loss of echo means a *B* on all data sheets, and apart from occasional errors, all sheets should give identical results. In fact the $f_{\min}$ sheets have been used for all stations except Washington for which, as the $f_{\min}$ was not available, the f_0F_2 sheets were used.

This approach is qualitative and does not show how much more power would be required to produce a visible echo, nor does it allow for possible influence of noise variations. The disturbances dealt with are known to be of considerable magnitude, and are essentially an on–off phenomenon. It is, therefore, felt that a considerable change in equipment performance, or considerable differences between stations, would not have a great influence on the results obtained.

The observations as taken at the stations record only 15 sec. of each hour. This makes studies of blackout duration precarious, but provides enough material for a statistical study of the probability of finding a blackout in progress at any random moment of sampling.

(*b*) *Reception of WWV*

Subjective measurements of the strength of signals received from WWV were also made hourly. These measurements were of no use as attenuation

measurements and, therefore, an on–off criterion similar to that used in the vertical incidence studies was adopted. At all stations, at least one of the transmissions on 2.5 Mc., 5.0 Mc., 10.0 Mc., and 15.0 Mc. was normally audible. A blackout is considered to have occurred when none of these frequencies could be heard at all.

(*c*) *Effect of f_0F_2 Variations*

Before discussing the results in detail one fact should be emphasized which may distort our qualitative picture. It is to be expected that the attenuation is produced by ionization in the lower part of the ionosphere, and that the absorption will vary roughly inversely as the square of the frequency (see Appleton (1)). Thus, for a given amount of ionization, corresponding to a fixed absorption on any one frequency, there is a greater likelihood of recording a blackout at times of low f_0F_2. The latter happens diurnally, seasonally, and with the long period solar activity variation. It will be shown that the observed frequency of blackouts does not change in sympathy with the f_0F_2 variations, and it is, therefore, considered that though there may be a small contribution from this cause, the blackout phenomenon is of a sufficiently "on–off" nature that the results would not be greatly altered if f_0F_2 variations were allowed for.

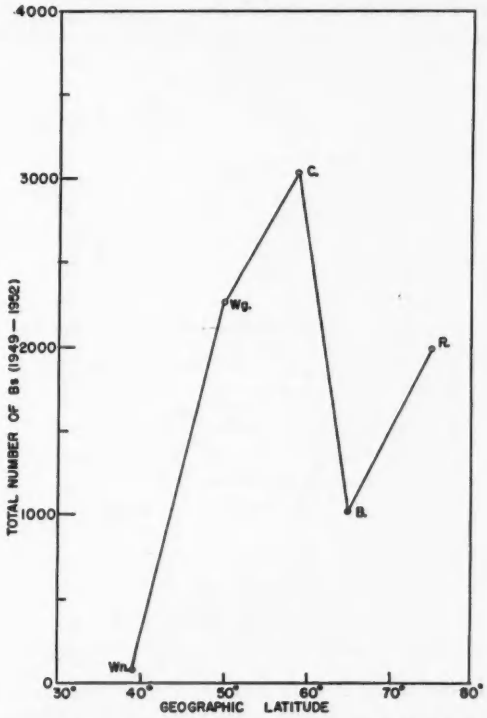

FIG. 2. Occurrence of blackouts as a function of latitude. Wn. Washington, Wg. Winnipeg, C. Churchill, B. Baker Lake, R. Resolute Bay.

III. ANALYSIS OF VERTICAL INCIDENCE DATA

(1) *The Geographical Distribution of Blackout*

In Fig. 2 the totals of '*B*s' recorded at the stations over the four-year period 1949 to 1952 have been plotted against geographical latitudes. This indicates that the occurrence of blackout is greatest near Churchill.

(2) *Temporal Variations*

(a) *Secular Variations*

The long term variations in the frequency of occurrence of blackout phenomenon are shown in Figs. 3 and 4 which show the yearly totals and the individual monthly totals of hours of blackout respectively, independently of time of day.

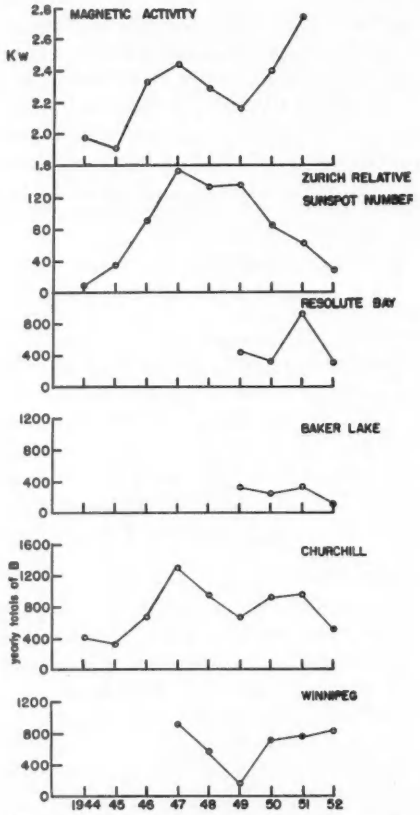

FIG. 3. Secular variation in frequency of occurrence of blackout.

Comparison of the blackout data with the Zurich relative sunspot number, also plotted in Fig. 3, shows that peak values of '*B*' occurred in 1947 at Churchill, suggesting some dependence of blackout phenomena on solar

activity. However, the data are too scanty to draw a definite conclusion, especially as the data for Baker Lake and Resolute Bay appear to have no

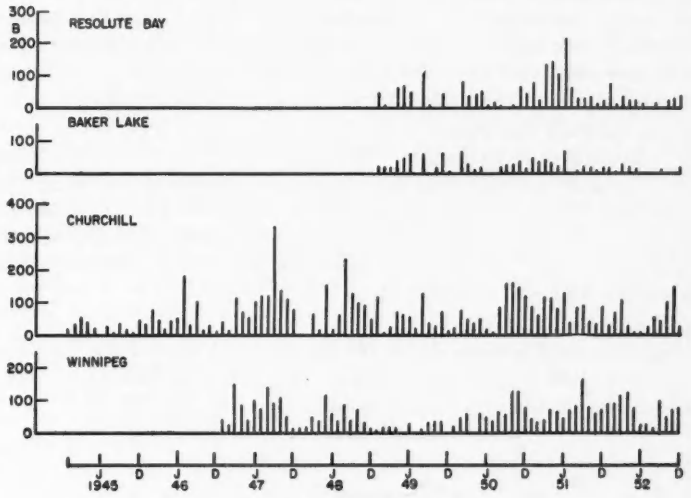

FIG. 4. Monthly totals of B.

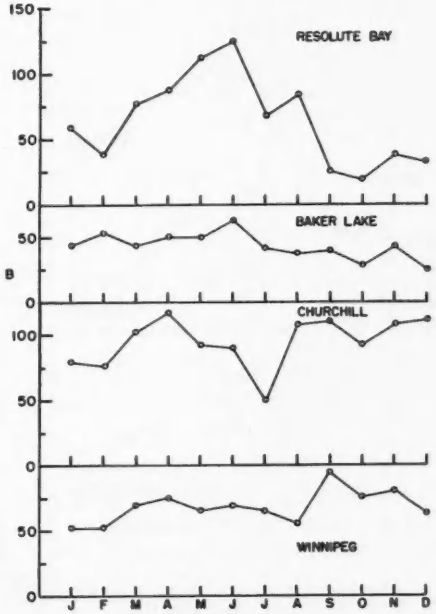

FIG. 5. Monthly mean totals of B (1949 to 1952).

connection with sunspots. A more interesting correlation is that between the occurrence of blackout and the mean annual values of the magnetic Kw figure, which are also plotted in Fig. 3. The correlations with blackouts at Churchill and Winnipeg are fair and the correlations with the data for Baker Lake and Resolute Bay give some support to the conclusion that, at least statistically, blackouts are associated with enhanced magnetic activity. The lack of detailed correlation may be more significant than the slight over-all correlation.

(*b*) *The Seasonal Variations*

The individual monthly totals of '*B*' are plotted in Fig. 4. There is a slight tendency for peak values to occur near the equinox months at the two southernmost stations. This is brought out in Fig. 5 in which the mean monthly totals for the four years 1949, 1950, 1951, and 1952 are plotted. There is very little seasonal variation at Baker Lake while at Resolute Bay there is a well-defined increase from winter to summer.

(*c*) *The Diurnal Variations*

In Fig. 6 the total numbers of '*B*s' occurring at each hour of the day over the years 1949 to 1952 are plotted. These graphs indicate a well-defined diurnal variation. The chief points to be noted are:

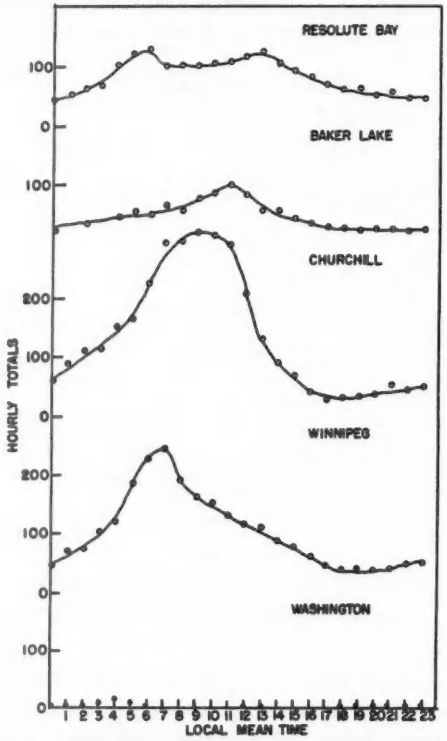

FIG. 6. Diurnal variation of frequency of occurrence of *B*.

(i) Daily maxima of occurrence in the morning, except at Resolute Bay, and minima of occurrence in the evening. A further study of the Resolute Bay data (not reproduced here) shows that the early morning maximum at Resolute occurs almost entirely in the winter months.

(ii) Although the total number of hours of occurrence of blackout at Washington is too small to construct a reliable diurnal curve, it is clear that most blackouts occur there during the hours of darkness. It may be inferred from this that the effects of sudden ionospheric disturbances of the Dellinger type are small since nearly the same number of Dellinger blackouts occur at all stations, except in the winter when the northern ones may be in darkness. Over the four-year period 1949 to 1952, 89 blackouts were recorded at Washington; 66 of these occurred between 00:00 hours and 06:00 hours. Thus even if all the remaining 23 were Dellinger type fadeouts they would constitute a very small fraction of the total numbers of blackouts observed at the Canadian stations.

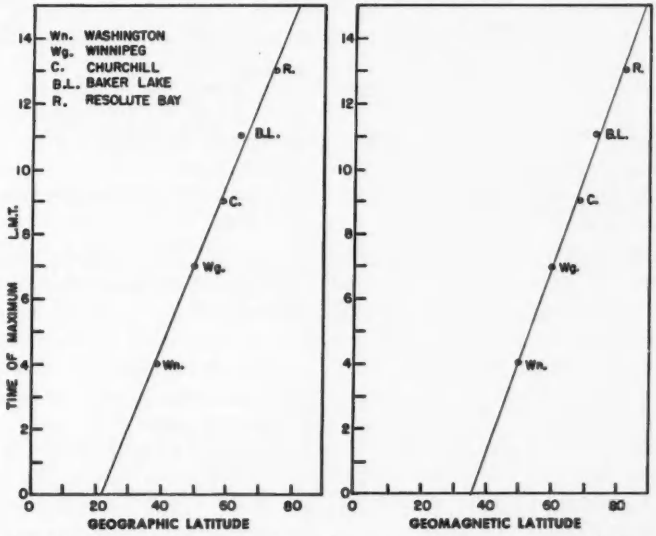

FIG. 7. Plot of times of diurnal maxima of occurrence of blackout against latitude.

(iii) A plot of local mean time of maximum occurrence against latitude gives a remarkably linear relation (Fig. 7) to which the second maximum at Resolute Bay fits quite well. The relation is

$$T = -5.7 + \tfrac{1}{4}\phi$$

when T is local mean time (hours) and ϕ is geographical latitude in degrees. This variation which is one hour in four degrees of latitude recalls the work of Stagg (3) on the diurnal variation of magnetic disturbances. He found a maximum in the late evening but states that "there is a disposition for the time of the maximum to be delayed with increasing latitude at the rate of approximately one hour every 5°".

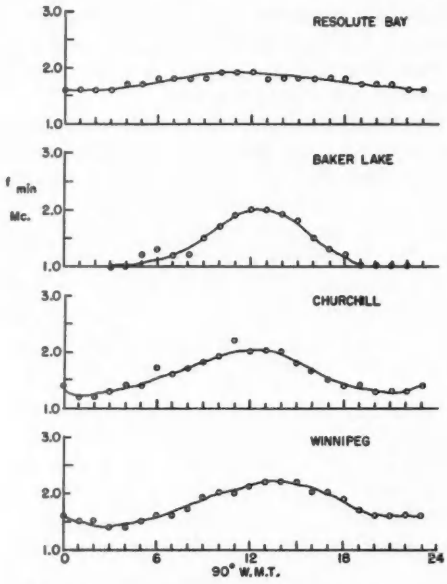

FIG. 8. Diurnal variation of the minimum frequency reflected from the ionosphere (hourly median values 1949 to 1952).

(iv) In order to see whether the diurnal variation in the occurrence of '*B*' is brought about by the normal diurnal variation of *D*-region absorption the hourly median values of the minimum frequency reflected from the ionosphere have been plotted in Fig. 8. Now, provided the equipment characteristics are constant, $f_{\min}$ is largely determined by ionospheric absorption. From Fig. 8 it will be seen that the maxima are attained near noon at all the stations. It may be concluded, therefore, that the observed diurnal variation is not produced simply by the variation in the position of the sun. It should be noted that the observed diurnal variation of $f_{\min}$ is diminished because the receiver gain is greater by day than by night but this would not affect the time of maximum value of $f_{\min}$.

(*3*) *Duration of Blackout*

It is of some interest to examine the distribution of the total time of blackout amongst the individual blackouts of various durations. To study this aspect of the problem the data have been classified according to the number of successive hourly records to which the symbol '*B*' is assigned. In Fig. 9 the distribution of the total blackout time has been plotted against the duration of the blackout. It is inherently assumed that if two successive hours are blacked-out the whole of the interval between is also blacked-out. Hence, the occurrence of the symbol '*B*' on n successive hours is interpreted as representing a blackout of length longer than $n - 1$ hours but shorter than $n + 1$ hours. It may be relevant to note here that a study of short duration blackouts suggests

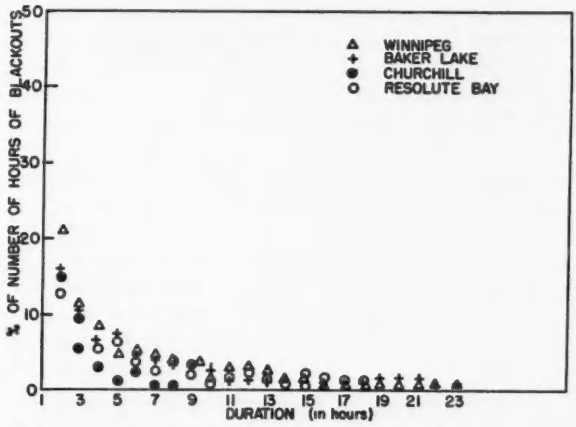

FIG. 9. Distribution of the total time of blackout amongst blackouts of different durations.

that the influence of sudden ionospheric disturbances of the Dellinger type is relatively slight.

From Fig. 9 it can be seen that the distributions of the total time of blackout amongst the individual blackouts are very similar at Winnipeg, Churchill, and Resolute Bay. There is a remarkable similarity in the relative distributions of short duration blackouts. Thus it appears that although a blackout may be less likely at Resolute Bay than at Churchill, the probability that it will last up to about 24 hr., say, is roughly independent of the locality. It appears, however, that there is a much larger percentage of one-hour blackouts at Baker Lake than elsewhere.

(*4*) *Extent of Blackouts*

It is seen that many more blackouts occur at some stations than at others, suggesting that such blackout phenomena are to a large extent localized in space. It is of considerable interest to study to what extent the occurrence of blackout at one station is reproduced at another. It is not possible in a reasonable space to consider all possible correlations and so attention will be confined to a detailed correlation between blackouts which occurred at Churchill and at Baker Lake for 1951.

Blackouts of all durations will be considered. For the present purpose it is convenient to express the correlation as the percentage of Baker Lake blackouts which occurred simultaneously at Churchill. The monthly values thus obtained are plotted in Fig. 10. In considering such correlation it must be remembered that even if the occurrence of blackouts were completely random at both sites, appreciable correlation would still be evident. Values to be expected in the case of random distributions can be estimated from the known frequencies and durations at the two stations, and are also included in Fig. 10. From this diagram it is clear that the observed values are significantly greater than would be expected on the basis of chance.

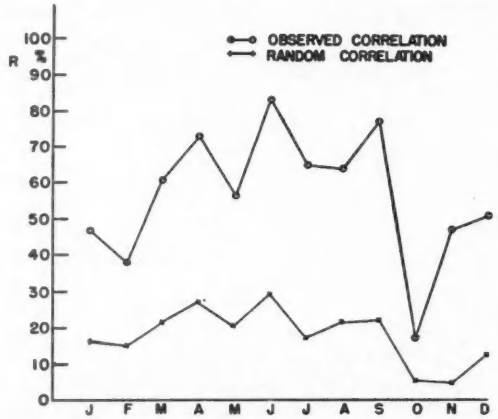

FIG. 10. Correlation between the occurrence of blackouts at Churchill and at Baker Lake.

$$R = \frac{\text{blackouts at Baker Lake which occurred simultaneously at Churchill}}{\text{total number of blackouts at Baker Lake}} \times 100.$$

It should be emphasized that most of the simultaneous occurrences of blackouts are due to long duration disturbances. Thus a study of blackouts of duration of one hour at all four stations for 1951 showed that there was no occasion on which a blackout of one-hour duration occurred at all four stations simultaneously.

It thus appears as if blackouts of short duration are essentially localized phenomena and that those of long duration are more widespread.

IV. RECEPTION OF WWV

(1) *Geographical Distribution*

To illustrate the geographical distribution the total number of hours of

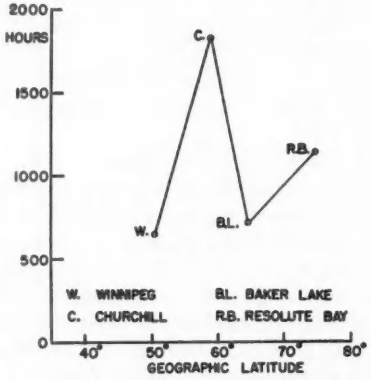

FIG. 11. Total numbers of hours of no reception of WWV 1949 to 1952.

blackout have been plotted against geographical latitude for the four Canadian stations. This is shown in Fig. 11. The variation of these blackouts with latitude bears a striking resemblance to that of the vertical incidence case shown in Fig. 2. There are two possible explanations for this similarity, namely,

(i) that reception of radio signals is governed by the state of the ionosphere near the receiving site,

or (ii) that both vertical incidence soundings and reception of long distance signals depend on operational conditions at the stations, e.g., noise level, operating procedure, etc.

The former explanation is very unlikely, since normally it is assumed that reception of long distance signals is governed by conditions along the propagation path. On the other hand the alternative explanation is quite likely, because both types of observations depend to some extent on the personal judgments of the observers.

(2) *Temporal Variations*

(a) *Secular Variations*

In Fig. 12 are plotted the total number of hours of blackout independent of time of day. It is clear that the long term variations at Winnipeg and at Churchill are in an opposite sense to the sunspot cycle variation. It appears,

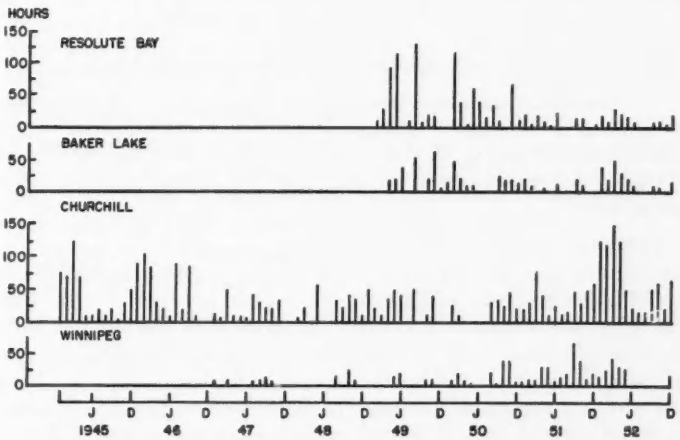

FIG. 12. Number of hours of no reception of WWV per month on frequencies of 2.5, 5.0, 10.0, 15.0 Mc.

therefore, as if these blackouts are due to electron limitation effects in the E and F regions. The data for Baker Lake and Resolute Bay are too meager to reach any definite conclusions but the frequency of occurrence of blackout at these stations appears to vary in phase with the sunspot cycle.

(b) *Seasonal Variations*

The mean monthly totals of hours of blackout for the years 1949 to 1952

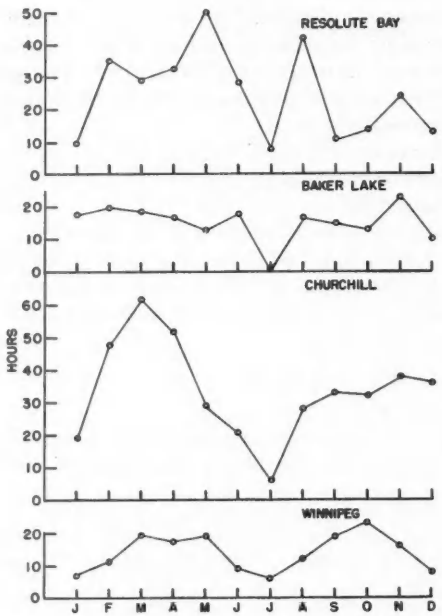

FIG. 13. Mean monthly totals of hours when WWV was not received 1949 to 1952.

inclusive are plotted in Fig. 13. While there appears to be little definite seasonal variation, it may be relevant to note the very low July values which occur at all four stations.

(*c*) *Diurnal Variations*

The diurnal variations of the frequency of occurrence of blackout are shown in Fig. 14 where the hourly totals over the four-year period 1949 to 1952 are plotted. Here again there is a marked similarity with the vertical incidence phenomenon, because most blackouts occur before noon, and the "double hump" is again evident at Resolute Bay. It is interesting to note, however, that the times of maximum frequency of occurrence are between one and two hours earlier than in the case of the vertical incidence curves. This is to be expected qualitatively from the geometry of the paths and from Fig. 7.

(*3*) *Duration of WWV Blackouts*

The data have been classified in the same way as for the vertical incidence data—see Section III (3). The distribution of the total time of blackout amongst the individual blackouts is shown in Fig. 15. The results are similar to the vertical incidence results. The probability of occurrence of short period blackouts is about the same at all four stations. Long period blackouts appear to be more frequent in the north than in the south.

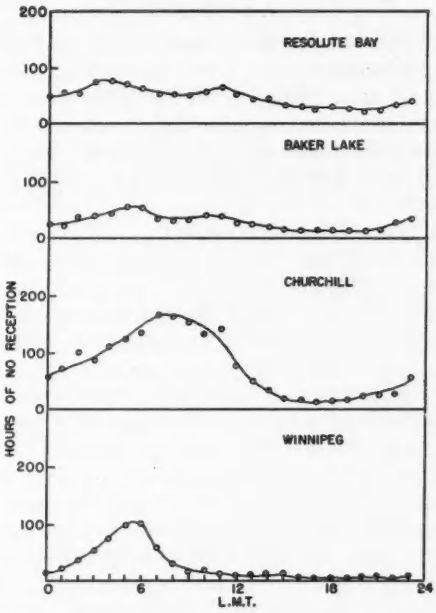

FIG. 14. Diurnal variation of the frequency of occurrence of blackouts of WWV.

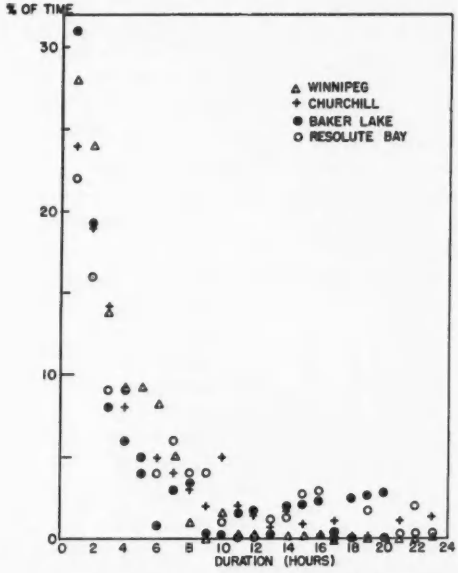

FIG. 15. Distribution of the total time of no reception of WWV amongst the individual blackouts of different durations.

V. SUMMARY

Although the data used for the present studies are somewhat uncertain because of their subjective nature, it is believed that the results will be of interest in a general way. Owing to the difficulty of making any accurate ionospheric absorption measurements in the Arctic regions, very little work has been done on radio wave attenuation at high latitudes. The present studies, therefore, constitute an attempt to obtain some useful information from available data.

Summarizing the most important results:

(i) For about 5 to 10% of the total time no echoes are obtained from the ionosphere at vertical incidence,
(ii) Blackouts usually occur in the morning hours,
(iii) The time of daily maximum of occurrence of blackouts is roughly a linear function of latitude,
(iv) There is no well-defined seasonal variation common to all stations,
(v) Short duration blackouts appear to be localized in space.

(ii), (iii), and (v) suggest that blackouts are caused by corpuscular action (Piggott (2)), rather than by ultraviolet radiation.

Probably the most interesting results are (ii) and (iii). The cause of the morning maximum and its dependence on latitude is not known. It is of course obvious that there must be some observer contribution to this essentially qualitative work, and it may be that it is significant. It is for this reason that the details of the apparent variation of blackout occurrence with latitude are not greatly emphasized. It is not believed that observer judgment would produce all the features obtained from the records and therefore these studies are presented to show that there certainly are phenomena worthy of more detailed and deliberate study.

REFERENCES

1. Appleton, E. V. Proc. Roy. Soc.(London), A, 162: 451. 1937.
2. Piggott, W. R. Nature, 171: 124. 1953.
3. Stagg, J. M. Proc. Roy. Soc.(London), A, 149: 298. 1935.

SOME MASS SPECTROMETRIC DATA ON PHOSPHORUS[1]

By Larkin Kerwin

ABSTRACT

Investigation of red phosphorus with a mass spectrometer shows the element to be monoisotopic to 1 part in 50,000. The relative abundances of the molecules resulting from electron bombardment of natural phosphorus are given, and the existence of the molecule P8 in nature is reported.

GENERAL

The most recent tables of isotopes, for example (6), give as a reference for the element phosphorus a paper by Aston (1) which dates back to 1920. He then reported the element as being apparently monoisotopic. An examination of his results leads to the conclusion that at the time he would not have observed any isotopes of mass greater than 31 whose abundance was less than about 2%, because of the presence of hydrides. His upper limit for isotopes of mass less than 31 would have been somewhat better. Since then, no one seems to have investigated further, although it was suggested by Naudé (3) that a heavier isotope might be present. There was an inviting vacancy at mass 33 until the recent discovery by Yaffe and Brown (7) of the radioactive P33. The atomic mass of phosphorus as determined by mass spectrographic measurements agrees so well with that resulting from other studies that it was generally considered improbable that other stable isotopes existed.

ISOTOPIC ABUNDANCES

We have recently checked the isotopic constitution of phosphorus, using the Laval inflection spectrometer (2). Phosphorus atoms are obtained by packing red phosphorus into a filament-furnace which then supplies atoms to the ionizing chamber of the spectrometer source. The element is found to be indeed monoisotopic to 1 part in 50,000 at least, isotopes 28, 29, 30, 32, 33, and 34 being absent to this extent.

MOLECULAR ABUNDANCES

Red phosphorus is generally conceded to exist in nature as the molecule P4. When evaporated from the hot filament and bombarded by the standard 70-volt electrons in the spectrometer source, the molecule decomposes. Over a moderate range of filament temperatures the abundances of molecular masses are in the following proportion:

P1 (mass 31):	16
P2 (mass 62):	50
P3 (mass 93):	6
P4 (mass 124):	100
P5 (mass 155):	0
P6 (mass 186):	0
P7 (mass 217):	0
P8 (mass 248):	0.5

[1]*Manuscript received August 19, 1954.*
Contribution from Physics Department, Faculty of Science, Laval University, Quebec, Que.

These data indicate that when the molecule splits, it usually splits in half under such conditions, the loss of a single atom being a less likely phenomenon, as is well known (4, for example). No P5 or P7 molecules were observed, and while there was possibly a trace of P6, its abundance would be less than our experimental error. The molecule found at mass 248 does not appear to be explainable by anything other than P8, although this molecule has not hitherto been observed. This experimental evidence for its existence confirms a suggestion made two years ago by Pauling and Simonetta (5). In discussing the question of phosphorus structure, they have proposed that red phosphorus is formed from white phosphorus. One of the bonds of the tetrahedron structure of the white phosphorus would break, and the open tetrahedrons would then join together in long chains, forming red phosphorus. These chains would preferably break up into molecules whose mass was a multiple of four, and thus P8, P12, etc., might be expected to be found in low abundances. The discovery of the P8 fragment confirms this suggestion which was made to explain certain anomalies in bond energy measurements. We have not looked for P12 (mass 372) but since it would probably be much less abundant than P8, it is doubtful whether we would have observed any.

The author is pleased to acknowledge the financial assistance of the Office de Recherches scientifiques of the Province of Quebec in carrying out this work.

REFERENCES

1. ASTON, F. W. Phil. Mag. 40: 632. 1920.
2. KERWIN, J. L. Rev. Sci. Instr. 21: 96. 1950.
3. NAUDÉ, S. M. Phys. Rev. 36: 346. 1930.
4. PASCAL, P. Traité de chimie minérale. Tome 3. Masson et Cie, Paris. 1932.
5. PAULING, L. and SIMONETTA, M. J. Chem. Phys. 20: 29. 1952.
6. SEABORG, G. T., HOLLANDER, J. M., and PERLMAN, L. Revs. Mod. Phys. 25: 469. 1953.
7. YAFFE, L. and BROWN, F. Phys. Rev. 82: 332. 1951.

A POTENTIAL FUNCTION FOR LIQUID HELIUM AT 0° K.[1]

By C. F. A. Beaumont

ABSTRACT

A new potential function for liquid helium is obtained by modifying the Margenau potential function and summing over a suggested structure for the liquid. The new potential function leads to fair agreement with the first peak of the radial distribution curve for liquid helium, with the isothermal compressibility, and with second virial coefficient data at high temperatures.

INTRODUCTION

It is the purpose of this note to determine a potential function between two helium atoms in liquid helium at 0° K. Corner and Lennard-Jones (1) have given a method for determining a potential function from an experimental radial distribution curve; however, the accuracy of the known radial distribution curve for liquid helium (4) does not justify the necessary calculations. Hildebrand and Wood (3), and Kerr and Lund (6), have given methods for determining a potential function of the Lennard-Jones form from radial distribution curves and relevant data. This form of the potential function is in terms of the maximum interaction energy and collision diameter of the atoms; however, it is desirable to obtain a potential function in terms of the fundamental forces acting between the atoms. Margenau (9), taking into consideration exchange forces and van der Waal's attractive forces, has determined the following potential function between two helium atoms:

$$[1] \qquad \phi(r) = [770e^{-4.60r} - 560e^{-5.33r} - (1.39/r^6) - (3.0/r^8)]10^{-12} \text{ ergs.}$$

For purposes of calculation Margenau states that one may use:

$$[2] \qquad \phi(r) = [770e^{-4.60r} - (1.39/r^6) - (3.7/r^8)]10^{-12} \text{ ergs.}$$

If [2] is summed over the structure suggested by Hutchison and Reekie (4) one obtains the total potential energy per mole of liquid helium, and a graph of this is plotted against the molecular volume in Fig. 1, curve A. The minimum value of -96.5 cal./mole occurs at a molecular volume of 16.2 cm.^{3} as compared with the accepted value of -14.2 cal./mole (5, pp. 230) at a molecular volume of 27.6 cm.^{3} (5, p. 207). This indicates that, for liquid helium, some additional repulsive potential has not been taken into consideration.

Yntema and Schneider (12) have developed an empirical potential function of the form

$$\phi(r) = ae^{-r/b} - (c_1/r^6) - (c_2/r^8)$$

to give a good fit with experimental virial data over the range 0° C. to 1200° C. c_1 was taken to be 1.24×10^{-12} erg-(Å)^6, as derived by London (7). c_2, calculated by Margenau (10), corresponding to the above value for c_1, has the value 1.89×10^{-12} erg-(Å)^8. a and b were determined by a trial and error

[1]*Manuscript received September 2, 1954.*
Contribution from the Royal Military College, Kingston, Ontario.

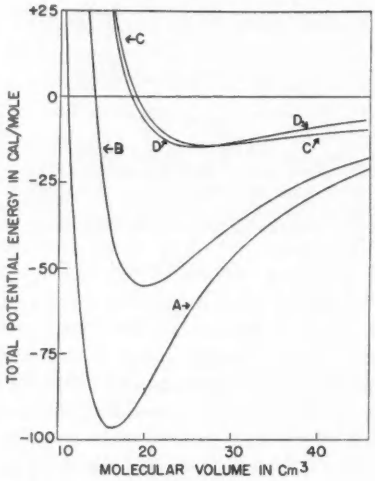

FIG. 1. Curves A, B, C, and D give the potential energy per mole as a function of the molecular volume of liquid helium at 0° K. These curves are obtained by a summation of equations [2], [3], [10], and [11], respectively, over the suggested structure (4) for liquid helium.

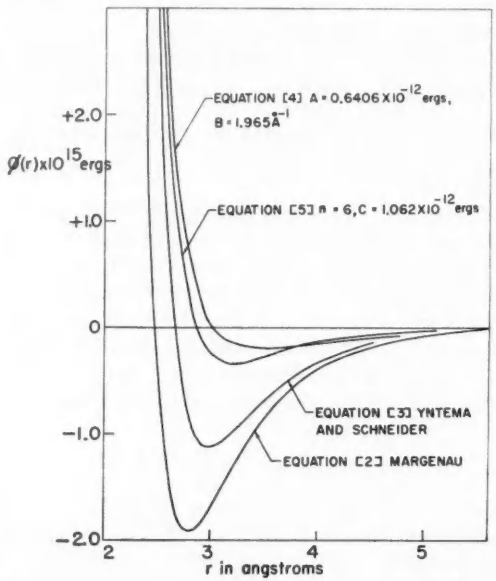

FIG. 2. These curves show the potential function between two helium atoms as given by Margenau's theoretical potential function [2], Yntema and Schneider's empirical potential function [3], and the two potential functions [4] and [5], obtained by combining Margenau's potential function with experimental data at 0° K.

process to obtain a satisfactory fit with the virial coefficient data. The final expression for the potential function was

[3] $\phi(r) = [1200e^{-r/0.212} - (1.24/r^6) - (1.89/r^8)]10^{-12}$ ergs.

Summing [3] over the suggested liquid helium structure gives a minimum value of -55.1 cal./mole at a molecular volume of 19.7 cm.^{3}, curve B, Fig. 1.

Equations [2] and [3] are shown in Fig. 2 with minima occurring at 2.8 Å and 3 Å respectively. According to the first peak of the radial distribution curve for liquid helium (4) the minimum should occur at about 3.44 Å.

DEVELOPMENT

Equation [2] will be modified by adding to it an additional repulsive term either of the form Ae^{-Br} or of the form C/r^n. Equation [2] then becomes

[4] $\phi(r) = Ae^{-Br} + [770e^{-4.60r} - (1.39/r^6) - (3.7/r^8)]10^{-12}$ ergs

or

[5] $\phi(r) = C/r^n + [770e^{-4.60r} - (1.39/r^6) - (3.7/r^8)]10^{-12}$ ergs.

Considering equation [4] first, it is summed over the suggested structure and one obtains

[6] $$W(r) = \{4A(e^{-0.8909BR} + 1.5e^{-1.260BR} + 2e^{-1.543BR} + 3e^{-1.782BR}) + [3080(e^{-4.098R} + 1.5e^{-5.796R} + 2e^{-7.098R} + 3e^{-8.196R}) - (15.254/R^6) - (42.476/R^8)]10^{-12}\} N/2 \text{ ergs/mole},$$

where $W(R)$ is the total potential energy per mole, R^3 is the volume per atom in cubic angstroms, and N is Avogadro's number. The summation for the attractive terms is taken over the 20 nearest neighbors, while for the repulsive terms it is sufficient to sum over the first four nearest neighbors. From the facts that $W(R) = -14.2$ cal./mole at $R = 3.578$ Å (molecular volume $= 27.6$ cm.^{3}) and $dW(R)/dR = 0$ at $R = 3.578$ Å one obtains two equations for A and B which, on solving, yield the values

$$A = 0.6406 \times 10^{-12} \text{ ergs}, \qquad B = 1.965 \text{ Å}^{-1}.$$

Curve C, Fig. 1, is a graph of [6] using these values for A and B.

At this stage, the isothermal compressibility χ_T may be computed from

[7] $$1/\chi_T = V(dR/dV)^2 (d^2W(R)/dR^2)$$

giving $\chi_T = 7.2 \times 10^{-3}$ atm.$^{-1}$ as compared with the extrapolated value of 12.5×10^{-12} atm.$^{-1}$ (2). For a general value of n, equation [5] is not simply summed over the crystal lattice to obtain an equation similar to [6]. However, summing over the lattice for various particular values of n one may determine the corresponding values for C from $W(R) = -14.2$ cal./mole at $R = 3.578$ Å. The correct n is the one giving a minimal value for $W(R)$ at $R = 3.578$ Å, and this turns out to be $n = 6.65$. Owing to the difficulties of summation for n not an integer, n will be given the value 6 or 7. $n = 7$ yields an isothermal compressibility of approximately 5×10^{-3} atm^{-1}. For $n = 6$, C has the value 1.062×10^{-12} ergs, giving an isothermal compressibility of 8.4×10^{-3} atm^{-1}. Curve D, Fig. 1, shows the total potential per mole for the case $n = 6$. From

Fig. 2 it may be seen that equation [4] has a minimum at $r = 3.45$ Å, while equation [5] (with $n = 6$) has a minimum at $r = 3.2$ Å. Equation [4] is in close agreement with the first peak of the radial distribution curve for liquid helium.

As a further check on the values $A = 0.6406 \times 10^{-12}$ ergs, $B = 1.965$ Å^{-1}, or $n = 6$, $C = 1.062 \times 10^{-12}$ ergs, the second virial coefficients for high temperatures may be computed from the classical expression

$$B(T) = 2\pi N \int_0^\infty (1 - e^{-\phi(r)/kT}) r^2 \, dr, \tag{8}$$

where $B(T)$ is the second virial coefficient, N is Avogadro's number, and k is Boltzmann's constant. A comparison is made with experimental values (11) in Table I.

TABLE I

COMPARISON OF CALCULATED VALUES OF SECOND VIRIAL COEFFICIENTS FOR LIQUID HELIUM

Temp., deg. C.	$B(T)$ in cm.^{3}/mole		
	Measured values	Equation [4]	Equation [5]
0	11.77	12.96	13.06
300	10.76	11.47	11.05
600	9.82	10.30	9.97

One may be tempted to call the difference between the potential energy due to summing equation [2] over the lattice and the potential energy resulting from summing [4] or [5] over the lattice the zero point energy of liquid helium. However, one must note that additivity is assumed throughout the above

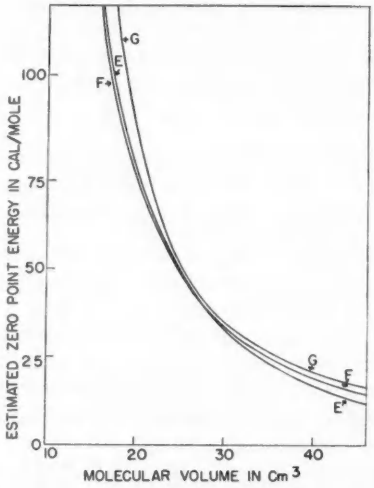

FIG. 3. Curves E and F are an estimate of the zero point energy of liquid helium obtained by taking the difference between curves A and C and curves A and D respectively in Fig. 1. Curve G is the zero point energy as computed using London's formula [9] taking $d = 2.55$ Å.

work. Margenau (9) has shown for helium atoms that additivity is almost legitimate for first-order exchange forces and van der Waal's attractive forces. Additivity does not necessarily hold when one considers the zero point energy as a repulsive potential energy. Hence curves E and F in Fig. 3, obtained by taking the difference between curves A and C and curves A and D respectively in Fig. 1, may at best be considered only as a rough approximation to the zero point energy. It is interesting to compare these two curves with curve G as computed from London's formula (8)

$$[9] \qquad E_o = h^2 d/2\pi m(R - 2^{-1/6}d)^2\,(R + kd),$$

where $k = 0.713$, R is the mean distance between atoms, and d is the diameter of the atoms. In calculating curve G, d is taken as 2.55 Å. At a molecular volume of 27.6 cm.^{3} curves E and F give an estimated value of 39.5 cal./mole for the zero point energy, while London's formula gives a value of 41 cal./mole.

DISCUSSION

Two possible potential functions for liquid helium have been determined:

$$[10] \qquad \phi(r) = [0.6406e^{-1.965r} + 770e^{-4.60r} - (1.39/r^6) - (3.7/r^8)]10^{-12} \text{ ergs}$$

and

$$[11] \qquad \phi(r) = [(1.062/r^6) + 770e^{-4.60r} - (1.39/r^6) - (3.7/r^8)]10^{-12} \text{ ergs}.$$

These equations have been constructed to give the correct latent heat and molecular volume at 0° K. Owing to the fact that n is integral, equation [11] is not quite correct, giving a latent heat of -14.5 cal./mole at a molecular volume of 25.5 cm.^{3} With regard to the isothermal compressibility, a sensitive quantity, both [10] and [11] yield values which are of the correct order of magnitude. Also, from Table I, the agreement with second virial coefficient data from 0° C. to 600° C. is within 11% error and the error decreases with increasing temperature. Finally the position of the minimum of equations [10] and [11] should be about 3.44 Å as determined by the first peak of the radial distribution curve for liquid helium. The minimum of equation [10] occurs at 3.45 Å and that of equation [11] at 3.2 Å. Evidence points slightly in favor of equation [10] as being the more acceptable potential function between two helium atoms in liquid helium.

The author wishes to thank Dr. T. S. Hutchison and Dr. D. C. Baird for helpful discussions.

REFERENCES

1. CORNER, J. and LENNARD-JONES, J. E. Proc. Roy. Soc. (London), A, 178: 401. 1941.
2. EDWARDS, M. H. Ph.D. Thesis, University of Toronto, Toronto, Ont. 1953.
3. HILDEBRAND, J. H. and WOOD, S. E. J. Chem. Phys. 1: 817. 1933.
4. HUTCHISON, T. S. and REEKIE, J. R. Phys. Rev. 92: 827. 1953.
5. KEESOM, W. H. Helium. Elsevier Publishing Co., Inc., Amsterdam. 1942.
6. KERR, R. H. and LUND, L. H. J. Chem. Phys. 19: 50. 1951.
7. LONDON, F. Z. Physik, 63: 245. 1930.
8. LONDON, F. Proc. Roy. Soc. (London), A, 153: 576. 1935.
9. MARGENAU, H. Phys. Rev. 56: 1000. 1939.
10. MARGENAU, H. Revs. Mod. Phys. 11: 1. 1939.
11. YNTEMA, J. L. and SCHNEIDER, W. G. J. Chem. Phys. 18: 641. 1950.
12. YNTEMA, J. L. and SCHNEIDER, W. G. J. Chem. Phys. 18: 646. 1950.

IONIZATION PROBABILITY CURVES USING AN ELECTRON SELECTOR

RESULTS ON N_2^+, N^+, Xe^{++} [1]

By E. M. Clarke[2]

ABSTRACT

An apparatus consisting of an electron energy selector built into a mass spectrometer is described. With it, initial ionization yield curves may be obtained. The interpretation of these curves is discussed, and the following new measurements reported:

Nitrogen: $^2\Pi_u$ state of N_2^+ at 1.0 ± 0.2 ev. above initial ionization potential;
$^2D^0$ state of N^+ 2.36 ev. above the $^4S^0$ state;
$^2P^0$ state of N^+ 1.4 ev. above the $^2D^0$ state;
energy of dissociation of N_2: 9.80 ev.

Xenon: second ionization potential of Xe: 21.09 ev.

A. INTRODUCTION

The measurement of ionization and appearance potentials by electron impact methods has been practised for a considerable time (17, 12). Ideally, this technique would consist in repeated bombardment of a single atom with a single electron, and gradual increase of the energy of the latter until the atom was seen to ionize. In practice, one must bombard many atoms with many electrons, and so several complicating factors are introduced:

Experimentally:

(*a*) The electrons emitted from a source generally do not have all the same energy. For instance, those from a hot filament have a Maxwellian energy distribution.

(*b*) At the onset of ionization it is necessary to detect very small quantities of ions. Thus the threshold of the detector may introduce an experimental difficulty similar to that described in (*d*) below.

In interpreting the measured curves:

(*c*) There may be several ionization processes, to various energy levels. If the levels are close together they can produce an effect similar to that due to (*a*).

(*d*) Even for a single process, and monoenergetic electrons, the quantity of ionization produced after ionization has set in is not definitely known. Wannier (18) has theoretically predicted a near-linear function, which is not discontinuous however, but asymptotic to the potential axis, as in Fig. 1. If this is so, a precise experimental measurement of the onset of ionization is theoretically impossible, unless this function is known in advance.

To illustrate the effect of these four complicating factors, consider a typical ionization probability curve, such as in Fig. 2. Then the point P where the curve leaves the axis is quite indeterminate. It depends on the sensitivity of the detector, and the theoretical nature of the curve. The curved region R may

[1] *Manuscript received September 10, 1954.*
Contribution from the Department of Physics, Faculty of Science, Université Laval, Québec, P.Q.
[2] *On leave of absence from St. Francis Xavier University, Antigonish, N.S.*

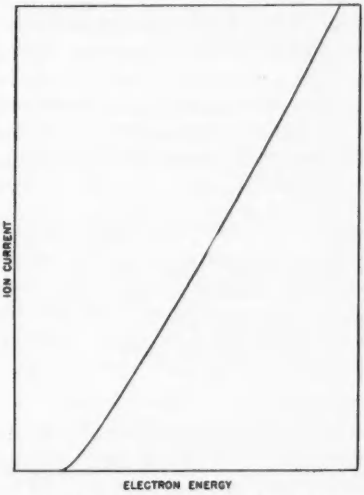

FIG. 1. Theoretical ionization yield according to Wannier.

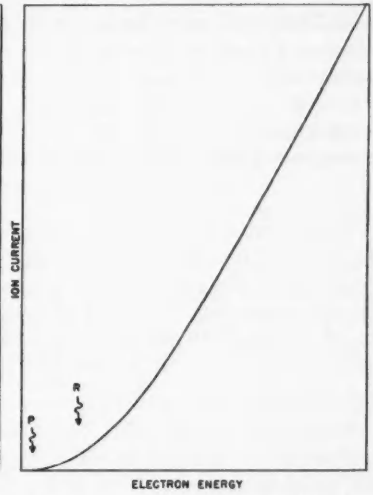

FIG. 2. Typical experimental ionization yield.

be caused by the true nature of the curve (Fig. 1), the energy spread of the electrons, or a succession of ionizations to various energy levels, masked by the former two.

Therefore, in order to determine ionization potentials:

(*A*) Experimental techniques must be used which effectively reduce the electron energy spread, and improve the limit of sensitivity of the detector, until these factors no longer mask the various ionization processes. This however can never permit the precise determination of the ionization potential if the actual ionization curve is an unknown asymptotic function as described above.

(*B*) So an arbitrary interpretation of the experimental curve such as will yield useful information must be made. The worth of any such arbitrary method is measured by the success with which it gives results which agree with spectroscopic values.

As far as experimental techniques are concerned, Fox *et al.* (4) and Morrison (14) have recently developed methods which have had considerable success in overcoming the electron energy spread, and in enabling them to separate out various ionization processes.

As regards the arbitrary interpretation of the measured curves, this is currently being done by one of several methods:

(i) The approximate point at which the curve leaves the axis is chosen (vanishing current method).

(ii) The approximately linear section of the curve is extrapolated to meet the axis (linear extrapolation method).

(iii) The difference in potential of the ionization curves of two elements is plotted as a function of intensity and extrapolated to zero intensity (Warren method (19)).

It is the purpose of this paper to describe a new apparatus for overcoming the experimental difficulties mentioned, to discuss the various arbitrary methods of interpreting the curves obtained, and to report some new measurements.

B. APPARATUS

The apparatus used in this work consisted of a 127° electrostatic velocity selector which provided a beam of nearly monoenergetic electrons (9), followed by a grid to accelerate these electrons to energies sufficient to ionize the sample. The ions formed by this source were separated by an inflection mass spectrometer of very high luminosity (11) and detected by a 12-stage Allen-type Be-Cu multiplier (1, 15), followed by a vibrating reed chart recorder (16).

Electron Selector

The electron selector, Fig. 3, was constructed of stainless steel strips set into grooves cut in plates of Mycalex K. Electrons from a wolfram filament *A* were accelerated by 3 v. between the filament and the first 0.7 mm. by 4 mm. slit of the selector *S*. The inside curved deflection plate *B*, of 1 cm. radius, was maintained at +4.5 v., while the outside curved deflection plate *C*, of 1.5 cm.

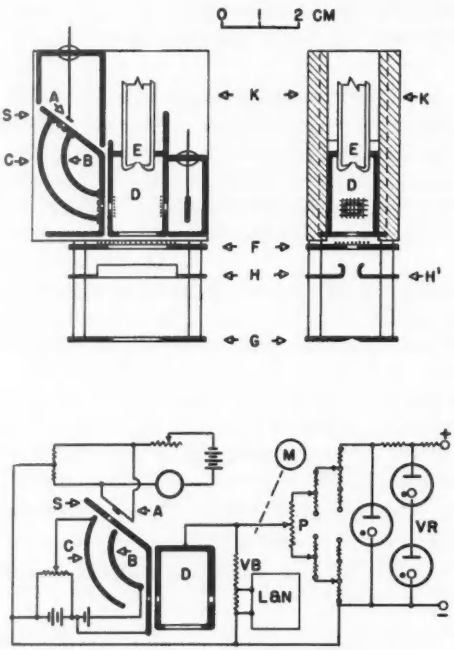

FIG. 3. Electron energy selector.

radius, could be varied from 0 to +3 v., the usual value for optimum work being about +1.3 v. as will be seen. Both slits were adjustable, and at the same potential, being mounted on the same strip of stainless steel *S*. The additional energy necessary to cause ionization was given to the electrons by the potential difference between the 0.5 mm. by 3 mm. exit slit of the selector and the entrance grid of the ionization chamber *D*. A trap *T* was provided to measure the electron current, and when not in use was grounded to the case *D*. The trap current was found to be independent of the electron energy over a range of from 7 to 60 v.

The Mycalex plates were coated with graphite on the area between the deflecting plates to prevent surface charges and to provide a more uniform field. A cylindrical magnetic shield 0.5 in. thick and 3 in. long in the form of a laminated transformer core was placed around the outside of the spectrometer head.

Gas was admitted to the ionization chamber through a 25 μ quartz leak *E*. The ions formed were drawn out from *D* by the fringing field from the grid *F*, and then accelerated by 1000 v. into the spectrometer entrance slits *G*. Plates *H* and *H'* were used for focusing and alignment. The grids on the ionization chamber *D* and the draw-out grid *F* were of 95% transparency wolfram mesh.

The ionization voltage was stabilized by cascaded voltage regulator tubes *VR*, and adjusted by a step potentiometer, followed by a potentiometer *P* driven by a motor *M*, so arranged as to give sweeps of 2, 4, or 8 v. in five minutes. The voltages were measured with a volt box and Leeds and Northrup potentiometer, calibration marks being keyed onto the motor-driven chart at 0.20 or 0.50 v. intervals.

The approximate electron energy distributions furnished by the selector were examined by placing a negative bias of 13.5 v. on the trap and measuring

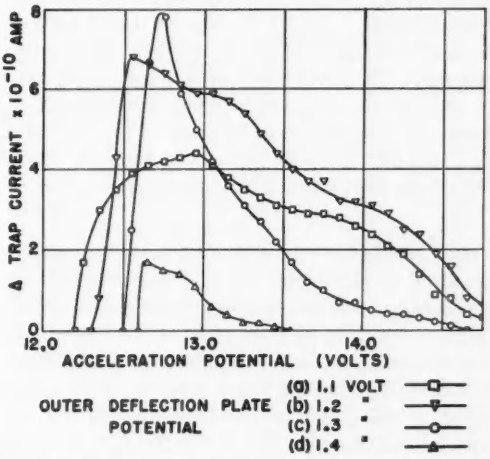

FIG. 4. Energy distribution furnished by electron selector.

the trap current as a function of the acceleration potential. The total current curve so obtained was differentiated to obtain the electron energy distribution as shown in Fig. 4.

Here we see the energy distributions furnished by the selector for different settings of its outer deflection plate voltage. All of the curves show a sharp cutoff on the high-energy side of the distribution, and it is this characteristic which is most useful, since it is the long high-energy tail of the Maxwellian distribution which causes most of the experimental troubles. The cutoff on the low-energy end is due to the relatively sharp cutoff inherent in the Maxwellian distribution itself at low energies. Adjusting the outer electrode voltage selected different parts of the Maxwellian distribution, and thus more or less energy spread was selected. In the figure, total distributions of from 0.8 to 2.5 ev. are obtained. Thus the combination of selector characteristics and Maxwellian distribution of the initial energies results in a smaller energy spread than would be expected.

In addition to this, since the probability of ionization increases with excess voltage, the high-energy electrons which appear at the left of the graph are more efficient in producing ions, and thus distributions such as Fig. 4(*c*) and (*d*) are effectively narrower than they appear. It has been found useful in this work to take as a measure of the energy distribution the difference in ionization potential as found by linear extrapolation and by the vanishing current method. On this basis, distributions as low as 0.2 ev. have been obtained. Generally the outer deflection plate was operated at 1.30 v., the trap current was about 10^{-8} amp., and the energy distribution about 0.3 ev.

Mass Spectrometer

To operate a mass spectrometer with a trap current of 10^{-8} amp. requires special care. The fringing field from an external electrode was used to draw out the ions instead of the usual repeller plate, this being found more efficient when it was desired to have minimum effect on the electron energy. The grid on the draw-out electrode served merely to shield the source from the main accelerating potential. The geometric and electrical settings of the focusing slits projected ions from a wide angle onto the spectrometer entrance slit. The inflection spectrometer was capable of focusing at 12° ion beam onto the detector. For stability, the exit slit was opened so that the resolving power was about 80 instead of the instrument's normal 300.

Detector

In spite of the precautions mentioned, it was necessary to measure ion currents of from 10^{-18} to 10^{-16} amp. The Be-Cu multiplier used was sensitized in an argon atmosphere, and provided a gain of about 10^6 when operated at about 250 v./plate. Its output of from 10^{-12} to 10^{-10} amp. was measured by a vibrating reed electrometer with an input resistor of 10^9 ohms. This combination was found capable of detecting single ions, and in the range of ion currents actually measured, a 500 picofarad condenser across the electrometer input served to smooth out statistical variations in the current. Optimum operation of the multiplier was achieved by shielding it from the spectrometer magnet

with a 0.5 in. soft iron shield, and positioning a small permanent magnet outside the multiplier. These latter precautions improved performance about 60 times.

C. INTERPRETATION

Fig. 5 showing measurements made on xenon and Fig. 6 giving some results with NO will serve for the discussion of the interpretation of the experimental curves.

Curves *a*, *b*, and *c* of Fig. 5 show ionization probability curves of xenon made at sensitivities of 1, 1/10, and 1/100. They illustrate the weakness of using the vanishing current method of interpreting the curves. Not only are the initial points absolutely indeterminate, but they give relative values of ionization potential which vary approximately 0.16 ev. for each factor of 10 in the sensitivity.

The linear extrapolation method applied to curves *b* and *c* gives values within about 0.02 v. of each other, and is therefore more reliable. However the method cannot be used at high sensitivity, such as for curve *a*, because here the line is curved throughout its length, and there is no straight portion to extrapolate. In these curves, the electron energy distribution is seen to be about 0.3 ev. For this method then, too great sensitivity must not be used if good results are to be obtained. Ten runs made on krypton gave in this way a precision of measurement of about 0.013 ev.

Using a Warren plot, the krypton curves gave a precision of measurement of about 0.010 ev. However an extra manipulation was necessary to replot the curves so as to have the same final slope.

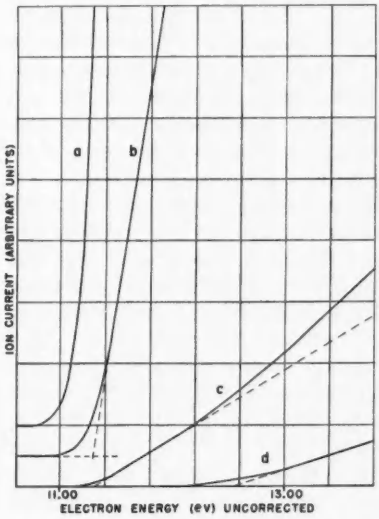

FIG. 5. Initial ionization yield of Xe^+.

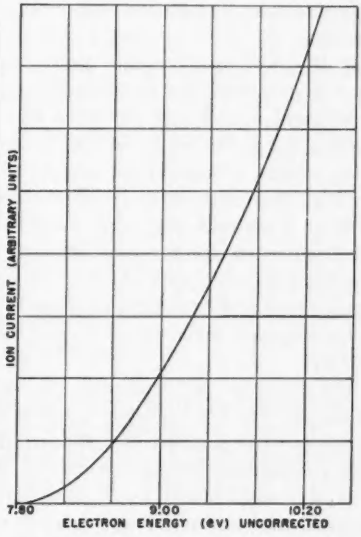

FIG. 6. Initial ionization yield of NO^+.

To summarize, the vanishing current method is poor, the linear extrapolation method is good if the sensitivity is not too high, and the Warren method gives a little better result for some extra work.

A method not reported to date is the application of Wannier's theory to the curves. As a matter of fact, the linear portions of the curves were rarely perfectly straight, but became more so when replotted to give the 1.127 root on the basis of Wannier's prediction that the initial probability should follow a 1.127 power law. Using this method, the above runs on krypton gave a precision of measurement of 0.009 ev. However this is not conclusive proof of Wannier's thesis, as both the electron distribution and the use of the condenser filter might tend to cause a similar curvature.

So far we have dealt with single processes, where the electron energy distribution, if small, is of no consequence. Curve 5*c* shows that the initial approximately linear section for xenon is followed by a second curved and linear section, indicating that another process of ionization has set in, leaving the Xe^+ in the $^2P_{1/2}$ instead of the $^2P_{3/2}$ state. Curve 5*d* corresponding to this second process was obtained by subtraction of the linear extrapolation of the first straight section from the original combined curve. In five runs, using linear extrapolation, the mean difference for the two ground states of Xe^+ was calculated to be 1.20 ± 0.05 ev., instead of the spectroscopic value of 1.31 ev. This, along with the unduly long tail of the second process, indicates that the graphs were slightly curved. However the assumption that they were of the 1.127 power gave values that were almost as much too high. This figure compares with the xenon curves obtained by Fox *et al.* (4) using a pulsed grid method to obtain nearly monoenergetic electrons.

In this case the two processes were clearly separated, but if the separation is less than the electron energy spread, or than the initial Wannier curvature, then the processes become masked. This is illustrated by argon which also has two processes, but separated by only 0.18 ev., so that they merge to give a curve similar to 5*b*, instead of 5*c*. Here linear extrapolation will give an intermediate value for the ionization potential (12). This is verified in the present work: three runs on argon give by linear extrapolation a difference of 3.70 $\pm .02$ ev. compared with xenon, instead of the spectroscopic value of 3.63 ev., an error of approximately half the 0.18 ev. in the proper direction. On the other hand, when an argon curve assumed to be made up of two processes and a xenon curve arbitrarily chosen to have a slope equal to one-half that of the argon curve and hence approximately equal to that of the initial process only were compared using a Warren plot, the correct difference was obtained within 0.02 ev.

The curve for NO, shown in Fig. 6, may be treated similarly. Here, at low sensitivity, the line is still curved throughout, and actually fits a 1.7 power law. However in this case the curvature is due to the multiplicity of vibrational states separated by approximately 0.3 ev., and therefore masked by the electron energy spread used. However, as in the case of argon, useful information may be obtained. It is known that the initial 0.5 ev. of the argon curve is made up of two processes; and also it is known (2) that there are two processes

for NO in the first 0.5 ev. above threshold. Therefore it is interesting to compare these initial sections of the two curves. When this was done by a Warren plot, the ionization potential of NO was found to be 9.24±.04 ev. which corresponds to the 9.23±.02 value found by Watanabe *et al.* (20) using a photoionization technique. Hagstrum's value of 9.4 ev. (5) approaches the above value if his neon curve is reduced to correspond to the slope of only the initial processes in NO.

D. NEW MEASUREMENTS

Nitrogen: N^+ from N_2

Fig. 7 shows a typical curve of N^+ obtained from N_2. There are two distinct breaks in the curve. The first occurs at 2.36±0.07 ev. above the initial ionization potential (mean from 10 curves by the linear extrapolation method) and

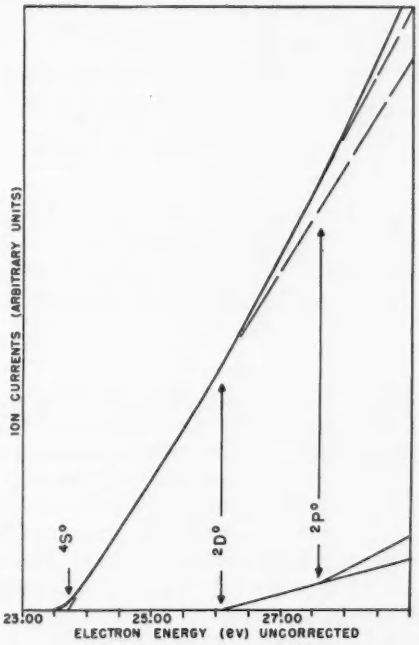

FIG. 7. Initial ionization yield of N^+ from N_2.

the second occurs 1.4±0.1 ev. higher. This corresponds very closely to the spectroscopic value of 2.38 ev. for the difference in energy between the $^4S^0$ and $^2D^0$ levels of N, and approximately to the additional 1.19 ev. required for the $^2P^0$ level. From this we may calculate the energy of dissociation of N_2 as follows. In the process

$$N_2(X^1\Sigma_g^+) \rightarrow N^+(^3P) + N(^4S^0)$$

(notation as in Hagstrum (5)) we have the energy relation

$$A_0 = D(N_2) + I(N) + E_e(N^+) + E_e(N)$$

where A_0 = appearance potential, D = dissociation energy,

I = ionization potential, E_e = electronic excitation energy;

whence

$$D(N_2) = A_0 - I(N) - E_e(N^+) - E_e(N).$$

The mean value for A_0 taken from several curves as in Fig. 7 and compared with xenon as standard is 24.35±0.1. The ionization potential of N is known to be 14.54 (7). $E_e(N^+)$ and $E_e(N)$ are zero for the onset of the process, and so we have:

$$D(N_2) = 24.35 - 14.54 - 0 - 0$$
$$= 9.81 \text{ ev.}$$

Similarly in the second process

$$N_2(X^1\,\Sigma_g^+) \rightarrow N^+(^3P) + N^*(^2D^0),$$

we have A_0 equal to 26.71±0.1 from measured curves as in Fig. 7, and so:

$$D(N_2) = 26.71 - 14.54 - 0 - 2.38$$
$$= 9.79 \text{ ev.}$$

This result favors the 9.764 ev. spectroscopic value in agreement with Douglas (3), and the value 7.4 ev. as reported by Hagstrum (5) would appear to be erroneous. Examination of Hagstrum's paper indicates that he placed too much reliance on a value for the heat of formation of NO taken from Hanson (6).

Nitrogen: N_2^+

In Fig. 8 we see the initial part of the ionization curve of N_2^+ from N_2. The curvature from A to C is attributed to the excitation of the vibrational levels of the ionized molecule, which are known from spectroscopy (3). Thus if this were the only process involved, the curve would continue in a fashion similar to that of NO (Fig. 6) as shown by the dotted line. Instead, the curve transforms into a linear function of the excess voltage along EF. If the curvature due to the vibrational levels is ignored for the moment, the portions AB and EF of the curve may be extrapolated to meet at D, where another process evidently sets in. Because of the nature of the curve, D may not be fixed more accurately than 1.0±0.2 ev. above the initial ionization potential. However this agrees with the break found by Fox's method by Frost and McDowell (to be published) at 1.20 ev. and attributed by them to the $^2\Pi_u$ state recently identified by Meinel (13) and Dalby and Douglas (2) and situated at 1.115 ev. above the 15.576 ev. first ionization level. This interpretation indicates that once the electrons have sufficient energy to excite the $^2\Pi_u$ state, then vibrational levels are no longer excited. This is not in disagreement with optical spectrometry, where the bands attributed to the $^2\Pi_u$ state have recently been found to be quite weak (2).

That part of the curve from C to E is attributed to excitation of vibrational levels by the electrons in the tail of the distribution of Fig. 4(c) which have not enough energy to excite the $^2\Pi_u$ state. This effect shifts the apparent break from D to E. The curves of Frost and McDowell show a relatively low ionization for the first process, and relatively strong ionization for the second process. The reverse is true in the present work, and is believed to be due to the relatively wide band of electrons exciting a greater number of resonant vibrational states at one time.

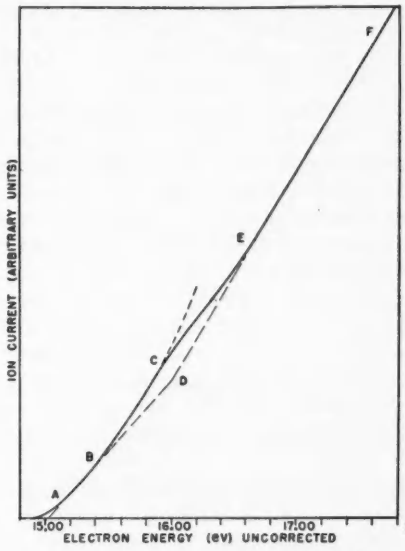

FIG. 8. Initial ionization yield of N_2^+.

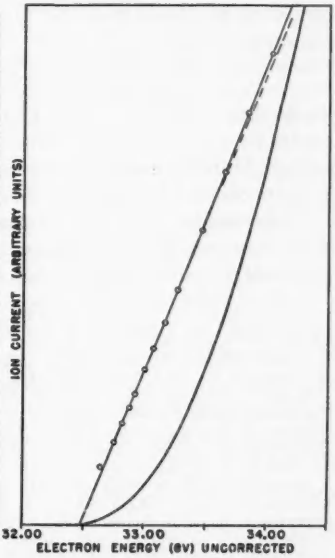

FIG. 9. Initial ionization yield of Xe^{++}.

Xenon: Xe^{++}

Fig. 9 shows a typical ionization curve for Xe^{++}. The line is curved throughout, and so the usual methods of interpreting it may not be used. However this curvature is not due to a multiplicity of states, as it is known from spectroscopy that the first two excited states of this ion are the $^3P^1$ and $^3P^0$, at 1.214 and 1.008 v. above the $^3P^2$ ground state respectively (10).

Therefore the initial part of the curve should be due to the process involving the ground state only. It apparently does not obey a linear law, nor a Wannier function. Arbitrarily, a square root plot, as shown in the figure, gives a straight line with a slight break at 1.0 ± 0.2 v. above threshold, which point seems to correspond with the onset of the $^3P^0$ state. Therefore, taking this initial part of the square root plot as representing the ground state process, and comparing it with Xe^+ as a standard, we obtain for the second ionization potential of xenon, the value 21.09 ± 0.05 ev. The spectroscopic value is 21.204 ev. (7)

and so we may consider the interpretation as possible. Similar approximately square-law curves were also found for argon.

These results are in contradiction with the findings of Hickam *et al.* (8) who have found a correlation with a linear threshold law using the Fox method. Following their interpretation, it is also possible that the curve of Fig. 9 is due to a linear probability function, plus a large contribution from resonant autoionization mechanisms excited by the larger electron energy band used.

The results on Ze^{++} and N_2^+ indicate that it is unwise to make a priori assumptions of the nature of the probability function; and also that it is necessary to use more than one width of electron energy spread to obtain maximum information.

ACKNOWLEDGMENTS

The author wishes to thank Dr. L. Kerwin for his great assistance and encouragement, and also the other members of the Faculty of Science for their many helpful discussions. Thanks are also due to Dr. C. A. McDowell of the University of Liverpool for an advance copy of his paper; to St. Francis Xavier University for a leave of absence and financial assistance; to the National Research Council for a grant for material; and to Mr. C. E. Jordan for his assistance in the preparation of this paper.

REFERENCES

1. ALLEN, J. S. Rev. Sci. Instr. 18: 739. 1947.
2. DALBY, F. W. and DOUGLAS, A. E. Phys. Rev. 84: 843. 1951.
3. DOUGLAS, A. E. Can. J. Phys. 30: 302. 1952.
4. FOX, R. E., HICKMAN, W. M., and KJELDASS, T., JR. Phys. Rev. 89: 555. 1953.
5. HAGSTRUM, H. D. Revs. Mod. Phys. 23: 185. 1951.
6. HANSON, E. E. Phys. Rev. 51: 86. 1937.
7. HERZBERG, G. Atomic spectra and atomic structure. 2nd ed. Dover Publications, Inc., New York. 1944.
8. HICKAM, W. M., FOX, R. E., and KJELDASS, T., JR. Phys. Rev. 90: 386A. 1953.
9. HUGHES, A. L. and MCMILLAN, J. H. Phys. Rev. 34: 291. 1929.
10. HUMPHREY, J. C. J. Research Natl. Bur. Standards, 22: 19. 1939.
11. KERWIN, J. L. Rev. Sci. Instr. 21: 96. 1950.
12. MARINIER, T. and BLEAKNEY, W. Phys. Rev. 72: 807. 1947.
13. MEINEL, A. B. Astrophys. J. 114: 431. 1951.
14. MORRISON, J. D. J. Chem. Phys. 21: 1767. 1953.
15. OSBORNE, F. J. F. M.Sc. Thesis, Université Laval, Québec, P.Q. 1951.
16. OVERHOFF, M. W. M.Sc. Thesis, Université Laval, Québec, P.Q. 1952.
17. SMYTH, H. D. Revs. Mod. Phys. 3: 347. 1931.
18. WANNIER, G. H. Phys. Rev. 90: 817. 1953.
19. WARREN, J. Nature, 165: 810. 1950.
20. WATANABE, K., MARMO, F. F., and INN, E. C. Y. Phys. Rev. 91: 1155. 1953.

CALCULATED DIFFRACTION PATTERNS OF DIELECTRIC RODS AT CENTIMETRIC WAVELENGTHS[1]

By Charlotte Froese and James R. Wait

ABSTRACT

Diffraction patterns are calculated for a cylindrical electromagnetic wave incident normally on a dielectric cylinder of infinite length whose diameter is comparable to the wavelength. Reasonably good agreement is obtained when the results are compared with published experimental results.

INTRODUCTION

Several experimental investigations of diffraction of electromagnetic waves by cylindrical rods whose diameter is comparable to a wavelength have been reported recently (1, 2, 7). It was observed that the effects of diffraction around the cylinder are very pronounced. In particular, the fields just behind a dielectric cylinder exhibit extreme maxima and minima which are difficult to explain by any simple physical argument. It is possible that some of the effects observed by the above-mentioned investigators might be explained very crudely by geometrical optics. In general, however, since the diameter of the cylinder is of the order of a wavelength, a complete quantitative description can only be found from a solution of the boundary value problem.

The above-mentioned investigators did carry out calculations based on the solution of the boundary value problem for the scalar wave diffraction of a perfectly conducting cylinder of infinite length. They found very good agreement with observed diffraction patterns of brass rods. To the authors' knowledge no calculations for dielectric cylindrical rods have been published. It is the purpose of this note to present such computations and to select the parameters to correspond to the experimental conditions. The reader is referred to the original papers for details of the observational technique.

OUTLINE OF THEORY

The geometry of the diffraction problem is shown in Fig. 1. The source of the radiation is taken to be S, the geometrical apex of the horn. SX is the

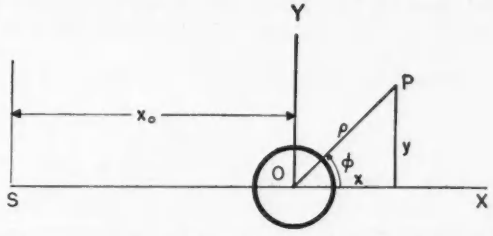

Fig. 1. Schematic representation of the dielectric cylinder of radius a with respect to the (x, y, z) and (ρ, ϕ, z) coordinate systems.

[1]*Manuscript received August 27, 1954.*
Contribution from the Radio Physics Laboratory of the Defence Research Board, Ottawa, Ontario.

geometrical axis of symmetry of the horn. The diffracting cylinder of radius a is located at O and is coaxial with the z axis of a cartesian coordinate system. There are two important cases to investigate, namely when the polarization of the incident electric vector is parallel and when it is perpendicular to the axis of the cylinder. The parallel case is considered first.

The distance x_0 is much greater than x and y in the experiments so that the incident wave at O is almost plane, with a slight curvature in the wave front. As shown by Kodis (2) a good approximation for the plane $z = 0$ is to assume that the incident wave is cylindrical, which is equivalent to representing the excitation by a line source of electric current at S. The exact solution for this problem has been given previously by Wait (5) for a homogeneous cylinder of arbitrary dielectric constant ϵ_1 and permeability μ_1 embedded in a homogeneous medium (ϵ_0, μ_0). Employing Watson's (6) notation for Bessel functions the field E_z at P expressed as a ratio of the incident field E_0 at P is*

$$[1] \qquad \frac{E_z}{E_0} = e^{i\phi_0} + \sum_{m=0}^{\infty} C_m i^m H_m^{(1)}(k\rho) A_m \cos m\phi$$

where

$$\phi_0 \simeq k\left[\sqrt{(x+x_0)^2+y^2} - (x+x_0)\right],$$

$$k = 2\pi/\lambda, \qquad \lambda = \text{free space wavelength},$$
$$C_0 = 1, \qquad C_m = 2 (m \neq 0),$$
$$\rho = (x^2+y^2)^{\frac{1}{2}}, \qquad \phi = \tan^{-1}(y/x),$$

and

$$A_m = -\frac{nJ_m(ka)J_m'(Nka) - J_m'(ka)J_m(Nka)}{nH_m^{(1)}(ka)J_m'(Nka) - H_m^{(1)\prime}(ka)J_m(Nka)}$$

where $n = (\mu_0\epsilon_1/\mu_1\epsilon_0)^{\frac{1}{2}}$, $N = (\epsilon_1/\epsilon_0)^{\frac{1}{2}}(\mu_1/\mu_0)^{\frac{1}{2}}$.

In writing equation [1] in this form, it has been assumed that

$$\frac{H_0^{(1)}\left[k\sqrt{(x+x_0)^2+y^2}\right]}{H_0^{(1)}[k(x+x_0)]} \simeq e^{i\phi_0} \text{ and } \frac{H_0^{(1)}[kx_0]}{H_m^{(1)}[kx_0]} \simeq i^m,$$

which are justified since $kx_0 \gg 1$ and x and $y \ll x_0$. For purposes of computation it is convenient to rewrite equation [1] in the following form

$$[2] \qquad \frac{E_z}{E_0} = e^{i\phi_0} - \sum_{m=0}^{\infty} C_m i^{m+1} e^{-i\eta_m} \sin \eta_m H_m^{(1)}(k\rho) \cos m\phi,$$

where

$$\tan \eta_m = \tan \delta_m(ka) \frac{\tan \alpha_m(ka) - \tan \alpha_m(Nka)}{\tan \beta_m(ka) - \tan \alpha_m(Nka)},$$

with $\mu_1 = \mu_0$

and

$$\tan \delta_m(x) = -J_m(x)/Y_m(x),$$
$$\tan \alpha_m(x) = -xJ_m'(x)/J_m(x),$$
$$\tan \beta_m(x) = -xY_m'(x)/Y_m(x).$$

A time factor $\exp(-i\omega t)$ is employed.

When $N \rightarrow i^{\frac{1}{2}}\infty$, corresponding to a perfectly conducting cylinder, it can be seen that $\eta_m \rightarrow \delta_m(ka)$.

When the incident electric vector is perpendicular to the axis of the cylinder, as in the experimental work of Keys (1), the ratio of the magnetic field H_z at P to the incident field H_0 at P is identical in form to equation [1] with the exception that the coefficient n is replaced by n^{-1} where it occurs in A_m. It is convenient to express the field in the following form for purposes of computation:

$$[3] \qquad \frac{H_z}{H_0} = e^{i\phi_0} - \sum_{m=0}^{\infty} C_m i^{m+1} e^{-i\eta_m^*} \sin \eta_m^* H_m^{(1)}(k\rho) \cos m\phi,$$

where

$$\tan \eta_m^* = \tan \delta_m(ka) \frac{N^2 \tan \alpha_m(ka) - \tan \alpha_m(Nka)}{N^2 \tan \beta_m(ka) - \tan \alpha_m(Nka)}$$

with $\mu_1 = \mu_0$. When $N \rightarrow i^{\frac{1}{2}}\infty$ corresponding to the perfectly conducting cylinder, it follows that

$$\eta_m^* \rightarrow \delta_m'(ka)$$

where

$$\tan \delta'(x) = -J_m'(x)/Y_m'(x).$$

In the experimental work of Keys (1), the E_y component of the field is measured, which is related to H_z by

$$E_y = \frac{1}{i\epsilon_0 \omega} \frac{\partial H_z}{\partial x}.$$

This component of the electric field, expressed as a ratio of the incident field, is then written in suitable form for computation as follows:

$$[4] \qquad \frac{E_y}{E_0} = e^{i\phi_0} - \sum_{m=0}^{\infty} C_m i^m e^{-i\eta_m^*} \sin \eta_m^* F_m,$$

where

$$F_m = \cos m\phi \cos \phi H_m^{(1)\prime}(k\rho) + \frac{m \sin m\phi \sin \phi H_m^{(1)}(k\rho)}{k\rho}.$$

The functions $\alpha_m(x)$, $\beta_m(x)$, $\delta_m(x)$, and $\delta_m'(x)$ are tabulated extensively by Lowan *et al.* (3). These tables, which are not readily available, greatly simplify the computations.

PRESENTATION OF RESULTS

Computations from equation [1] have been carried out for selected values of the parameters. In Fig. 2 the calculated amplitude and phase of E_z/E_0 are plotted against ky for a polystyrene cylindrical rod for $x_0 = 600$ cm., $\lambda = 1.25$ cm., $a = 1.27$ cm., and with the relative dielectric constant N^2 taken to be 2.56 to correspond with the experimental conditions of Kodis (2). The experimental curves are shown by the broken curves which correspond quite closely with the calculated values except for small values of ky. The discrepancy here,

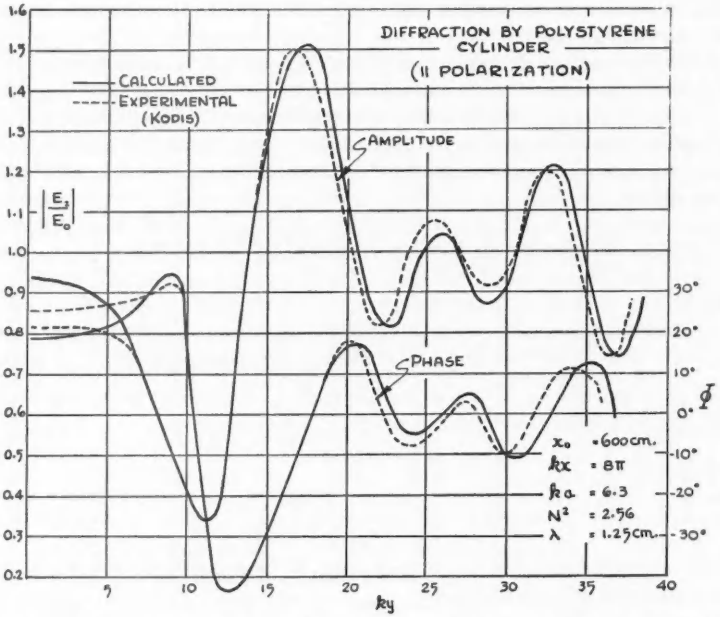

FIG. 2. The amplitude and phase of E_s/E_0 for a polystyrene cylinder whose radius is approximately equal to a wavelength.

which is not more than 13%, can probably be attributed to the ohmic loss in the polystyrene which has been neglected in the calculation. Actually, the dielectric constant N^2 according to published values (4) would be $2.56(1 + i0.0012)$ at a wavelength of 1.25 cm. It is also possible that the interaction between the probe and the cylinder might account for this disagreement.

Similar computations from equation [1] have also been carried out for a lucite rod ($N^2 = 2.56$, $a = 1.22$ cm.) and a tenite rod ($N^2 = 3.20$, $a = 1.27$ cm.), both for $x+x_0 = 615$ cm. and $\lambda = 3.2$ cm. These results are plotted in Figs. 3 and 4. Experimental values of McLay are shown in Fig. 3 by the broken curves which correspond very closely to the computed curves. It is also interesting to compare the computed patterns for the lossless tenite cylinder in Fig. 4 with Wiles' and McLay's (7) published experimental results for a hard rubber cylinder. All conditions for the two cases are nearly identical except that the rubber has a loss tangent of about 0.10, which has the effect of greatly reducing the maxima of intensity just behind the cylinder. The other aspects of the curve, however, are very similar, which would substantiate our explanation that the focusing action of the cylinder is seriously affected by the resistive loss in the dielectric.†

†*Prof. McLay has recently repeated the experiment with a tenite cylinder and the results are within a few per cent of the calculated values shown in Fig. 4.*

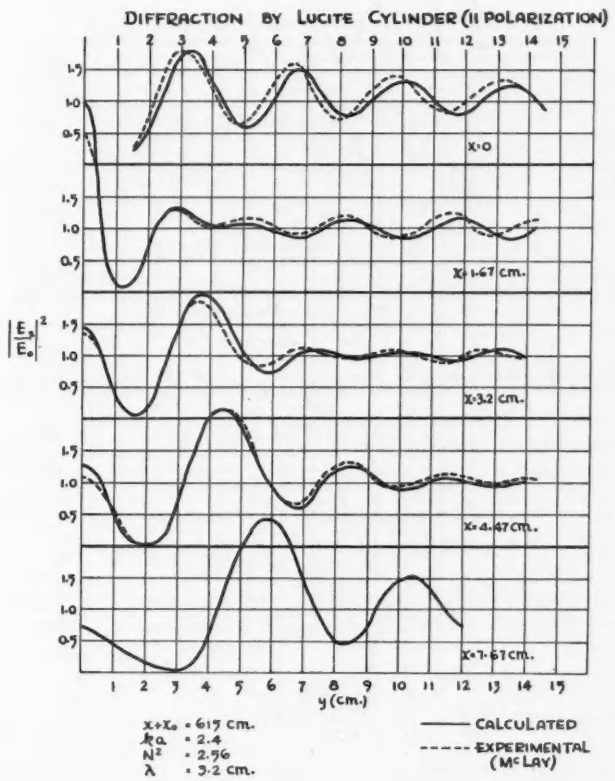

FIG. 3. The amplitude of $(E_z/E_0)^2$ for a lucite cylinder whose diameter is comparable to a wavelength.

The complexity of the calculations for the perpendicular polarization is somewhat greater. The computations from equation [4] for $x+x_0 = 535$ cm., $\lambda = 3.2$ cm., $a = 1.22$ cm., $N^2 = 2.56$, are illustrated in Fig. 5 for several values of x. Experimental values of Keys (1) are shown by the broken curves. The agreement is reasonably good except for points in the plane $x = 0$. It is believed that the discrepancy here can be partly attributed to the spurious response of the detector probe to the E_x component of the field. In the plane $x = 0$, the E_z component of the scattered field from the cylinder is much larger than the E_y component so that slight misalignments or asymmetry of the probe will produce a response which is not indicative of E_y.

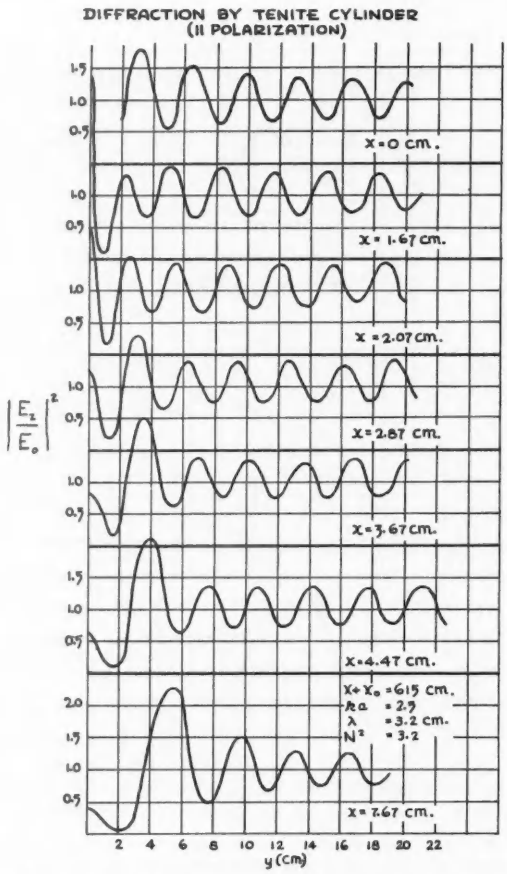

FIG. 4. The amplitude of $(E_z/E_0)^2$ for a tenite cylinder whose diameter is comparable to a wavelength.

CONCLUSION

These results show that a predominant characteristic of the diffraction pattern of a dielectric rod is the peaks of intensity near the center of the geometrical shadow just behind the cylinder. This effect is apparently present when the incident wave is either parallel or perpendicular to the axis of the cylinder. These peaks seem to be generally slightly lower in the experimental patterns, which is probably a result of resistive loss in the dielectric. For the case of lucite and polystyrene the dielectric "loss tangent" is never greater than about 0.005 at centimeter wavelengths and the assumption that the dielectric constant is real would not be expected to lead to serious error.

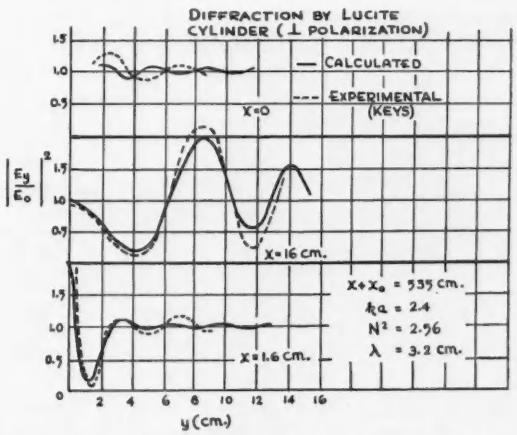

FIG. 5. The amplitude of $(E_y/E_0)^2$ for a lucite cylinder with the polarization of the incident electric vector transverse to the axis of the cylinder.

In all the diffraction patterns it is noted that intensity maxima and minima vary in a very regular manner in the region away from the geometrical shadow. Furthermore, the location of these maxima and minima is only slightly dependent on the dielectric constant of the cylinder.

ACKNOWLEDGMENT

Appreciation is expressed to Prof. A. B. McLay who communicated to us the experimental results shown in Fig. 3. Helpful suggestions have been given by J. H. Crysdale and J. E. Keys.

REFERENCES

1. KEYS, J. E. M.Sc. Thesis, Dept. of Physics, McMaster University, Hamilton, Ont. 1953. To be published.
2. KODIS, R. D. J. Appl. Phys. 23: 249. 1952.
3. LOWAN, A. N., MORSE, P. M., FESHBACH, H., and LAX, M. Appl. Math. Panel Rept. No. 62.1 R. Mass. Inst. Technol. Feb. 1945.
4. Tables of dielectric materials. Vols. I–III. Laboratory for Insulation Research of the Massachusetts Institute of Technology, Cambridge, Mass. June 1948.
5. WAIT, J. R. Geophysics, 17: 378. 1952.
6. WATSON, G. N. Theory of Bessel functions. 2nd ed. Cambridge University Press, London. 1944.
7. WILES, S. T. and MCLAY, A. B. Can. J. Phys. 32: 372. 1954.

THE EFFECT OF HIGH LOADING ON THE KINETIC FRICTION OF ICE[1]

By C. D. Niven

ABSTRACT

The kinetic friction of stainless steel on ice decreased very markedly at high loadings of 30 to 50 kgm. per sq. cm. This constituted a violation of Amontons' Law. At low loading the material of a slider is of far greater importance than at high loading, which suggests that in the explanation of the friction of ice at least two important factors are involved, which are related respectively to (*a*) pressure and (*b*) adhesion.

INTRODUCTION

Although the low friction of ice just under the freezing point must have been observed by man from the earliest times, yet the explanation of the phenomenon has been only partially given. Physicists and engineers have been for years content with the theory that pressure tended to melt the ice and so created a film of water to furnish lubrication. More recently the suggestion has been put forward that the liquid for lubrication is provided by frictional heat (3) but this at once raises the question as to why certain good metallic conductors of heat have a low friction on ice.

The explanation of this extremely commonplace phenomenon is certainly not obvious and needs to be completely reconsidered in the light of modern developments in the theory of friction (1, 5, 6). The lack of information at high loading is surprising. Interest seems to have centered mainly around the ski for personnel or aircraft rather than around the sleigh runner. A report, however, by Wakefield (8) on logging sleighs sliding on packed snow, published in 1938, indicated that the friction at high loading decreased. In 1939 Bowden and Hughes (3) using a turntable showed that the friction of ice dropped when the load on the slider was increased above *ca.* 300 gm. Only loads under 600 gm. were used and the area of apparent contact was not stated. The data, nonetheless, supported Wakefield's work and to some extent fitted in with the field observation that after a certain load had been put on a runner drag increased little as the load was further increased.

Altogether there was a distinct suggestion that insofar as the kinetic friction of ice was concerned Amontons' Law was not always true at high loading. The work described below deals with the investigation of this point.

APPARATUS

A photograph of the turntable which was used by the writer is shown in Fig. 1. It consisted of a 36 in. diameter disk of 3/16 in. boiler plate on the edge of which was fixed a circular bath for containing the water to be frozen for the track. The boiler plate and the track were mounted at the center on a vertical spindle protruding from a gear box. A d-c. motor, with series resistance, was used to drive the turntable.

[1]*Manuscript received August 31, 1954.*
Contribution from the Division of Physics, National Research Council, Ottawa, Canada. Issued as N.R.C. No. 3437.

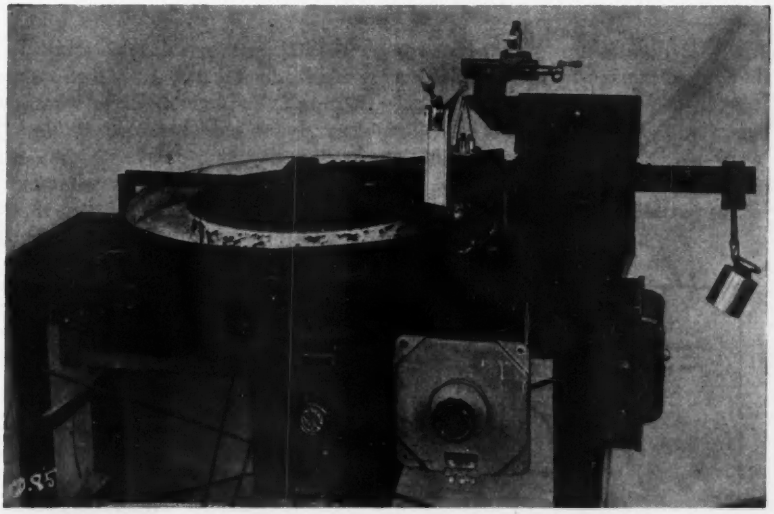

FIG. 1. Photograph of turntable, showing tool-holder for machining surface of ice, lever arm for putting load on slider, and gravity balance for measuring the drag. Since the circular trough was empty at the time of photographing, the arm is not resting on the slider; the latter can be seen in the trough near the arm.

From a point above the center an arm or lever was pivoted so that it could be raised above the track when the ice was being machined, and lowered on to the sample or slider during a test. The pivot was somewhat like a universal joint because provision was made to allow the arm to swing horizontally through a small angle. To reduce friction against motion in this plane ball bearings were used. The sample supported the arm at a point 15 in. from the center or pivot and a hook was provided 25 in. farther out on the arm for carrying weights. A 60 lb. weight could by this means put a load of 193 lb. on the slider; on a sample of area 2 in. × 1 in. this approximated 100 lb./sq. in. To support the table under the sample a wheel had to be mounted under the boiler plate.

The track was 6 in. wide and 3 in. deep and after the ice was frozen it had to be machined. To do this a tool holder was mounted on the bench of the turntable in such a way that it could be swung into place while the ice was being surfaced, and swung out of place when the experiments were in progress. Fig. 1 shows the tool holder swung out of place and the arm down.

The balance was a simple gravity balance (see Fig. 2). The sensitivity far exceeded the sensitivity required to measure the "stick-slip" drag of the friction test. The speed of rotation of the turntable was kept down to about one revolution in three seconds; as the diameter of the circular track was 33.5 in. this worked out to about 89 cm. per sec. Since 1 mile per hour is approximately 45 cm. per sec. the speed was considerably lower than the speed which would normally occur in transportation; therefore the drag values

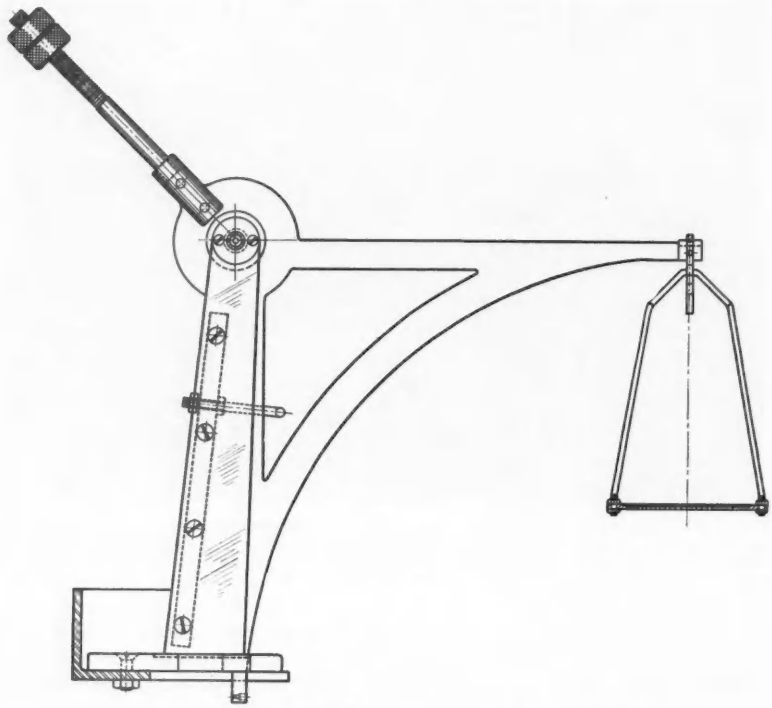

FIG. 2. Gravity balance designed to weigh a horizontal drag.

can be considered higher than would be encountered in practice on similar ice surfaces and in the same atmospheric conditions. On account of the fact that the slider was running over the same track again and again, speeds were kept low intentionally, in order to prevent too much heat from being put into the surface of the ice; obviously the work done by the motor on the slider must for the most part go into the ice as heat. A $\frac{1}{2}$-in. steel ball resting in a block of brass permitted the slider to adjust to any angle in any direction under the lever carrying the weights.

The cold room in which the tests were made could be controlled to $\pm 1°F$.

Twenty pounds were as a rule added at a time to the hook at the end of the lever and with each addition the drag was balanced with weights on the balance pan. Since the actual load on the slider was the thrust of the arm itself plus $2\frac{2}{3}$ times the weight on the hook, 0, 20, 40, and 60 lb. on the hook corresponded to loads on the slider of 14.92, 39.13, 63.35, and 87.56 kgm. These figures are the abscissae of points on the drag vs. load charts. Values of the friction constant have not been worked out because the significance of a constant rather disappears if it is not a constant at all.

RESULTS

Results on stainless steel, bakelite, and teflon (polytetrafluoroethylene) are shown in Figs. 3, 4, 5. These graphs represent drag plotted against load (i) on a sample of apparent area 13 sq. cm.—indicated by full lines—and (ii) on a sample of apparent area 1.6 sq. cm.—indicated by broken lines. The larger apparent area corresponds to the area of a piece of material 2 in. × 1 in. while the smaller apparent area corresponds to the area of two runners on a miniature sleigh each 1 in. long and $\frac{1}{8}$ in. wide. All drag vs. load graphs are plotted to the same scale so that direct comparisons can be made.

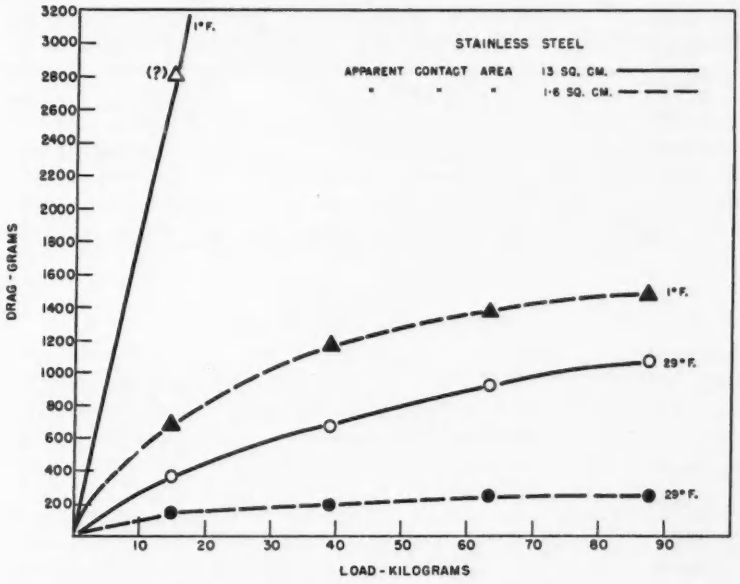

FIG. 3. Drag vs. load curves for stainless steel.

The measurements were made at 29°F. and 1°F. The samples all slid on the ice fairly smoothly except the larger sample of stainless steel at 1°F. In this instance the stick-slip motion, so well known in the measurement of friction, became very troublesome and the drag value was most indefinite. A question mark against the point on the diagram draws attention to this. Only the lowest loading was measured because the jerky motion was so hard on the apparatus.

The graphs are not plotted from averages. Each curve is plotted from a single set of readings which is representative of the behavior of the material at that temperature. Friction measurements are notoriously difficult to repeat to a high degree of accuracy, and with ice slight changes in temperature can cause a change in the absolute friction value. It was found however on examining the

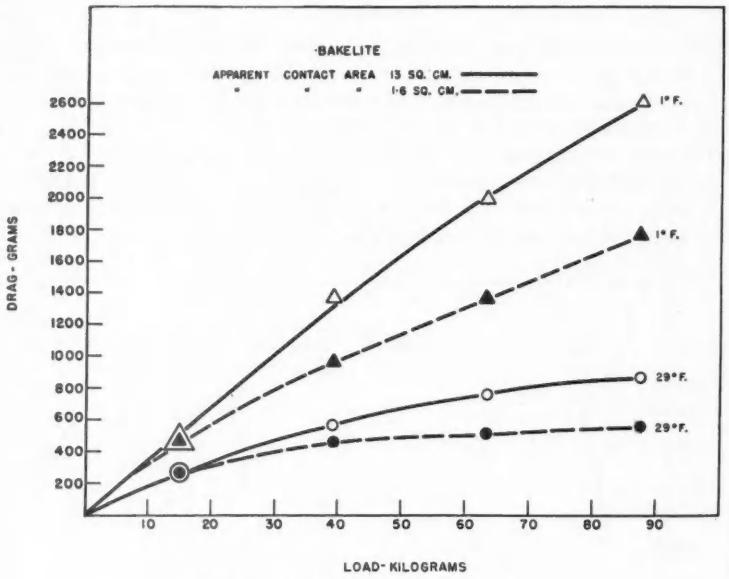

FIG. 4. Drag vs. load curves for bakelite.

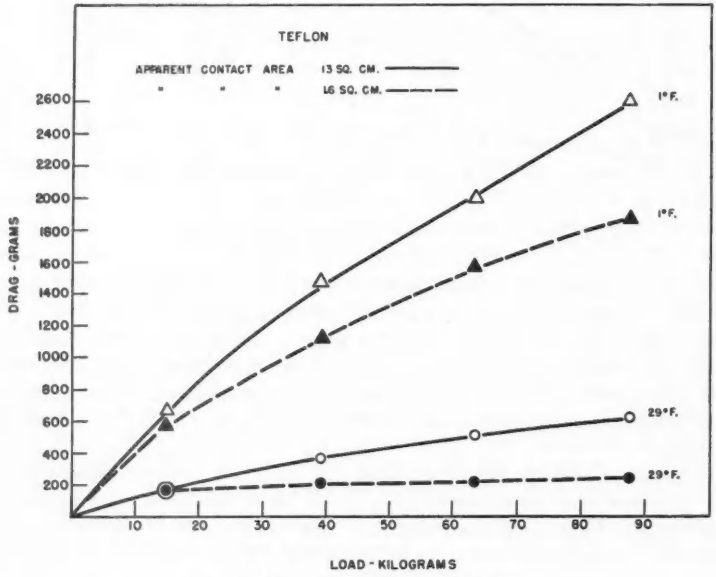

FIG. 5. Drag vs. load curves for teflon.

experimental data that these slight variations were quite unimportant in drawing several conclusions. These can be summed up as follows:

(1) All sets of readings showed very marked curving of the graphs for samples of small apparent area of contact at 1°F. but little or no curving for the samples of larger apparent area of contact at that temperature.

(2) All sets of readings for teflon and stainless steel samples of small apparent area of contact showed an almost constant drag at 29°F.

(3) The readings consistently showed that the bakelite samples whether of small or of large apparent area of contact had a higher drag value at 29°F. than the corresponding teflon samples. At 1°F. the accuracy of the work does not however permit discrimination between these two materials.

(4) At both 29°F. and 1°F. the effect of apparent area of contact on the kinetic friction is far more marked for stainless steel than for either bakelite or teflon.

(5) Considering only samples of large apparent area of contact, the increase of kinetic friction with lowering of temperature is far greater for stainless steel than for either bakelite or teflon; on the other hand, considering only the samples of small apparent area of contact, while there is an increase in kinetic friction with lowering of temperature all three materials are comparable at 1°F. with a distinct indication that at very high loadings stainless steel may slide the best of the three materials.

DISCUSSION OF RESULTS

It is evident that under certain circumstances depending upon temperature and loading, the field observation that drag for steel is not increased much with increase of load at high loadings is essentially correct. In other words Amontons' Law fails at high loading on ice under certain circumstances. Such a conclusion for kinetic friction contrasts with Bowden's (2) conclusion on static friction. Teflon, which has come on the market only recently, does not show much improvement over bakelite around 0°F., but it is definitely better than bakelite just below freezing; bakelite has been advocated by Klein (7) for aeroplane shoeing before teflon was discovered, but teflon seems to have a possible advantage worth investigating under more realistic conditions than the laboratory permits.

The curving towards the load axis at high loading, which is most clearly shown in the case of stainless steel around 0°F., taken in conjunction with the fact that stainless steel contrasts severely with the two plastics in certain other aspects of the work, suggests the following micromechanism for the low friction of ice. After the molecules which constitute the extreme tip of some asperity on the ice surface have been forced to start moving by the pressure and sheering forces during the sliding process, they have become "agitated" or in other words "heated"; they have received a part of the energy which the motor has wasted in dragging something along the level. Were this energy wastage great enough one would expect melting, and using a rubber slider and a temperature just below freezing this melting of the ice surface is quite easy to observe; on the other hand using a hard slider and a lower temperature, it is

not easy to detect actual liquid. However it is not really of importance whether liquid can be detected either visually or by means of a chemical indicator. The important thing is that the molecules on the tips of the asperities have become agitated both on the ice surface and on the slider surface; and when molecules are agitated they are conditioned—so to speak—for forming a bond if bonding is at all feasible. No one would argue this point if one were discussing heating reagents in a test tube over a bunsen burner or welding platinum wire, but it is not so obvious when the agitation has arisen mechanically through dragging one substance over another. With ordinary solid materials such as constantan sliding on mild steel, temperatures as high as 1000°C. have been observed by Bowden and Ridler (4) during the friction process. The tendency to form liquid when one substance slides over the other must then normally assist the formation of an adhesive bond rather than assist in the sliding.

Ice however is not a normal substance and there is, in consequence, a special point to consider. If a peak on the ice surface is approaching an inverted peak on the slider surface, when they actually make contact there is a sudden increase in pressure. How great this is will depend on the load and on the velocity of approach. Ice has the peculiar property of tending to melt rather than freeze with increase of pressure, so that agitated molecules which are available for bonding are discouraged from getting into the solid state during the collision of two peaks although this is just the very time that any normal substance would find it most easy to take advantage of the possibility of forming a bond.

If the temperature is very cold this tendency to melt rather than freeze when two peaks collide is too small to consider in comparison with the tendency of the surrounding cold to stop agitation and so form a bond. Thus the friction of very cold ice would be expected to differ little from that of any other solid. Those materials which are hydrophobic would not bond easily with ice even when the molecules were agitated, so that there would be no special reason why increase of pressure at peaks at the time of collision should help prevent something that can only occur with difficulty anyhow.

Weyl (9) considers ice to be covered with a fluid surface layer hundreds of molecules thick. The idea of this thick layer of distorted water molecules would fit in much better with the observed friction facts at high loading if this layer were not a fluid but a solid which like ordinary ice contracted on turning to a liquid. Any theory which fails to make use of this basic and almost unique property of ice in explaining its low friction seems questionable.

CONCLUSIONS

1. Amontons' Law is not as a rule true for substances sliding on ice when the loading per unit area of apparent contact is high.

2. There appear to be two entirely different factors at work in determining the friction of a substance on ice, firstly a general friction factor which depends on the loading and on the temperature and which applies to all hard materials sliding on ice, and secondly a special friction factor which depends on particular qualities of the sliding material. How these two factors combine to give

the resulting friction is not clear but they are certainly not additive. The work suggests that the second factor is relatively less important than the first at very high loadings per unit area.

ACKNOWLEDGMENTS

The author would like to express his thanks to the Director of the Division of Mechanical Engineering, N.R.C., for the hospitality of the Low Temperature Laboratory needed for this work; to Mr. J. D. C. Waller of that laboratory for much help in connection with the cold room conditions; and to Dr. Thomas H. McConica of the American Ski Company for valuable general information on the friction of ice.

REFERENCES

1. BOWDEN, F. P. Discussion meeting. Proc. Roy. Soc. (London), A, 212: 440. 1952.
2. BOWDEN, F. P. Proc. Roy. Soc. (London), A, 217: 462. 1953.
3. BOWDEN, F. P. and HUGHES, T. P. Proc. Roy. Soc. (London), A, 172: 281. 1939.
4. BOWDEN, F. P. and RIDLER, K. E. Proc. Roy. Soc. (London), A, 154: 640. 1936.
5. BOWDEN, F. P. and TABOR, D. Proc. Roy. Soc. (London), A, 169: 391. 1939.
6. FINCH, G. I. 34th Guthrie lecture. Proc. Phys. Soc.(London), B, 63: 465. 1950.
7. KLEIN, G. J. Natl. Research Council Can. Rept. MM-225. 1950.
8. WAKEFIELD, W. E. Rept. on Project No. 107, Forest Products Labs., Dominion Govt., Ottawa. 1938.
9. WEYL, W. A. J. Colloid Sci. 6: 389. 1951.

MOTION OF CLOUDS OF ABNORMAL IONIZATION IN THE AURORAL AND POLAR REGIONS[1]

By E. L. Hagg and G. H. Hanson[2]

ABSTRACT

Examination of records taken in rapid succession at ionospheric stations in Northern Canada has revealed three distinctive types of echoes corresponding to clouds of ionization in motion. One type is ascribed to clouds of sporadic *E* moving horizontally over the station. The second type is believed to be due to clouds of ionization descending vertically from the *F* region to the *E* region, while the third type appears to be from clouds moving at extremely high velocities in the *E* region. Reflections of the second and third types have been seen only at stations in or north of the auroral zone. The characteristics of the echoes, the velocities of the clouds, and other associated phenomena are discussed.

1. INTRODUCTION

Canadian ionospheric stations are provided with automatic recording equipment which can obtain complete *h'-f* records of the ionosphere as often as 10 times per minute. For several years such records have been taken for 24 hr. every two weeks at Baker Lake (64.3°N., 96.0°W.) and at Fort Chimo (58.1°N., 68.3°W.). A smaller number are available from Resolute Bay (74.7°N., 94.9°W.). Unfortunately, the interference created by the operation of the equipment has prevented the taking of continuous runs at the other northern station at Churchill (58.8°N., 94.2°W.) and has curtailed the program at Resolute Bay. The *h'-f* sweeps are photographed on 16 mm. film in such a way that when the film is run through a motion-picture projector, a speeded-up picture of the changes in the ionosphere is revealed. Many short-lived reflections and rapid changes are observed which would be missed completely by the routine sweeps which are taken at 15-min. intervals.

Most of the film from these continuous runs has been carefully examined recently in order to study certain unusual types of echoes which had been observed earlier. These echoes have been divided into three distinct types. The characteristics of each are given in succeeding sections.

2. VELOCITIES OF CLOUDS OF SPORADIC *E*

When viewing continuous runs, traces identical in appearance with sporadic *E* often appear at virtual heights of 200 to 300 km. and then decrease in height in a regular manner until they reach the 100 km. level. The traces often remain at this level for some time and then increase in height again until they disappear. They will be referred to as type I traces. A typical graph of height as a function of time is shown in Fig. 1. It is evident that type I traces can be interpreted as being due to reflections from a cloud of sporadic *E* moving horizontally at a height of about 100 km., the minimum

[1]*Manuscript received June 16, 1954.*

Contribution from the Defence Research Telecommunications Establishment (Radio Physics Laboratory), Defence Research Board, Ottawa, Canada. Work carried out under DRB Project No. D48-97-52-01.

[2]*Present Address: Department of Electrical Engineering, University of Minnesota, Minneapolis 14, Minn.*

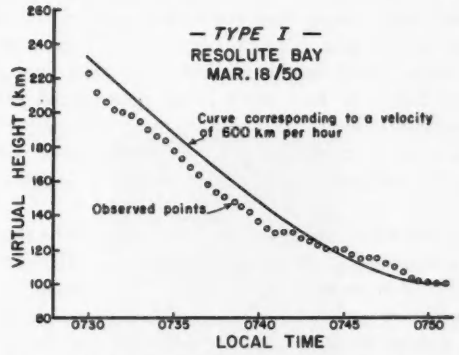

FIG. 1. The change in virtual height of a sporadic E cloud as it approaches the station.

virtual height occurring when the cloud is either directly over the station or is at a point of closest approach. This phenomenon has been reported previously by Meek (3), who found 40 examples in film from Baker Lake. Of his 40 examples, 11 were of clouds which appeared to belong to the E region, while the others were believed to be higher.

A total of 51 more occurrences of type I clouds have been observed in this study. Of this number, 26 are from Resolute Bay, 15 are from Fort Chimo, and 10 are from Baker Lake. Graphs of height vs. time have been drawn for each occurrence and the velocities of each have been computed. In calculating the velocities it was assumed that the cloud was moving horizontally at constant speed at a height equal to the lowest height observed, or, if the minimum height observed was above 120 km., that the true height was 120 km., but that the cloud passed some distance to the side of the station. The distribution of velocities for each station is shown in Fig. 2. The median velocity is about 800 km. per hour with a few being three times as great. There are no significant differences in the velocities measured at the three stations.

The number of occurrences as a function of time of day is shown in Fig. 3. There is no favored time of day at Resolute Bay, but at Baker Lake and Fort

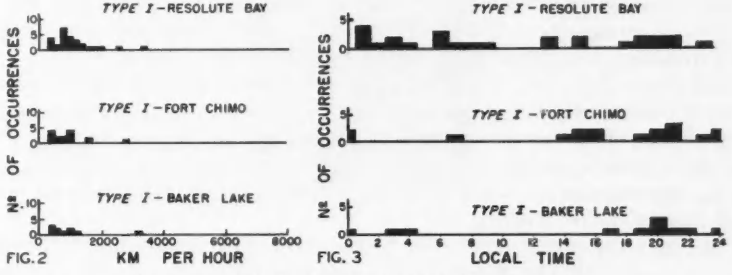

FIG. 2. The distribution of velocities of type I clouds.
FIG. 3. Diurnal distribution of type I clouds.

Chimo most type I clouds were observed in the evening. This is in agreement with observations of sporadic E made regularly at these stations. At Baker Lake and Fort Chimo, both in the auroral zone, most sporadic E occurs at night, whereas at Resolute Bay there is no pronounced diurnal variation. There were not enough observations to determine whether or not there was a diurnal variation of velocity. However, a greater range of velocities occurred between midnight and 8 a.m. and all the very high velocities occurred in the early morning.

The velocity of motion of the sporadic E cloud should be that of the air at the same height. It is interesting to compare the above results with measurements of ionospheric winds made by other methods. Chapman (1) has measured winds in the normal E region at Ottawa and Montreal, using the fading of radio echoes at spaced receivers. He found the velocities to range from 70 km. to 1080 km. per hour, with a median value of approximately 290 km. per hour. This is somewhat less than was found in this work where the velocities range from 270 to 3500 km. per hour and the median value is approximately 800 km. per hour. It is not too surprising to find these differences, however, for the observations were not made at the same location, nor were the reflections necessarily from the same height in the ionosphere.

3. VERTICAL MOTIONS FROM THE F REGION TO THE E REGION

Another type of moving cloud, hereafter referred to as type II, is illustrated by the series of photographs in Fig. 4. These photographs were taken 15 sec. apart and show the sudden appearance of a reflecting 'patch' below the $F2$ layer. The patch moves rapidly downward to a minimum virtual height of 180 km., and then rises to disappear in the $F2$ layer. A height vs. time plot of the cloud in Fig. 4 is shown in Fig. 5.

The characteristics of type II reflections are as follows. The trace first appears below the $F1$ or $F2$ trace and has the same curvature as the F traces. There is evidence of retardation at a critical frequency and of splitting into o and x branches. As the virtual height decreases, the highest frequency increases and the trace becomes flatter; when the height increases, the reverse changes take place. There are always some spread echoes and fuzziness in connection with the reflections, and occasionally the height fluctuates for a few moments at or near the minimum height. There is no blanketing of the F region and no significant effect on the regular F layers. The trace never appears at a frequency lower than the critical frequency of the E layer.

The above characteristics indicate that the cloud of ions causing the reflections is moving vertically from above the $F2$ layer into the E region. If such is the case, the cause of the phenomenon is hard to imagine. It is as if a stream of some ionizing radiation were suddenly turned on from outside the earth, the radiation becoming more intense and penetrating for some minutes and then gradually tapering off.

The velocities of each patch have been computed on the assumption that the motion is vertical. The distribution of velocities for the three stations where the phenomenon has been seen is shown in Fig. 6. The average downward

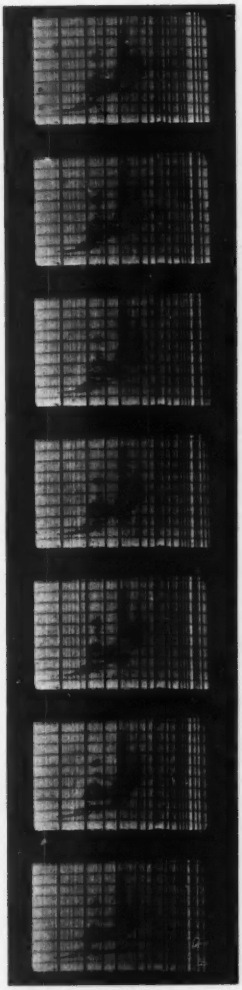

FIG. 4. A series of h'-f sweeps showing the movement of a type II cloud.

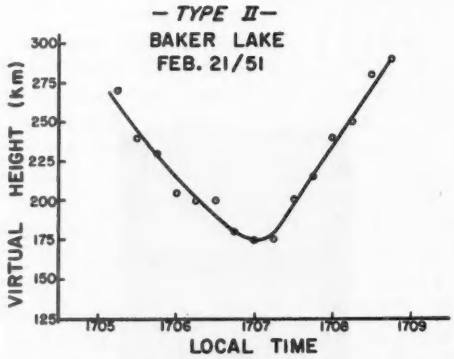

FIG. 5. The minimum virtual height of the cloud of Fig. 4 as a function of time.

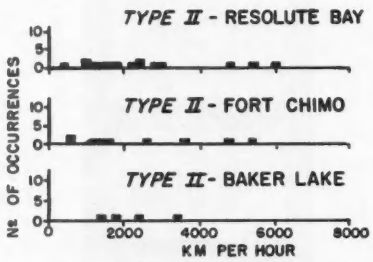

FIG. 6. The distribution of velocities of type II clouds.

velocity is about 7200 km. per hour although in one case a velocity three times as great was observed. There does not appear to be any difference among the stations although too few examples are available to be certain.

One significant point that has been noted is that the minimum height reached is lower at Fort Chimo and Baker Lake than at Resolute Bay. At the former stations it is usual for the minimum height to be 120 to 130 km. while at Resolute Bay it is about 150 km. When the ionization does reach to the E region, the critical frequency of the normal E layer increases slightly, or if the event occurs at night, a night E layer (2) forms. There have not been enough examples found as yet to determine whether type II is more common in the daytime or at night.

It must be emphasized that type II traces occur only at Fort Chimo, Baker Lake, and Resolute Bay. Many continuous runs are available from Prince Rupert and Winnipeg, far to the south, but no occurrence of type II has been seen there. With respect to the auroral zone, Prince Rupert, Winnipeg, and Resolute Bay are nearly equivalent, Resolute Bay being as far to the interior as the other stations are to the exterior.

It should be noted that the 28 occurrences which have been scaled do

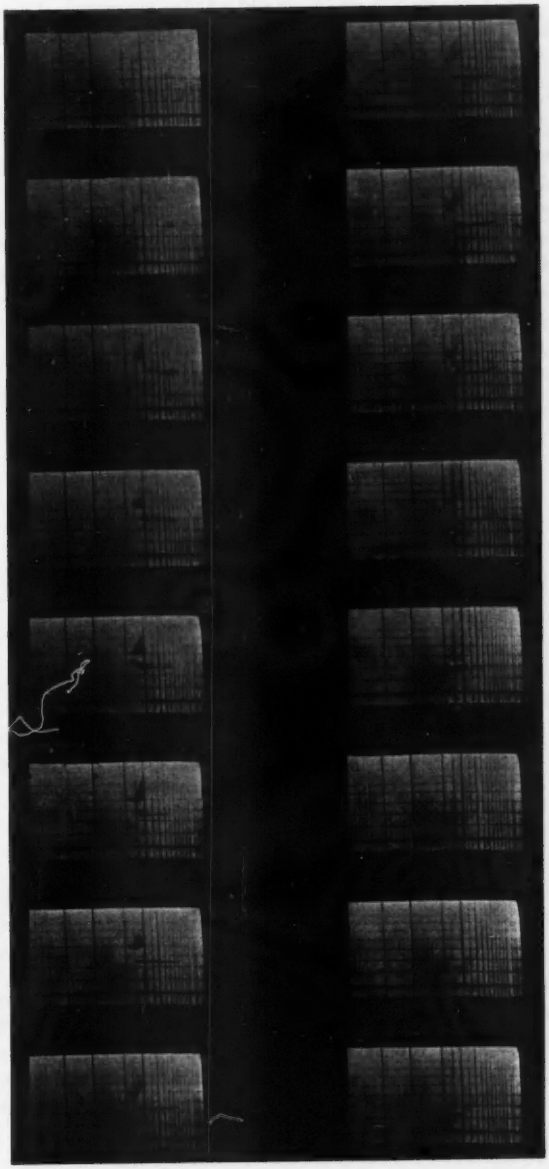

FIG. 7. A series of h'-f sweeps showing the motion of a type III cloud.

not give a true indication of the frequency of occurrence. On many other occasions, similar traces were seen but could not be accurately scaled because of spread echoes, lack of height markers on the film, or various equipment troubles.

4. EXTREMELY RAPID MOTION IN THE *E* REGION

A third type of abnormal ionospheric reflection has been observed at Fort Chimo and Baker Lake. Type III echoes are in many ways similar to type I echoes, except that the apparent velocity is much higher. As well, absorption is invariably much increased after the trace reaches the *E* region, and blackouts occur as an aftermath. The appearance of the reflections is shown in the series of photographs in Fig. 7, while the rate of change of virtual height can be seen from the graph in Fig. 8. The distribution of the velocities for Fort Chimo and Baker Lake is shown in Fig. 9.

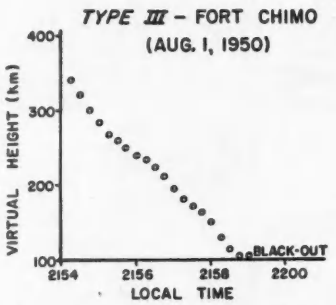

FIG. 8. The virtual height of the type III reflections of Fig. 5 as a function of time.

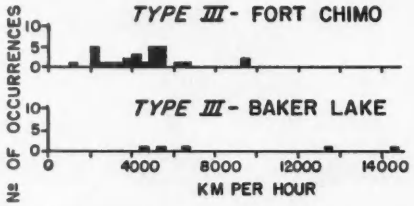

FIG. 9. The distribution of velocities of type III clouds.

The type III traces usually appear first at virtual heights of from 300 to 500 km. at a frequency of from 6 to 10 Mc. or more. As the height decreases the frequency range of the reflections decreases, although not regularly, until at a height of 100 km. the trace usually extends 2 or 3 Mc. beyond the f_0E, that is to about 6 Mc. In some cases the trace has descended to a height of 85 km.

From the appearance of the reflections and from the fact that no retardation has been seen near the *F*2 layer critical frequencies, it would seem that the

ion cloud is moving horizontally in the E region. On this assumption, the velocities have been computed. The average velocity is about 4500 km. per hour but in two cases at Baker Lake the velocity was nearly 15,000 km. per hour or 4 km. per second. There were several cases where it was felt that even higher velocities occurred, but the trace appeared on only a few frames and so was not scaled.

On most of the occasions when type III reflections were seen, a great increase in absorption, resulting in a total blackout, occurred when the trace reached a height of 100 km. or less. When a total blackout did not occur, the absorption increased (as seen from the minimum frequency of reflection) and the E region appeared very turbulent. Often a night E layer (2) appeared, and after the absorption returned to normal, the E region remained turbulent. The occurrence of blackouts or night E prevented observations of the trace after it reached its minimum height.

Type III reflections have been seen only at Fort Chimo and Baker Lake, in the auroral zone. The suspicion that the echoes are connected with the aurora is supported by Fig. 10 where the diurnal distribution is shown.

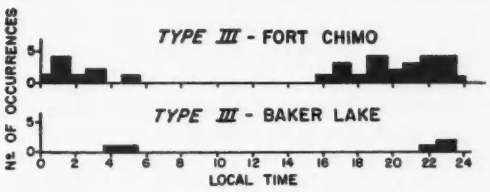

FIG. 10. Diurnal distribution of type III echoes.

All occurrences were between 4 p.m. and 5 a.m., roughly the same time as the aurora is observed.

One is tempted to suggest that type III echoes occur when a stream of charged particles enters the ionosphere and the point of contact of the stream with the E region moves horizontally. However, the velocities are very much higher than those of auroral structures which last for periods of several minutes, and it is hard to see how the echoes could be explained on this basis. It is probable that a satisfactory explanation of type III and type II echoes cannot be made unless simultaneous measurements of magnetic and auroral characteristics at the same station are available.

5. CONCLUSIONS

Type I echoes appear to arise from clouds of sporadic E ionization drifting with the winds in the E region of the ionosphere. The wind velocities measured on this assumption vary from 235 to 3500 km. per hour with a median value of 800 km. per hour. This is in general agreement with observations by other authors, having regard to the differing places of observation.

The echoes designated as type II and type III cannot be explained as simply as those of type I. Although type I and type III echoes have some

similarities, the extremely high velocities of type III echoes (up to 1500 km. per hour) make it most unlikely that the apparent motion is due to an ionospheric wind. Since type III reflections have been observed only at stations very close to the auroral zone maximum, it is quite possible that the effect is due to sweeping of the auroral ionizing agent. Type II echoes, while not as strictly limited to the auroral zone, also appear to relate to an auroral ionizing agent, and can be explained as due to a stream of ionizing radiation which has suddenly been turned on. The apparent downward velocity measured on this premise is about 7200 km. per hour.

ACKNOWLEDGMENTS

The authors are grateful to Dr. J. H. Chapman, Dr. P. A. Forsyth, and Dr. W. Petrie for useful talks in connection with this work.

REFERENCES

1. CHAPMAN, J. H. Can. J. Phys. 31: 120. 1953.
2. HANSON, G. H., HAGG, E. L., and FOWLE, D. Radio Phys. Lab. Rept. R-2. 1953.
3. MEEK, J. H. J. Geophys. Research, 54: 339. 1949.

CALCULATION OF DEPOLARIZATION FACTORS IN THE RAMAN SPECTRA OF POLYATOMIC MOLECULES[1]

By Salvador M. Ferigle and Alfons Weber

ABSTRACT

General expressions for the derived polarizability tensor are deduced for non-cyclic molecules having bonds with cylindrical symmetry by assuming the additivity of bond polarizabilities as suggested by Wolkenstein. Full use is made of the Wilson *FG* matrix technique. As an example, the expressions for the trace and the anistropy for the CX_3Y molecular type are obtained explicitly.

INTRODUCTION

The calculation of intensities and depolarization factors in the Raman spectra of polyatomic molecules has been given an increasing amount of attention in the last few years. The theory—as it stands today— assumes the additivity of bond polarizabilities, and this assumption, together with a few complementary assumptions about the dependence of the bond polarizabilities on the internal coordinates, was made the basis of the method developed by Wolkenstein (10). The same basic ideas have been used by Long (6), who used, however, different mathematical techniques more in line with the *FG* matrix method developed by Wilson (9) for the calculation of vibrational frequencies of polyatomic molecules. In this paper we attempt to make a more complete use of Wilson's formulas and to give a more explicit formulation for the elements of the derived polarizability tensor than was given in previous papers.

A set of rectangular coordinate axes xyz is fixed in the molecule and the additivity of bond polarizabilities and their derivatives is expressed as

$$\alpha_{uv} = \sum_n \alpha_{uv}^{(n)} \qquad [1]$$

and

$$\frac{\partial \alpha_{uv}}{\partial Q^k} = \sum_n \frac{\partial \alpha_{uv}^{(n)}}{\partial Q^k}, \qquad [2]$$

where u and v can take the values x, y, z; n refers to the nth bond in the molecule; the summation is carried over all the bonds in the molecule; and Q^k is the kth normal coordinate.

The depolarization factor ρ_k of the kth fundamental vibration is given by (8)

$$\rho_k = \frac{6B_k^2}{5A_k^2+7B_k^2} \qquad [3]$$

where A_k and B_k are respectively the trace and the anisotropy of the derived polarizability tensor $\partial\alpha_{uv}/\partial Q^k$, that is,

[1]*Manuscript received July 22, 1954.*
Contribution from Spectroscopy Laboratory, Physics Department, Illinois Institute of Technology, Chicago 16, Illinois.

$$[4]\quad \begin{cases} A_k = \sum_u \dfrac{\partial \alpha_{uu}}{\partial Q^k}, \\ B_k^2 = \dfrac{1}{2}\left\{\left(\dfrac{\partial \alpha_{xx}}{\partial Q^k} - \dfrac{\partial \alpha_{yy}}{\partial Q^k}\right)^2 + \left(\dfrac{\partial \alpha_{yy}}{\partial Q^k} - \dfrac{\partial \alpha_{zz}}{\partial Q^k}\right)^2 + \left(\dfrac{\partial \alpha_{zz}}{\partial Q^k} - \dfrac{\partial \alpha_{xx}}{\partial Q^k}\right)^2 \right. \\ \qquad \left. + 6\left[\left(\dfrac{\partial \alpha_{xy}}{\partial Q^k}\right)^2 + \left(\dfrac{\partial \alpha_{yz}}{\partial Q^k}\right)^2 + \left(\dfrac{\partial \alpha_{zz}}{\partial Q^k}\right)^2\right]\right\}. \end{cases}$$

For the special case of a symmetric top molecule, $\alpha_{xx} = \alpha_{yy} \neq \alpha_{zz}$ and, for totally symmetric vibrations,

$$[5]\quad B_k = A_k - 3\partial\alpha_{xx}/\partial Q^k.$$

The principal axes of the bond polarizability are assumed to be both in the equilibrium position and during vibration to be directed along and perpendicular to the bond, and therefore

$$[6]\quad \alpha_{uv}^{(n)} = \sum_m \alpha_{nm}\cos(nmu)\cos(nmv),$$

where m takes the value 1 for the component along the bond and the values 2 and 3 for the axes perpendicular to the bond, and $\cos(nmu)$ is the direction cosine of the nm-axis with the u-axis. For bonds with cylindrical symmetry $\alpha_{n2} = \alpha_{n3}$, and Eq. [6] gives, from the orthonormal properties of the direction cosines,

$$\begin{aligned} \alpha_{uv}^{(n)} &= \alpha_{n1}\cos(n1u)\cos(n1v) + \alpha_{n2}[\cos(n2u)\cos(n2v) + \cos(n3u)\cos(n3v)] \\ &= (\alpha_{n1} - \alpha_{n2})\cos(n1u)\cos(n1v) + \alpha_{n2}\delta_{uv}, \end{aligned}$$

where δ_{uv} is the Kronecker delta symbol. If we write (nu) for $(n1u)$ since it is simply the angle between the nth bond and the u-axis, the last equation can be written as

$$[7]\quad \alpha_{uv}^{(n)} = (\alpha_{n1} - \alpha_{n2})\cos(nu)\cos(nv) + \alpha_{n2}\delta_{uv}.$$

Wolkenstein assumed that α_{nm} depends only on the stretching of the nth bond, that is, it is unaffected by the stretching of other bonds or changes in interbond angles. Then, the molecular polarizabilities depend on the bond stretchings through α_{nm} and on the interbond bendings through the direction cosines. As clearly stated by Long, Wolkenstein's assumptions are not necessary and a similar treatment can be carried out without these simplifying assumptions; however, the final expressions will be much more cumbersome and the number of polarizability terms characterizing a bond will be larger. In the following we will restrict ourselves to non-cyclic molecules with bonds having cylindrical symmetry.

CALCULATION OF $\partial\alpha_{uv}/\partial Q^k$

Let us consider a non-cyclic molecule with N bonds. In the normal coordinate treatment internal coordinates are used (bond stretchings, interbond bendings, etc.), because in terms of them the potential constants have a clearer physical meaning. Then, symmetry coordinates are formed as linear combinations of

internal coordinates, which belong to the different irreducible representations of the point group of the molecule; thus the secular equation is factored out into several equations of lower order. However, a tensor referred to space-fixed axes (fixed as far as the vibration is concerned) such as the polarizability tensor cannot be defined in terms of internal coordinates. Wolkenstein and Eliashevich, and Long make use of some sort of intermediate coordinates.

Long defines the so-called intensity coordinates. For the molecule of N bonds which we are considering, there are N bond stretchings, and $3N$ direction cosines of which only $2N$ are independent because of the normalization condition. For the component α_{uv}, the N bond stretchings and the $2N$ direction cosines $\cos(nu)$, $\cos(nv)$ are used as intensity coordinates.

The following nomenclature will be used:

R^i = ith internal coordinate,
S^r = rth symmetry coordinate,
Q^k = kth normal coordinate,
I^p = pth intensity coordinate,
$\mathbf{d}_a$ = displacement vector of the ath atom during vibration.

The symmetry coordinates are related to the normal coordinates by means of the following matrix defined by Wilson

[8] $$S^r = \sum_k L_k^r Q^k$$

and

[9] $$Q^k = \sum_r (L^{-1})_r^k S^r,$$

where L and L^{-1} are obviously reciprocal matrices. The use of superscripts and subscripts has been kept here for consistency.

The symmetry coordinates are defined from the internal coordinates by means of

[10] $$S^r = \sum_i U_i^r R^i.$$

If there are redundancies, i.e. dependence between the internal coordinates, the matrix U will be rectangular; however, by making use of the redundancy relations it is possible to solve for the internal coordinates in terms of the symmetry coordinates, so that

[11] $$R^i = \sum_r T_r^i S^r.$$

Since the symmetry coordinates are orthonormal, including the redundancies, the matrix T is the transpose of the matrix U.

For the part involving the direction cosines, the displacement vectors $\mathbf{d}_a$ can be used as intermediate coordinates. The displacement vectors cannot be written directly unless explicit use is made of the Eckart conditions (3), since there are six more displacements than internal coordinates. On the other hand, the internal coordinates can be written as linear combinations of the displacement vectors as

[12] $$R^i = \sum_a \mathbf{s}_a^i \cdot \mathbf{d}_a,$$

where $\mathbf{s}_a^i$ is the **s**-vector associated with the ith internal coordinate and the ath atom as introduced by Wilson. Explicit formulas for the **s**-vectors corresponding to the different types of internal coordinates have been given in the literature (2, 4, 5, 9). By taking into account the consistency of Wilson's method with the Eckart conditions by which the latter are automatically taken care of (7) the displacement vectors can be expressed as

$$\mathbf{d}_a = \mu_a \sum_{ij} \mathbf{s}_a^j g_{ij} R^i \tag{13}$$

where μ_a is the reciprocal of the mass of the ath atom and g_{ij} is the kinetic energy matrix defined by

$$2T = \sum_{ij} g_{ij} \dot{R}^i \dot{R}^j.$$

Eq. [13] will be derived in the Appendix and corresponds to an expression given by Crawford and Fletcher (1) and used subsequently by Long (6).

We can now obtain the elements of the derived polarizability tensor, namely,

$$\frac{\partial \alpha_{uv}}{\partial Q^k} = \sum_p \frac{\partial \alpha_{uv}}{\partial I^p} \frac{\partial I^p}{\partial Q^k}.$$

Now, N of the intensity coordinates are bond stretchings which may be designated by the indices $p = 1, 2, \ldots, N$; the rest designated by the indices $p = N+1, \ldots, 3N$ are direction cosines. Then

$$\frac{\partial \alpha_{uv}}{\partial Q^k} = \sum_{p=1}^{N} \frac{\partial \alpha_{uv}}{\partial I^p} \frac{\partial I^p}{\partial Q^k} + \sum_{p=N+1}^{3N} \frac{\partial \alpha_{uv}}{\partial I^p} \frac{\partial I^p}{\partial Q^k}. \tag{14}$$

The first term on the right-hand side of Eq. [14] can be obtained very easily. From Eqs. [8] and [11] we have

$$R^i = \sum_{rk} T_r^i L_k^r Q^k, \tag{15}$$

and if we designate the internal coordinates corresponding to bond stretching by q^n, then

$$q^n = \sum_{rk} T_r^n L_k^r Q^k.$$

Then from Eq. [7]

$$\sum_{p=1}^{N} \frac{\partial \alpha_{uv}}{\partial I^p} \frac{\partial I^p}{\partial Q^k} = \sum_n \frac{\partial \alpha_{uv}^{(n)}}{\partial q^n} \frac{\partial q^n}{\partial Q^k} = \sum_{nr} \left[\cos(nu)\cos(nv) \frac{\partial}{\partial q^n}(\alpha_{n1} - \alpha_{n2}) + \delta_{uv} \frac{\partial \alpha_{n2}}{\partial q^n} \right] T_r^n L_k^r. \tag{16}$$

Although the index r in Eq. [16] formally runs over all the symmetry coordinates, T_r^n is clearly zero unless r refers to a symmetry coordinate involving bond stretchings.

For the second part on the right-hand side of Eq. [14] we have:

$$\sum_{p=N+1}^{3N} \frac{\partial \alpha_{uv}}{\partial I^p} \frac{\partial I^p}{\partial Q^k} = \sum_{p=N+1}^{3N} \frac{\partial \alpha_{uv}}{\partial I^p} \sum_{ai} \frac{\partial I^p}{\partial \mathbf{d}_a} \cdot \frac{\partial \mathbf{d}_a}{\partial R^i} \frac{\partial R^i}{\partial Q^k} = \sum_{p=N+1}^{3N} \frac{\partial \alpha_{uv}}{\partial I^p} \sum_{ajri} \frac{\partial I^p}{\partial \mathbf{d}_a} \cdot \mathbf{s}_a^j \mu_a g_{ij} T_r^i L_k^r, \tag{17}$$

where use has been made of Eqs. [13] and [15]. The index i runs formally over all internal coordinates.

We can define a set of vectors $\mathbf{S}_a^r$ each of which is associated with an atom and a symmetry coordinate by means of

$$\mathbf{s}_a^i = \sum_r T_r^i \mathbf{S}_a^r \tag{18}$$

in terms of which the displacement vectors can be written as

$$\mathbf{d}_a = \mu_a \sum_{rt} \mathbf{S}_a^r G_{rt} S^t \tag{19}$$

which is similar to Eq. [13] and where G_{rt} is the kinetic energy matrix defined by

$$2T = \sum_{rt} G_{rt} \dot{S}^r \dot{S}^t, \tag{20}$$

which is related to g_{ij} by means of

$$G_{rt} = \sum_{ij} g_{ij} T_r^i T_t^j. \tag{21}$$

From Eq. [18] we have

$$\begin{aligned} \sum_{ajrt} \frac{\partial I^p}{\partial \mathbf{d}_a} \cdot \mathbf{s}_a^j \mu_a g_{tj} T_r^i L_k^r &= \sum_{ajrti} \frac{\partial I^p}{\partial \mathbf{d}_a} \cdot \mathbf{S}_a^i T_{ti}^j \mu_a g_{tj} T_r^i L_k^r \\ &= \sum_{atr} \frac{\partial I^p}{\partial \mathbf{d}_a} \cdot \mathbf{S}_a^t \mu_a G_{tr} L_k^r \\ &= \sum_{at} \frac{\partial I^p}{\partial \mathbf{d}_a} \cdot \mathbf{S}_a^t \mu_a (L^{-1})_t^k, \end{aligned} \tag{22}$$

where the last step is obtained from the relations between the matrices L and L^{-1} introduced by Wilson (9).

From Eqs. [7] and [22], Eq. [17] can be written as

$$\begin{aligned} &\sum_{p=N+1}^{3N} \frac{\partial \alpha_{uv}}{\partial I^p} \frac{\partial I^n}{\partial Q^k} \\ &= \sum_n (\alpha_{n1} - \alpha_{n2}) \sum_{at} \left\{ \cos(nv) \frac{\partial}{\partial \mathbf{d}_a} \cos(nu) + \cos(nu) \frac{\partial}{\partial \mathbf{d}_a} \cos(nv) \right\} \cdot \mathbf{S}_a^t \mu_a (L^{-1})_t^k. \end{aligned} \tag{23}$$

In the summation with respect to the index a involved in Eq. [23] only two terms will appear, those corresponding to the two atoms which form the bond. If we call these atoms i and j, then

$$\frac{\partial}{\partial \mathbf{d}_i} \cos(nu) = -\sin(nu) \frac{\partial}{\partial \mathbf{d}_i}(nu) = \sin(nu) \mathbf{f}_{iu}^j Q_n,$$

where $\mathbf{f}_{iu}^j$ is a unit vector perpendicular to the ji-bond towards the u-axis, and Q_n is the reciprocal of the bond distance. This result follows immediately from the meaning of the partial derivative as the gradient of the angle at the equilibrium position (see Fig. 1). The vector $\mathbf{f}_{iu}^j$ can be written as a linear combination of a unit vector from the jth atom to the ith atom $\mathbf{e}_{ji}$, and a unit vector along the u-axis $\mathbf{e}_u$,

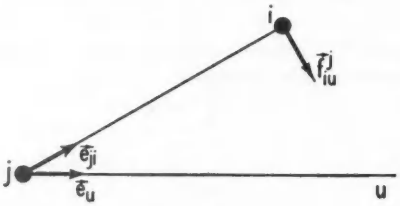

FIG. 1. The gradient of the angle between the *ji*-bond and the *u*-axis.

$$\mathbf{f}^j_{iu} = \frac{1}{\sin(nu)}[\mathbf{e}_u - \mathbf{e}_{ji}\cos(nu)].$$

Therefore

$$[24] \qquad \frac{\partial}{\partial \mathbf{d}_i}\cos(nu) = -\frac{\partial}{\partial \mathbf{d}_j}\cos(nu) = Q_n[\mathbf{e}_u - \mathbf{e}_{ji}\cos(nu)].$$

The final expression for the derived polarizability is then

$$[25] \quad \frac{\partial \alpha_{uv}}{\partial Q^k} = \sum_{nr}\left[\cos(nu)\cos(nv)\frac{\partial}{\partial q^n}(\alpha_{n1}-\alpha_{n2}) + \delta_{uv}\frac{\partial \alpha_{n2}}{\partial q^n}\right]T^n_r L^r_k$$

$$+ \sum_{nij}(\alpha_{n1}-\alpha_{n2})Q_n[\cos(nv)\mathbf{e}_u + \cos(nu)\mathbf{e}_v - 2\cos(nu)\cos(nv)\mathbf{e}_{ji}]$$

$$\cdot(\mu_i \mathbf{S}^i_i - \mu_j \mathbf{S}^i_j)(L^{-1})^k_{ij}.$$

From Eq. [7] it is clear that in the trace the second part of Eq. [25] contributes

$$\sum_u \frac{\partial \alpha^{(n)}_{uu}}{\partial I^p} = 0$$

from the normal property of direction cosines. Therefore only the first term of Eq. [25] contributes to the trace and from Eq. [16]

$$[26] \qquad \sum_u \frac{\partial \alpha^{(n)}_{uu}}{\partial Q^k} = \sum_{nr}\frac{\partial}{\partial q^n}(\alpha_{n1}+2\alpha_{n2})T^n_r L^r_k.$$

For a symmetry coordinate of totally symmetric type, all the elements T^n_r are the same, since symmetry coordinates are formed as linear combinations of equivalent internal coordinates; by using now the orthogonality property of symmetry coordinates it is seen that the trace is zero for any vibration other than the totally symmetric ones and therefore the corresponding depolarization factor is 6/7. This has been shown similarly by Wolkenstein and Eliashevich (10) and by Long (6).

AN EXAMPLE

As an example we will consider the tetrahedral CX_3Y molecule, shown in Fig. 2. The direction cosines are given in Table I. The **S** vectors can be ob-

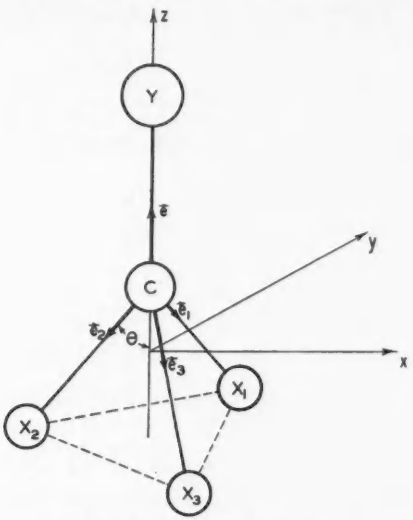

FIG. 2. The tetrahedral CX_3Y molecule.

TABLE I

DIRECTION COSINES FOR THE TETRAHEDRAL CX_3Y MOLECULE

Bond	Axes		
	x	y	z
CY	0	0	1
CX_1	0	$\sin\theta$	$-\cos\theta$
CX_2	$-\frac{1}{2}\sqrt{3}\sin\theta$	$-\frac{1}{2}\sin\theta$	$-\cos\theta$
CX_3	$\frac{1}{2}\sqrt{3}\sin\theta$	$-\frac{1}{2}\sin\theta$	$-\cos\theta$

tained from Eq. [18] and the **s** vectors given by Wilson. They are given in Table II, where the unit vectors are shown in Fig. 2 and the Q's are the reciprocals of the bond distances in the equilibrium position.

TABLE II

S VECTORS FOR THE TETRAHEDRAL CX_3Y MOLECULE

Atom	Symmetry coordinate		
	1	2	3
C	$-\mathbf{e}$	$-\frac{1}{\sqrt{3}}(\mathbf{e}_1+\mathbf{e}_2+\mathbf{e}_3)$	$\left[\frac{7\sqrt{3}}{12}Q_z-\frac{\sqrt{3}}{4}Q_y\right](\mathbf{e}_1+\mathbf{e}_2+\mathbf{e}_3)-\frac{\sqrt{3}}{4}(3Q_z+Q_y)\mathbf{e}$
X_1	0	$\frac{1}{\sqrt{3}}\mathbf{e}_1$	$-\frac{\sqrt{3}}{12}Q_z(\mathbf{e}_1+3\mathbf{e}_2+3\mathbf{e}_3-3\mathbf{e})$
X_2	0	$\frac{1}{\sqrt{3}}\mathbf{e}_2$	$-\frac{\sqrt{3}}{12}Q_z(\mathbf{e}_2+3\mathbf{e}_3+3\mathbf{e}_1-3\mathbf{e})$
X_3	0	$\frac{1}{\sqrt{3}}\mathbf{e}_3$	$-\frac{\sqrt{3}}{12}Q_z(\mathbf{e}_3+3\mathbf{e}_1+3\mathbf{e}_2-3\mathbf{e})$
Y	$\mathbf{e}$	0	$\frac{\sqrt{3}}{4}Q_y(\mathbf{e}_1+\mathbf{e}_2+\mathbf{e}_3+\mathbf{e})$

From Eqs. [25] and [26] and use of the values given in Tables I and II, we obtain

$$\frac{\partial \alpha_{xx}}{\partial Q^k} = \alpha'_{y2} L^1_k + 3^{-\frac{1}{2}}[\tfrac{4}{3}(\alpha'_{x1} - \alpha'_{x2}) + 3\alpha'_{x2}] L^2_k$$

$$+\tfrac{4}{3}(3^{-\frac{1}{2}})(\alpha_{x1} - \alpha_{x2}) Q_x \{2[3^{-\frac{1}{2}}(L^{-1})^k_1 - \tfrac{1}{3}(L^{-1})^k_2 + \tfrac{4}{3} Q_x (L^{-1})^k_3]\mu_C + \mu_X Q_x (L^{-1})^k_3\}.$$

The trace and the anisotropy are then

$$A_k = (\alpha'_{y1} + 2\alpha'_{y2}) L^1_k + 3^{\frac{1}{2}}(\alpha'_{x1} + 2\alpha'_{x2}) L^2_k$$

and

$$B_k = (\alpha'_{y1} - \alpha'_{y2}) L^1_k - 3^{-\frac{1}{2}}(\alpha'_{x1} - \alpha'_{x2}) L^2_k$$

$$-4(3^{-\frac{1}{2}})(\alpha_{x1} - \alpha_{x2}) Q_x \{2[3^{-\frac{1}{2}}(L^{-1})^k_1 - \tfrac{1}{3}(L^{-1})^k_2 + \tfrac{4}{3} Q_x (L^{-1})^k_3]\mu_C + \mu_X Q_x (L^{-1})^k_3\}.$$

The prime indicates the derivative of the bond polarizability with respect to bond stretching.

APPENDIX

In a previous paper (7) the matrices **D** and **Q** were defined as relating the internal coordinates to the mass reduced displacement coordinates. By Eq. [10] of Reference 7 we have

$$\sum_j Q^a_j D^j_b + \sum_p Q^a_p D^p_b = \delta^a_b.$$

Multiplying by $D^t_c \delta^{cb}$ we get

$$\sum_{jbc} Q^a_j D^j_b D^t_c \delta^{cb} + \sum_{pbc} Q^a_p D^p_b D^t_c \delta^{cb} = \sum_{cb} D^t_c \delta^{cb} \delta^a_b$$

from which, by use of Eqs. [12] and [14] of Reference 7, we obtain

$$\sum_j Q^a_j g^{tj} = D^t_a.$$

Multiplying now by g_{ik} and summing over i we finally obtain

$$Q^a_k = \sum_i D^i_a g_{ik}.$$

By splitting the index a, the last equation can be written as

$$\frac{\partial x^{nt}}{\partial R^k} = \frac{1}{\sqrt{m_n}} \sum_i D^i_{nt} g_{ik} = \frac{1}{m_n} \sum_i \mathbf{s}^i_n \cdot \mathbf{e}_t g_{ik}.$$

By combining now the three components of $\mathbf{d}_n$, the displacement vector of the nth atom, we get

$$\mathbf{d}_n = \mu_n \sum_{ik} \mathbf{s}^i_n g_{ik} R^k,$$

which is Eq. [13] of this paper.

REFERENCES

1. CRAWFORD, B. L. and FLETCHER, W. H. J. Chem. Phys. 19: 141. 1951.
2. DECIUS, J. C. J. Chem. Phys. 16: 1025. 1948.
3. ECKART, C. Phys. Rev. 47: 552. 1935.

4. FERIGLE, S. M. and MEISTER, A. G. J. Chem. Phys. 19: 982. 1951.
5. LOHMAN, J. B. Tech. Repts. No. 17. U.S. Office of Naval Research. 1951.
6. LONG, D. A. Proc. Roy. Soc. (London), A, 217: 203. 1953.
7. MALHIOT, R. J. and FERIGLE, S. M. J. Chem. Phys. 22: 717. 1954.
8. PLACZEK, G. Handbuch der radiologie. Vol. 6. 2nd ed. 1934.
9. WILSON, E. B., JR. J. Chem. Phys. 7: 1047. 1939; 9: 76. 1941.
10. WOLKENSTEIN, M. and ELIASHEVICH, M. Acta Physicochim. U.R.S.S. 20: 525. 1945.

LETTERS TO THE EDITOR

Under this heading brief reports of important discoveries in physics may be published. These reports should not exceed 600 words and, for any issue, should be submitted not later than six weeks previous to the first day of the month of issue. No proof will be sent to the authors.

Atomic Masses of Ru^{98}, Ru^{99}, Os^{189}, and Os^{192} *

The atomic masses of Ru^{98}, Ru^{99}, Os^{189}, and Os^{192} have been measured using the Dempster-type mass spectrograph at McMaster University. Both the instrument (2) and the method (3) have been described in detail previously. The mass differences obtained in this work and the atomic masses deduced therefrom are given in Table I.

TABLE I

MEASURED MASS DIFFERENCES AND COMPUTED ATOMIC MASSES

Doublet	Mass difference (m.m.u.)	Atomic mass (a.m.u.)
$\frac{1}{2}Os^{189} - Cu^{63}$	56.6 ± 3	$Os^{189} = 189.0177 \pm 9$
$\frac{1}{2}Os^{192} - Ni^{64}$	59.9 ± 2	$Os^{192} = 192.0224 \pm 8$
$\frac{1}{2}Pt^{196} - Ru^{98}$	77.0 ± 3	$Ru^{98} = 97.9363 \pm 4$
$\frac{1}{2}Pt^{198} - Ru^{99}$	76.3 ± 2	$Ru^{99} = 98.9378 \pm 4$

In order to calculate each of the above masses it was, of course, necessary to know the mass of the other member of the doublet. The values of these reference masses were taken to be: $Cu^{63} = 62.94926 \pm 6$ (1), $Ni^{64} = 63.94755 \pm 7$ (4), $Pt^{196} = 196.0267 \pm 6$ (5), and $Pt^{198} = 198.0283 \pm 6$ (5). In the case of Pt^{198}, an error in arithmetic leading to the wrong value given in Reference 5 has been corrected.

1. COLLINS, T. L., NIER, A. O. C., and JOHNSON, W. H., Jr. Phys. Rev. 86: 408. 1952.
2. DUCKWORTH, H. E. Rev. Sci. Instr. 21: 54. 1950.
3. HOGG, B. G. and DUCKWORTH, H. E. Can. J. Phys. 30: 637. 1952.
4. HOGG, B. G. and DUCKWORTH, H. E. Can. J. Phys. 31: 942. 1953.
5. HOGG, B. G. and DUCKWORTH, H. E. Can. J. Phys. 32: 65. 1954.

RECEIVED OCTOBER 15, 1954.

DEPARTMENT OF PHYSICS,
HAMILTON COLLEGE,
McMASTER UNIVERSITY,
HAMILTON, ONTARIO.

EDWIN M. PENNINGTON†
HENRY E. DUCKWORTH

**This work was supported by the Office of Scientific Research, Air Research and Development Command, U.S. Air Force, the National Research Council of Canada, and the Research Council of Ontario.*

†*Holder of a Research Council of Ontario Scholarship 1953–54, and currently holder of a National Research Council Scholarship.*

CONTENTS OF VOLUME 32

ALMQVIST, E., PEPPER, T. P., and LORRAIN, P.—The angular distribution of the $Li^7(l, \alpha)He^6$ reactions at 240 kev. triton energy, 621.

ATKINS, K. R.—Some comments on helium films, 347.

ATKINS, K. R. and HART, K. H.—The attenuation of second sound in liquid helium II above 1°K., 381.

ATKINS, K. R. and LOVEJOY, D. R.—A method of concentrating He^3–He^4 mixtures, 702.

BEAUMONT, C. F. A.—A potential function for liquid helium at 0°K., 759.

BEKEFI, G.—The impedance of an antenna above a circular ground plate laid upon a plane earth, 205.

BELL, R. E. and YAFFE, L.—Search for a possible error in the measured half life of Au^{198}, 416.

BRECKON, S. W., HENRIKSON, A., MARTIN, W. M., and FOSTER, J. S.—The radioactive isotopes Al^{24}, P^{28}, Cl^{32}, 223.

BRICOUT, P. A.—Refractive index nomogram for dry and humid air, 243.

BRIX, P. and HERZBERG, G.—Fine structure of the Schumann-Runge bands near the convergence limit and the dissociation energy of the oxygen molecule, 110.

BROWN, S. B. and PETRIE, W.—The effect of sunrise on the reflection height of low frequency waves, 90.

CHISHOLM, D. A. and WELSH, H. L.—Induced infrared absorption in hydrogen and hydrogen – foreign gas mixtures at pressures up to 1500 atmospheres, 291.

CLARKE, E. M.—Ionization probability curves using an electron selector. Results on N_2^+, N^+, Xe^{++}, 764.

CLUSIUS, K. and DOUGLAS, A. E.—The λ4050 bands of the C_3^{13} molecule, 319.

COSTELLO, M., SERSON, H., MONTALBETTI, R., and PETRIE, W.—The occurrence of ionized nitrogen bands in the twilight spectrum, 562(L).

COWAN, J. A.—Counting slow electrons with an electron multiplier, 101.

COX, J. W. and DAVIES, K.—Statistical studies of polar radio blackouts, 743.

CRAWFORD, G. J. B.—See Moody, H. J.

DANIELS, J. M.—Some experiments and theoretical considerations on the electric h.f.s. method of nuclear alignment, 662.

DAVIES, K.—See Cox, J. W.

DEMERS, P.—Cosmic ray phenomena at minimum ionization in a new nuclear emulsion having a fine grain, made in the laboratory, 538.

DONNELLY, R. J.—See Johns, M. W.

DOUGLAS, A. E.—See Clusius, K.

DUCKWORTH, H. E.—See Hogg, B. G.; Pennington, E. M.

ELLIOTT, L. G., PRESTON, M. A., and WOLFSON, J. L.—Disintegration of Au^{198}, 153.

ERDMAN, K. L.—See Warren, J. B.

FELDMAN, T.—See Romanko, J.

FERIGLE, S. M. and WEBER, A.—Calculation of depolarization factors in the Raman spectra of polyatomic molecules, 799.

FINKELSTEIN, R., GASIOROWICZ, S. G., and KAUS, P.—Description of a composite particle in terms of a functional potential well, 480.

FLEMING, W., TOMLINSON, R. H., and THODE, H. G.—The fission yields of the stable and long-lived isotopes of xenon, cesium, and krypton in neutron fission of U^{233}, 522.

FOSTER, J. S.—See Breckon, S. W.

FRASER, P. A.—A method of determining the electronic transition moment for diatomic molecules, 515.

FROESE, C. and WAIT, J. R.—Calculated diffraction patterns of dielectric rods at centimetric wavelengths, 775.

FROOD, D. G.—A note on the use of the titanates as thermoelectric transducers, 313.

GASIOROWICZ, S. G.—See Finkelstein, R.

GEIGER, K. W. and ROSE, D. C.—The multiplicity of neutron production by spontaneous fission of uranium, 498.

GOLDEMBERG, J.—See Katz, L.

GOLDEMBERG, J. and KATZ, L.—Photoneutron cross sections of some elements, 49.

GRAHAM, R. L. and STEWART, A. T.—Three-quantum annihilation of positrons in solids, 678(L).

GRANT, H. L. and STEWART, R. W.—A logarithmic photometer, 674.

GRUENBERG, H.—See Hurd, R. A.

HAGG, E. L. and HANSON, G. H.—Motion of clouds of abnormal ionization in the auroral and polar regions, 790.

HANSON, G. H.—See Hagg, E. L.

HART, J.—The effect of a steady transverse electric field on the viscosity of polar liquid dielectrics, 99(L).

HART, K. H.—See Atkins, K. R.

HASLAM, R. N. H.—See Katz, L.; Taylor, J. G. V.

HASLAM, R. N. H., ROBERTS, W. N., and ROBB, D. S.—Cross section for the reaction $Al^{27}(\gamma, n)Al^{26}$, 361.

HENRIKSON, A.—See Breckon, S. W.

HERZBERG, G.—See Brix, P.

HOGG, B. G. and DUCKWORTH, H. E.—An atomic mass study of nuclear shell structure in the region $82 < n < 126$, 65.

HUGO, T. J.—See Naudé, S. M.

HULL, T. E. and WOLFE, W. A.—On inverting Laplace transforms of the form $h(s)/(p(s)+q(s)e^{-\tau s})$, 72.

HURD, R. A.—The propagation of an electromagnetic wave along an infinite corrugated surface, 727.

HURD, R. A. and GRUENBERG, H.—*H*-Plane bifurcation of rectangular waveguides, 694.

JACKSON, J. D.—Electron capture by slow singly charged helium ions in helium, 60.

JAMES, D. B.—See Warren, J. B.

JARMAIN, W. R. and NICHOLLS, R. W.—Vibrational transition probabilities to high quantum numbers for the nitrogen first and second positive band systems, 201.

JOHNS, M. W., MCMULLEN, C. C., DONNELLY, R. J., and NABLO, S. V.—Coincidence studies of the decay of indium 114, 35.

JOHNS, M. W. and SARGENT, B. W.—Photoneutrons in a heavy water pile, 136.

KAEMPFFER, F. A.—On the concept of field quantization, 259. Note on the self-energy of single roton states in quantum hydrodynamics, 264. On a two-fluid model of matter, 430. On the relation between quantum hydrodynamics and conventional quantum field theory, 530.

KAHANA, S.—See Wait, J. R.

KATZ, L.—See Goldemberg, J.; McPherson, D.

KATZ, L., HASLAM, R. N. H., GOLDEMBERG, J., and TAYLOR, J. G. V.—The photoneutron and photoproton cross sections of silicon and magnesium, 580.

KAUS, P.—See Finkelstein, R.

KELLY, F. M.—On θ values in metals. II, 81.

KERWIN, L.—Some mass spectrometric data on phosphorus, 757.

KIRKALDY, J. S.—Dead-time losses in multichannel coincidence systems, 406.

LAMARCHE, G.—See Volkoff, G. M.

LAURIE, K. A.—See Warren, J. B.

LOKKEN, J. E.—Contribution from phonon–phonon interactions to the T^3 term of the specific heat of helium II, 359 (L).

LORRAIN, P.—See Almqvist, E.

LOVEJOY, D. R.—See Atkins, K. R.

MCKELLAR, A.—See Romanko, J.

MCKINLEY, D. W. R.—Dependence of integrated duration of meteor echoes on wavelength and sensitivity, 450.

MCLAY, A. B.—See Wiles, S. T.

MCMULLEN, C. C.—See Johns, M. W.

MCNAMARA, A. G.—See Meek, J. H.

MCNARRY, L. R.—See Redhead, P. A.

MCPHERSON, D., PEDERSON, E., and KATZ, L.—The (γ, n) and (γ, p) cross sections of argon^{40}, 593.

MARRIS, A. W.—On the Nusselt modulus as a function of friction factor, Reynolds and Prandtl moduli, for heat transfer to a fluid flowing turbulently through a tube of circular section, 167. An experimental investigation of the heat transfer to turbulently flowing pressurized air, 190. The momentum and vorticity transfer theories of turbulent heat transfer, 419.

MARTIN, W. M.—See Breckon, S. W.

MEEK, J. H. and MCNAMARA, A. G.—Magnetic disturbances, sporadic *E*, and radio echoes associated with the aurora, 326.

MØLLER, C. K. and STOICHEFF, B. P.—High resolution Raman spectroscopy of gases. IV. Rotational Raman spectrum of cyanogen, 635.

MONTALBETTI, R.—See Costello, M.

MOODY, H. J. and CRAWFORD, G. J. B.—An electronic ratchet, 356.

NABLO, S. V.—See Johns, M. W.

NAUDÉ, S. M. and HUGO, T. J.—The emission spectrum of aluminum monofluoride. II, 246.

NEUGEBAUER, H. E. J.—Clausius-Mosotti equation for certain types of anisotropic crystals, 1.

NICHOLLS, R. W.—An experimental study of band intensities in the first positive system of N_2. III. Quantitative treatment of eye estimates, 722. See Jarmain, W. R.; Turner, R. G.

NILBERG, R. H.—The American wind turbine, 639.

NIVEN, C. D.—The effect of high loading on the kinetic friction of ice, 782.

PEARSON, W. B.—Thermal expansion of lithium, 77° to 300°K., 708.

PEDERSON, E.—See McPherson, D.

PENNINGTON, E. M. and DUCKWORTH, H. E.—Atomic masses of Ru^{98}, Ru^{99}, Os^{189}, and Os^{192}, 808(L).

PEPPER, T. P.—See Almqvist, E.

PETRIE, W.—See Brown, S. B.; Costello, M.

PLINT, C. A., SMALL, R. M. B., and WELSH, H. L.—Density effects in the Raman spectrum of ammonia, 653.

PRESTON, M. A.—See Elliott, L. G.

REDHEAD, P. A. and MCNARRY, L. R.—An ionization manometer and control unit for extremely low pressures, 267.

RITTER, G. J.—See Zeeman, P. B.

ROBB, D. S.—See Haslam, R. N. H.

ROBERTS, W. N.—See Haslam, R. N. H.

ROBINSON, L. B.—See Taylor, J. G. V.

ROMANKO, J., FELDMAN, T., STANSBURY, E. J., and MCKELLAR, A.—The rotational Raman spectrum of ethylene, 735.

ROSE, D. C.—See Geiger, K. W.

ROY, S. K.—On the evaluation of certain lattice series, 509.

RUMSEY, V. H.—On the analysis of experiments involving the kinetics of piles with reflectors, 435.

RUSSELL, R. D.—See Shillibeer, H. A.

SANDERS, F. H.—Image interference in calm, near-isothermal water. *With an appendix by* STEWART, R. W.—"Lloyd's mirror" interference in the presence of slight uniform refraction—an approximate theory, 599.

SARGENT, B. W.—See Johns, M. W.

SCHIFF, H.—Electron capture cross sections, 393.

SERSON, H.—See Costello, M.

SHILLIBEER, H. A. and RUSSELL, R. D.—The potassium–argon method of geological age determination, 681.

SMALL, R. M. B.—See Plint, C. A.

STANSBURY, E. J.—See Romanko, J.

STEWART, A. T.—See Graham, R. L.

STEWART, R. W.—See Grant, H. L.; Sanders, F. H.

STOICHEFF, B. P.—High resolution Raman spectroscopy of gases. I. Experimental methods, 330. II. Rotational spectra of C_6H_6 and C_6D_6, and internuclear distances in the benzene molecule, 339. III. Raman spectrum of nitrogen, 630. See Møller, C. K.

TAYLOR, J. G. V.—See Katz, L.

TAYLOR, J. G. V., ROBINSON, L. B., and HASLAM, R. N. H.—Fine structure of the $F^{19}(\gamma, n)F^{18}$ activation curve, 238.

THODE, H. G.—See Fleming, W.

TOMLINSON, R. H.—See Fleming, W.

TURNER, C. H. M.—Birefringence in crystals and in the ionosphere, 16.

TURNER, R. G. and NICHOLLS, R. W.—An experimental study of band intensities in the first positive system of N_2. I. Vibrational transition probabilities, 468. II. The transition moment, 475.

VOLKOFF, G. M. and LAMARCHE, G.—Further calculations on the nuclear resonance spectrum of Al^{27} in spodumene, 493.

WAIT, J. R.—On the theory of an antenna with an infinite corner reflector, 365. Reflection from a wire grid parallel to a conducting plane, 571. See Froese, C.

WAIT, J. R. and KAHANA, S.—Radiation from a slot on a cylindrically tipped wedge, 714.

WARREN, J. B., LAURIE, K. A., JAMES, D. B., and ERDMAN, K. L.—Gamma radiation from the proton bombardment of oxygen, 563.

WEBER, A.—See Ferigle, S. M.

WELSH, H. L.—See Chisholm, D. A.; Plint, C. A.

WHITTIER, A. C.—Fast negative hydrogen ions, 275.

WILES, S. T. and MCLAY, A. B.—Diffraction of 3.2 cm. electromagnetic waves by cylindrical objects, 372.

WOLFE, W. A.—See Hull, T. E.

WOLFSON, J. L.—See Elliott, L. G.

YAFFE, L.—See Bell, R. E.

ZEEMAN, P. B.—Spectrum of the AlC molecule, 9.

ZEEMAN, P. B. and RITTER, G. J.—New measurements on the $A^1\Pi \leftrightarrow X^1\Sigma$ band system of AlH, 555.

CORRECTION

Vol. 30, 1952, pp. 574–575. The measured values of the electric field in Figs. 2 and 3 are in error and should be multiplied by 0.68 to obtain the correct r.m.s. fields.

CANADIAN JOURNAL OF PHYSICS

Notes to Contributors

Manuscripts

(i) ***General.*** Manuscripts should be typewritten, double spaced, on paper 8½×11 in. **The original and one copy are to be submitted.** Tables (each typed on a separate sheet) and captions for the figures should be placed at the end of the manuscript. Every sheet of the manuscript should be numbered.

Style, arrangement, spelling, and abbreviations should conform to the usage of this journal. Names of all simple compounds, rather than their formulas, should be used in the text. Greek letters or unusual signs should be written plainly or explained by marginal notes. Superscripts and subscripts must be legible and carefully placed.

Manuscripts should be carefully checked before they are submitted; authors will be charged for changes made in the proof that are considered excessive.

(ii) ***Abstract.*** An abstract of not more than about 200 words, indicating the scope of the work and the principal findings, is required, except in Notes.

(iii) ***References.*** References should be listed **alphabetically by authors' names,** numbered, and typed after the text. The form of the citations should be that used in this journal; in references to papers in periodicals, titles should not be given and only initial page numbers are required. All citations should be checked with the original articles and each one referred to in the text by the key number.

(iv) ***Tables.*** Tables should be numbered in roman numerals and each table referred to in the text. Titles should always be given but should be brief; column headings should be brief and descriptive matter in the tables confined to a minimum. Numerous small tables should be avoided.

Illustrations

(i) ***General.*** All figures (including each figure of the plates) should be numbered consecutively from 1 up, in arabic numerals, and each figure referred to in the text. The author's name, title of the paper, and figure number should be written in the lower left corner of the sheets on which the illustrations appear. Captions should not be written on the illustrations (see Manuscript (i)).

(ii) ***Line Drawings.*** Drawings should be carefully made with India ink on white drawing paper, blue tracing linen, or co-ordinate paper ruled in blue only; any co-ordinate lines that are to appear in the reproduction should be ruled in black ink. Paper ruled in green, yellow, or red should not be used unless it is desired to have all the co-ordinate lines show. All lines should be of sufficient thickness to reproduce well. Decimal points, periods, and stippled dots should be solid black circles large enough to be reduced if necessary. Letters and numerals should be neatly made, preferably with a stencil (**do NOT use typewriting**), and be of such size that the smallest lettering will be not less than 1 mm. high when reproduced in a cut 3 in. wide.

Many drawings are made too large; originals should not be more than 2 or 3 times the size of the desired reproduction. In large drawings or groups of drawings the ratio of height to width should conform to that of a journal page but the height should be adjusted to make allowance for the caption.

The original drawings and one set of clear copies (e.g. small photographs) are to be submitted.

(iii) ***Photographs.*** Prints should be made on glossy paper, with strong contrasts. They should be trimmed so that essential features only are shown and mounted carefully, with rubber cement, on white cardboard.

As many photographs as possible should be mounted together (with a **very** small space between each photo) to reduce the number of cuts required. Full use of the space available should be made and the ratio of height to width should correspond to that of a journal page; however, allowance must be made for the captions. Photographs or groups of photographs should not be more than 2 or 3 times the size of the desired reproduction.

Photographs are to be submitted in duplicate; if they are to be reproduced in groups one set should be mounted, the duplicate set unmounted.

Reprints

A total of 50 reprints of each paper, without covers, are supplied free. Additional reprints, with or without covers, may be purchased.

Charges for reprints are based on the number of printed pages, which may be calculated approximately by multiplying by 0.6 the number of manuscript pages (double-spaced typewritten sheets, 8½ × 11 in.) and making allowance for illustrations (not inserts). The cost per page is given on the reprint requisition which accompanies the galley.

Any reprints required in addition to those requested on the author's reprint requisition form must be ordered officially as soon as the paper has been accepted for publication.

Contents

Page

The Propagation of an Electromagnetic Wave Along an Infinite Corrugated Surface—*R. A. Hurd* - - - - - - - - - - 727

The Rotational Raman Spectrum of Ethylene—*J. Romanko, T. Feldman, E. J. Stansbury, and A. McKellar* - - - - - - 735

Statistical Studies of Polar Radio Blackouts—*J. W. Cox and Kenneth Davies* - - - - - - - - - - - - - - - - - 743

Some Mass Spectrometric Data on Phosphorus—*Larkin Kerwin* 757

A Potential Function for Liquid Helium at 0°K.—*C. F. A. Beaumont* 759

Ionization Probability Curves Using an Electron Selector. Results on N_2^+, N^+, Xe^{++}—*E. M. Clarke* - - - - - - - - - - 764

Calculated Diffraction Patterns of Dielectric Rods at Centimetric Wavelengths—*Charlotte Froese and James R. Wait* - - - 775

The Effect of High Loading on the Kinetic Friction of Ice—*C. D. Niven* - - - - - - - - - - - - - - - - - - 782

Motion of Clouds of Abnormal Ionization in the Auroral and Polar Regions—*E. L. Hagg and G. H. Hanson* - - - - - - - 790

Calculation of Depolarization Factors in the Raman Spectra of Polyatomic Molecules—*Salvador M. Ferigle and Alfons Weber* 799

Letter to the Editor:

Atomic Masses of Ru^{98}, Ru^{99}, Os^{189}, and Os^{192}—*Edwin M. Pennington and Henry E. Duckworth* - - - - - - - 808

Contents of Volume 32 - - - - - - - - - - - - - - 809

Printed in Canada *by* University of Toronto Press